

AD-A212 749

OHIO
STATE

4

Progress in the Identification of Airborne Radar Targets

R. Carrière, F.D. Garber, I. Jouny, R. L. Moses
O.S. Sands, W.M. Steedly and E.K. Walton

The Ohio State University
ElectroScience Laboratory

Department of Electrical Engineering
Columbus, Ohio 43212

Technical Report 718048-12
Contract No. N00014-86-K-0202
June 1989

Department of the Navy
Office of Naval Research
800 North Quincy Street
Arlington, Virginia 22217-5000

DTIC
ELECTE
SEP 18 1989
S B D

DISTRIBUTION STATEMENT A

Approved for public release
Distribution Unlimited

89 9 18 20 3

NOTICES

When Government drawings, specifications, or other data are used for any purpose other than in connection with a definitely related Government procurement operation, the United States Government thereby incurs no responsibility nor any obligation whatsoever, and the fact that the Government may have formulated, furnished, or in any way supplied the said drawings, specifications, or other data, is not to be regarded by implication or otherwise as in any manner licensing the holder or any other person or corporation, or conveying any rights or permission to manufacture, use, or sell any patented invention that may in any way be related thereto.

REPORT DOCUMENTATION PAGE	1. REPORT NO.	2.	3. Recipient's Accession No.
4. Title and Subtitle Progress in the Identification of Airborne Radar Targets			5. Report Date June 1989
7. Author(s) R. Carrière, F.D. Garber, I. Jouny, R.L. Moses, O.S. Sands, W.E. Steedly, E.K. Walton			6.
9. Performing Organisation Name and Address The Ohio State University ElectroScience Laboratory 1320 Kinnear Road Columbus, OH 43212			8. Performing Org. Rept. No. 718048-12
12. Sponsoring Organisation Name and Address Office of Naval Research Room 804, Code 1211, 800 North Quincy Street Washington, D.C. 22217			10. Project/Task/Work Unit No.
15. Supplementary Notes			11. Contract(C) or Grant(G) No. (C) N00014-86-K-0202 (G)
16. Abstract (Limit: 200 words) This report documents a summary of the work accomplished during the first six months under the project entitled "Identification of Airborne Radar Targets." The accomplishments discussed include: The development of techniques to estimate and parameterize canonical scattering centers of a radar object, the development and evaluation of a signal processing technique that estimates the polarization characteristics of target scattering centers the evaluation of the feasibility of using bispectrum processing techniques for the purpose of radar target characterization and classification, and the development of improved techniques for target identification based on structural pattern recognition.			13. Report Type/Period Covered Technical Report
14.			
17. Document Analysis a. Descriptors			
b. Identifiers/Open-Ended Terms			
c. COSATI Field/Group			
18. Availability Statement A. Approved for public release; Distribution is unlimited.	19. Security Class (This Report) Unclassified		21. No. of Pages 96
	20. Security Class (This Page) Unclassified		22. Price

Contents

1	Executive Summary	1
2	High Resolution Radar Target Modeling Using ARMA Models	2
2.1	Canonical Scatterers	2
2.2	ARMA Models	4
2.3	Experimental Results	6
2.3.1	Results from Applying ARMA Techniques to Compact Range Data	6
2.3.2	Direct Estimation of the Canonical Scatterer Model	11
3	Exponential Modeling of Fully Polarized Radar Return	15
3.1	Modeling the Scatterers	15
3.2	Determining Scatterer Locations and Associated Polarizations	17
3.3	Simulation Results	18
4	A Study of The Bispectral Estimates of Radar Signals And Appli- cation To Radar Target Identification	28
4.1	Introduction	28
4.2	Problem Formulation: Birange Profile Theory	29
4.3	Classical Bispectrum Estimation Algorithms	32
4.3.1	Indirect Method	33
4.3.2	Direct Method	33
4.4	Blade-Sphere Example	34
4.5	Bispectral Response of Noisy Data	35
4.5.1	Mean Square Error	35
4.6	Bispectral Response For Dispersive Scatterers	38
4.6.1	Single Edge Dispersion	38
4.7	Bispectral Responses for Canonical Aircraft	39
4.8	Bispectral Responses for Commercial Aircraft	39
4.9	Classification Methods	40



For	
Dist	<input checked="" type="checkbox"/>
Avail and/or	<input type="checkbox"/>
Special	<input type="checkbox"/>
Availability Codes	
A-1	

4.9.1	Indirect method	41
4.9.2	Direct method	42
4.9.3	Comparison	42
4.9.4	Classification Algorithm	43
4.10	Radar Target Identification Example	44
4.11	Conclusions	45
5	Investigations of Structural Pattern Recognition Methods for Radar	
	Target Identification	78
5.1	Introduction	78
5.2	Analytical Methods for Likelihood Function Determination	80
5.2.1	Conditional String Probability Estimation	81
5.2.2	Conditional Symbol Probability Calculations	86
5.2.3	Conclusions and Results	89
5.3	Conversion of Syntactic Classifiers to Deterministic Forms	92
6	References	95

List of Figures

2.1	Response of the Concord for $N = 30$, $M = 5$ and 10 , $n = 3$, $m = 2$. Data taken between 18–26 GHz.	7
2.2	Response of the Concord for $N = 30$, $M = 10$, $n = 3, 5$ and 7 , $m = 2$. Data taken between 18–26 GHz.	8
2.3	Response of the Concord for $N = 30$, $M = 10$, $n = 5$, $m = 2$. Data taken between 18–26 GHz with 10 dB SNR.	9
2.4	Response of the Concord for $N = 20$, $M = 10$, $n = 7$, $m = 4$. Data taken between 6.25–12 GHz at 0 and 20 degree aspect angle.	10
2.5	Concord, 18-26 GHz, FFT using 30 data points zero padded to 512, 0 degree aspect angle.	12
2.6	Scaled Picture of the Concord.	13
3.1	707 Scatterers and Polarizations	20
3.2	727 Scatterers and Polarizations	20
3.3	747 Scatterers and Polarizations	21
3.4	DC10 Scatterers and Polarizations	21
3.5	Concord Scatterers and Polarizations	22
3.6	DC10 Scatterers and Polarizations, SNR of 10dB	24
3.7	DC10 Scatterers and Polarizations, SNR of 5dB	25
3.8	DC10 Scatterers and Polarizations, SNR of 0dB	26
4.1	Optimum window (minimum bias supremum) in frequency domain. . .	46
4.2	Optimum window (minimum bias supremum) in range domain. . . .	47
4.3	Internal bounce diagram for blade-sphere interaction.	48
4.4	Frequency response for blade-sphere target.	49
4.5	Impulse response for blade-sphere, $r_0 = 0$, $r_1 = 1.6$ m, $r_2 = 2.4$ m. . .	50
4.6	Bispectrum for blade-sphere without window.	51
4.7	Bispectrum for blade-sphere $r_1 = 1.6$ m, $r_2 = 2.4$ m. with window . .	52
4.8	Bispectrum for blade-sphere with $r_0 = 1$ m.	53
4.9	3-D bispectral response for blade-sphere combination	54

4.10	Impulse response for noisy backscatter from blade-sphere (SNR= -30 dB)	55
4.11	Bispectrum for blade-sphere with noisy data (SNR= -30 dB)	56
4.12	Impulse response of frequency dispersive backscatter for blade-sphere. 57	
4.13	Bispectrum of frequency dispersive backscatter for blade-sphere. . .	58
4.14	Impulse response of frequency dispersive backscatter for blade-sphere. (single edge dispersion)	59
4.15	Bispectrum of frequency dispersive backscatter for blade-sphere with single edge dispersion	60
4.16	Bispectral response for fuselage at 0 degrees azimuth, 0 degrees ele- vation.	61
4.17	Bispectral response for fuselage and stabilizer at 0 degrees azimuth, 0 degrees elevation.	62
4.18	Bispectral response for wing at 0 degrees azimuth, 0 degrees eleva- tion.	63
4.19	Bispectral response for complete canonical aircraft at 0 deg. azimuth, 0 deg. elevation.	64
4.20	Scaled drawings for aircraft used in experimental study	65
4.21	Bispectral response for 747 at 0 degrees azimuth, 0 degrees elevation.	66
4.22	Bispectral response for 727 at 0 degrees azimuth, 0 degrees elevation.	67
4.23	Bispectral response for concord at 0 degrees azimuth, 0 degrees ele- vation.	68
4.24	Bispectral response for DC10 at 0 degree azimuth, 0 degree elevation.	69
4.25	Bispectral response for 707 at 0 degrees azimuth, 0 degrees elevation.	70
4.26	Bispectral response for 707 at 10 degrees azimuth, 0 degrees elevation.	71
4.27	Bispectral response for 707 at 20 degree azimuth, 0 degree elevation.	72
4.28	Bispectral response for 707 at 30 degree azimuth, 0 degree elevation.	73
4.29	Bispectral response for 707 at 0 degrees azimuth, 0 degrees elevation and $SNR = -5dB$	74
4.30	Conceptual diagram for bispectral radar target classification algo- rithm.	75

4.31	Diagram of bispectral radar target classification algorithm as implemented.	76
4.32	Classification performance assuming complete azimuth information. .	77
5.1	Conditional Probability Overlaps	80
5.2	Octant crossing primitive assignments.	87
5.3	Inscribed staircase region, 5 points	88
5.4	Circumscribed staircase region, 5 points	88
5.5	Octant crossing vs. coherent nearest neighbor	90
5.6	Single level crossing vs. nearest neighbor	91
5.7	Conversion to deterministic form, (a) non-deterministic automata set with labeled final states. (b) merged non-deterministic automata. (c) resulting deterministic automata	94

1. Executive Summary

This report documents a summary of the work accomplished during the first six months under the project entitled "Identification of Airborne Radar Targets" (Contract # N00014-86-K-0202). During this period of the renewed contract, the progress toward realizing the goals set forth in the statement of work has been rapid, and has produced a number of key interim results. In particular, we have:

1. Developed techniques to estimate and parameterize canonical scattering centers of a radar object. The results of this technique are compared with those obtained using an ARMA estimation technique for single polarization data.
2. Developed and evaluated the performance of a signal processing technique that estimates the polarization characteristics of target scattering centers. This technique incorporates polarization-diverse data to obtain a super-resolved down-range cross-section of the target showing polarization ellipses of the predominant scattering centers.
3. Evaluated the feasibility of using bispectrum processing techniques for the purpose of radar target characterization and identification. The results of this study have identified advantages of bispectrum processing for frequency-dispersive scatterers and indicate the possibility of identifying targets from the estimated bispectral responses.
4. Developed improved techniques for estimating the statistical parameters of observed symbol strings for the purpose of target identification based on structural pattern recognition. In addition, we have developed a formulation of the target identification algorithm that resembles a tree classifier. Reformulating the algorithm in this way reveals the structural nature of the classifier to the extent that a relative evaluation of the discrimination capability of particular symbols may be possible.

The remainder of this report is organized into chapters that more fully discuss progress and ongoing research in the areas mentioned above.

2. High Resolution Radar Target Modeling Using ARMA Models

This chapter discusses research high resolution modeling of radar data to obtain target impulse responses. The techniques are parametric, and rely on scattering center location estimation, and parameterizing the scattering center by various attributes. This chapter focuses on single polarization data. Two methods are considered. One is a canonical scattering center analysis, which employs nonlinear minimization techniques to obtain the estimate. The other approximates this canonical scattering model by an Autoregressive Moving Average (ARMA) model, and uses ARMA estimation techniques derived from the signal processing literature. The latter method is more computationally efficient than the former method.

We begin with a discussion of canonical scattering centers. We next present the ARMA modeling method, and briefly describe the algorithm which is used. Next we present simulation results obtained using compact range data measurements of model aircraft. Finally, we discuss the canonical scattering center estimation method.

2.1 Canonical Scatterers

It is well-known [1] that scattering of electromagnetic waves at high frequencies, i.e. at frequencies such that the wavelength is small compared to the scatterer, can be modeled as a set of independent scattering centers. There are several varieties of canonical scattering centers used in this process; typical examples are the point, edge and plate scatterers and the corner reflector [1].

If a target consisting of m scatterers is illuminated using a CW radar, then the backscattered field received by a linearly polarized antenna will give a signal of the form [2]:

$$y_k = \sum_{i=1}^m K_i e^{\frac{-j2r_i 2\pi f_k}{c}} (j2\pi f_k)^{t_i} \quad (2.1)$$

where K_i is the amplitude, r_i the relative range, and t_i the type of the i^{th} scatterer; f_k is the k^{th} frequency, and m is the number of scatterers. For the canonical scatterers in [2], t_i takes on the following values

$$t_i \in \{-1, -0.5, 0, 0.5, 1\} \quad (2.2)$$

In addition, for stepped frequencies, we can represent f_k by

$$f_k = f_0 + k\delta_f, \quad k = 0, 1, 2, \dots, N-1 \quad (2.3)$$

where f_0 , δ_f and N are given parameters of the system under consideration. The frequency f_0 represents the lowest frequency the radar system transmits and δ_f is the size of the frequency step. Estimation of the parameters in (2.1) from N measurements leads to a canonical scattering description of the target; see [2].

This model, while based on the physical properties of the scattering process, has the disadvantage of being non-linear. A non-linear estimator typically requires more data to converge to within a given distance of the correct estimate, and also suffers from the possibility of convergence to a false (local, but not global) minimum, leading to incorrect estimates.

We are currently investigating two estimators for this model. The first estimator uses the model (2.1) directly, and estimates the parameters of that model through a multi-step, non-iterative algorithm. If desired, the quality of the resulting estimates can be improved further by using the multi-step estimate as an initial guess for an iterative non-linear least-squares estimator. The second estimator uses an approximate model of (2.1) that allows linear estimation techniques, specifically an ARMA algorithm. The second algorithm is more computationally efficient, and has been studied more extensively.

The approximate model for linear estimation is obtained by replacing the $(j2\pi f_k)^t$ factor in (2.1) with ρ^k . By suitably adjusting the amplitude, the approximate model can be made to match the original model if the bandwidth involved is not too large. Thus we arrive at:

$$y_k = \sum_{i=1}^m d_i p_i^k \quad (2.4)$$

where d_i is in general not equal to K_i in (2.1) because of the approximation involved. The variable p_i can be found from:

$$p_i = \rho_i e^{-j2\pi r_i/R} \quad (2.5)$$

In practice the absolute range is not used; instead, r_i represents the range relative to a zero range reference point. R then represents the maximum unambiguous range

$$R = \frac{c}{2\delta_f}.$$

It should be noted that for $t = 0$ the correspondence is exact (ρ will be 1).

The energy associated with a single scattering center is the square of the absolute value of its contribution to the amplitude, or

$$P_i = \sum_{k=0}^{N-1} |d_i|^2 |p_i|^{2k} = |d_i|^2 \frac{1 - \rho_i^{2N}}{1 - \rho_i^2} \quad (2.6)$$

Equations (2.4) and (2.6) will be used to form the approximate parametric model of target scattering.

2.2 ARMA Models

In this section we will discuss estimation techniques for the approximate model. For a more detailed analysis of this model and the corresponding estimation techniques, see [3] and [4].

Equation (2.4) can be formed as the solution of a linear difference equation,

$$y_k + \sum_{i=1}^m a_i y_{k+i} = \sum_{i=0}^{m-1} c_i \delta_{k+i} \quad (2.7)$$

$$A(q^{-1})y_k = C(q^{-1})\delta_k \quad (2.8)$$

where δ_k is the unit impulse sequence. It can be shown [5] that the $\{p_i\}$ in equation (2.4) are the roots of the $A(z)$ polynomial, and the coefficients $\{d_i\}$ the partial fraction residues of $C(z)$ and $A(z)$. It should be observed that this means that the radar cross section as a function of relative range can be found by taking the square of the absolute value of

$$\begin{aligned} Y(r) &= \frac{C(e^{j\pi(1-2r/R)})}{A(e^{j\pi(1-2r/R)})} \\ &= \sum_{i=1}^m \frac{d_i}{e^{j\pi(1-2r/R)} - p_i}, \quad 0 \leq r \leq R \end{aligned}$$

By observing that for $k > 0$ the right hand side in (2.7) equals zero, we can find a linear least squares estimator for the $A(z)$ polynomial:

$$\begin{bmatrix} y_{M+1} & y_M & \cdots & y_1 \\ y_{M+2} & y_{M+1} & \cdots & y_2 \\ \vdots & \vdots & \ddots & \vdots \\ y_{N-1} & y_{N-2} & \cdots & y_{N-M-1} \end{bmatrix} \begin{bmatrix} a_M \\ \vdots \\ a_1 \\ 1 \end{bmatrix} \approx 0 \quad (2.9)$$

where M is some integer at least equal to m and where equality will hold for noiseless data that fits the model perfectly. Appropriate ways for choosing M are discussed in [4].

The performance of this estimator can be improved through the use of the singular value decomposition (SVD) as follows: find the SVD of the matrix Y on the left hand side of (2.9); let

$$\sigma_1 \geq \sigma_2 \geq \cdots \geq \sigma_{M+1} \geq 0.$$

be the resulting singular values. Set $\sigma_{n+1} \dots \sigma_{M+1}$ equal to zero, reconstruct Y and solve (2.9) with the new Y . The value of n is chosen to be such that the first large drop in the value of the $\{\sigma_i\}$ falls between σ_n and σ_{n+1} . This choice is motivated by the ability of the SVD to partially reject the effects of noise and unmodeled dynamics on the estimate. This issue is discussed in further detail in [4].

Once the $A(z)$ polynomial has been found, the $\{p_i\}$ can be estimated through standard polynomial rootfinding techniques. Given the $\{p_i\}$, the $\{d_i\}$ can be found from

$$\begin{bmatrix} \hat{p}_1^0 & \cdots & \hat{p}_M^0 \\ \vdots & & \vdots \\ \hat{p}_1^{N-1} & \cdots & \hat{p}_M^{N-1} \end{bmatrix} \begin{bmatrix} \hat{d}_0 \\ \vdots \\ \hat{d}_{N-1} \end{bmatrix} - \begin{bmatrix} y_0 \\ \vdots \\ y_{N-1} \end{bmatrix} \approx 0 \quad (2.10)$$

where \hat{p}_i is the estimate for p_i found above.

Above we computed an estimate of a polynomial $A_M(z)$ of order $M > m$, and a corresponding set of M zeros $\{p_i\}_{i=1}^M$. We also computed amplitudes corresponding to these zeros. The next step is to separate the m zeros that correspond to the

radar target (signal zeros) from the remaining spurious zeros. The zero separation process relies on the observation that since the spurious zeros correspond to modes that are not present in the data, their estimated energy should be low. To take advantage of this property, we use the following strategy. First, the amplitudes $\{d_i\}_{i=1}^M$, corresponding to all M zeros are found using equation (2.10). Then, the energy of each mode is computed using equation (2.6). The m zeros whose corresponding energy is the highest are kept and the remaining ones are discarded. Then, the energy estimates for the m kept zeros can be refined by recomputing the amplitude estimation using (2.10) with only the m selected zeros. However, since the energies for the discarded zeros is low, the difference between the two estimates should generally be small, so this refinement step may be omitted.

2.3 Experimental Results

In this section we describe results obtained with both types of algorithm. We first describe results obtained by applying the ARMA algorithm to data obtained from the ESL Compact Range and then present results from the application of the canonical estimator to simulated data.

2.3.1 Results from Applying ARMA Techniques to Compact Range Data

The main aim of this section is to demonstrate that the ARMA type algorithm presented above is robust to changes in model order M and number of singular values kept n , performs well in the presence of noise and achieves consistent results across different frequency ranges. On the other hand, the algorithm readily detects differences between aircraft and is able handle changes in aspect angle.

Figure 2.1 shows estimated responses for a 1:130 model of the Concord using $N = 30$ data points taken evenly spaced from 18–26 GHz (corresponds to 138–200 MHz on a full-size Concord) and model orders $M = 5$ and 10, keeping $n = 3$ singular values and $m = 2$ zeros.

Figure 2.2 shows estimates for $M = 10$ order model from the same data as above, keeping $n = 3, 5$ and 7 singular values and $m = 2$ zeros.

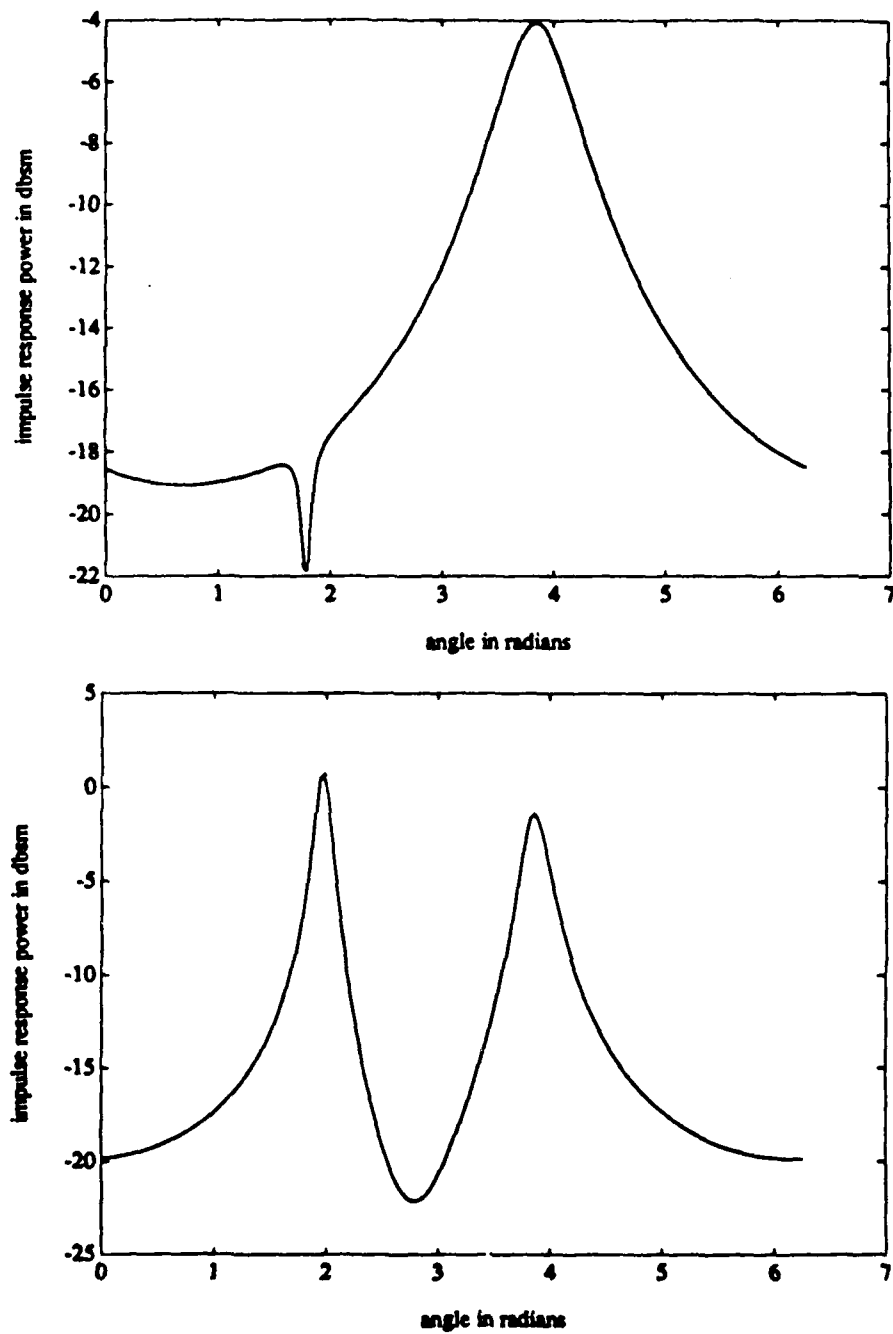


Figure 2.1: Response of the Concord for $N = 30$, $M = 5$ and 10 , $n = 3$, $m = 2$. Data taken between 18–26 GHz.

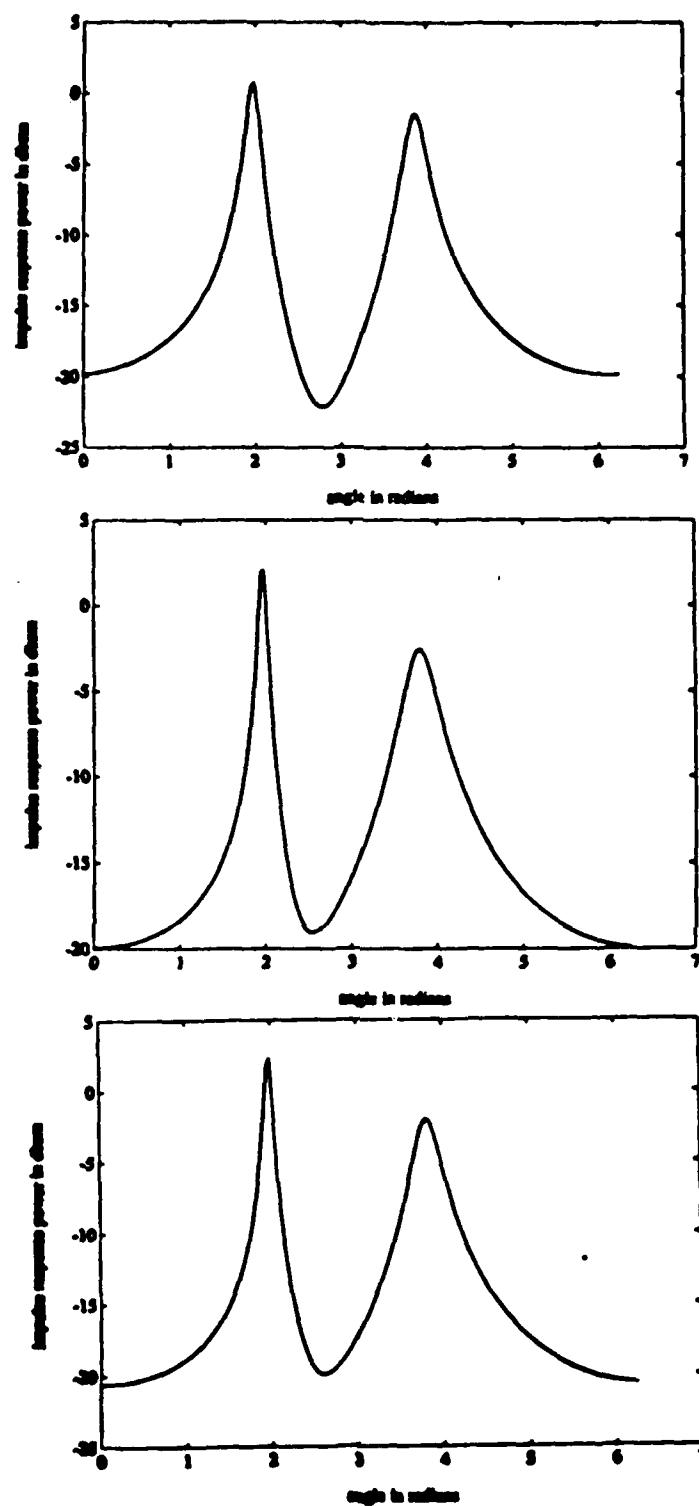


Figure 2.2: Response of the Concord for $N = 30$, $M = 10$, $n = 3, 5$ and 7 , $m = 2$. Data taken between 18–26 GHz.

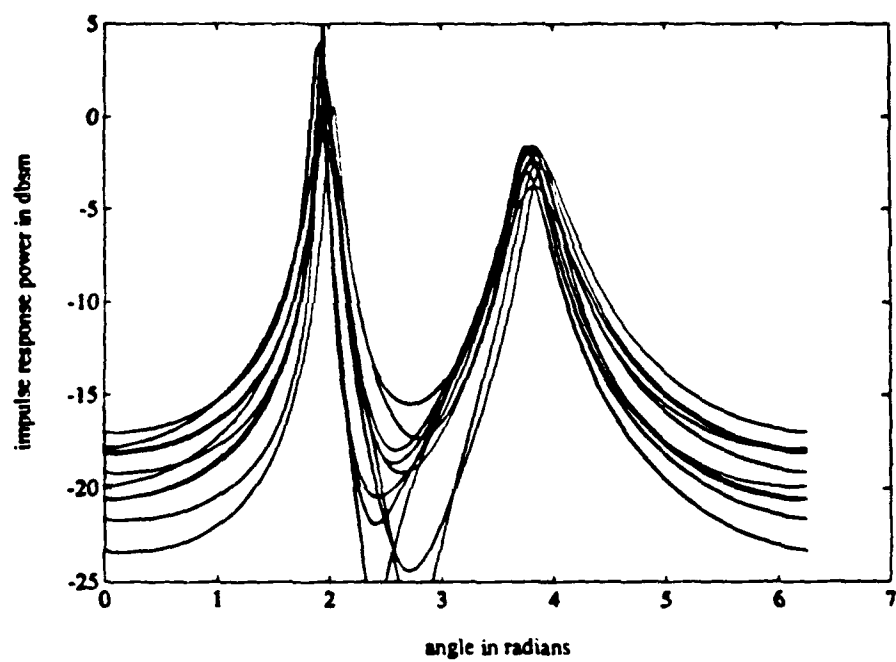


Figure 2.3: Response of the Concord for $N = 30$, $M = 10$, $n = 5$, $m = 2$. Data taken between 18–26 GHz with 10 dB SNR.

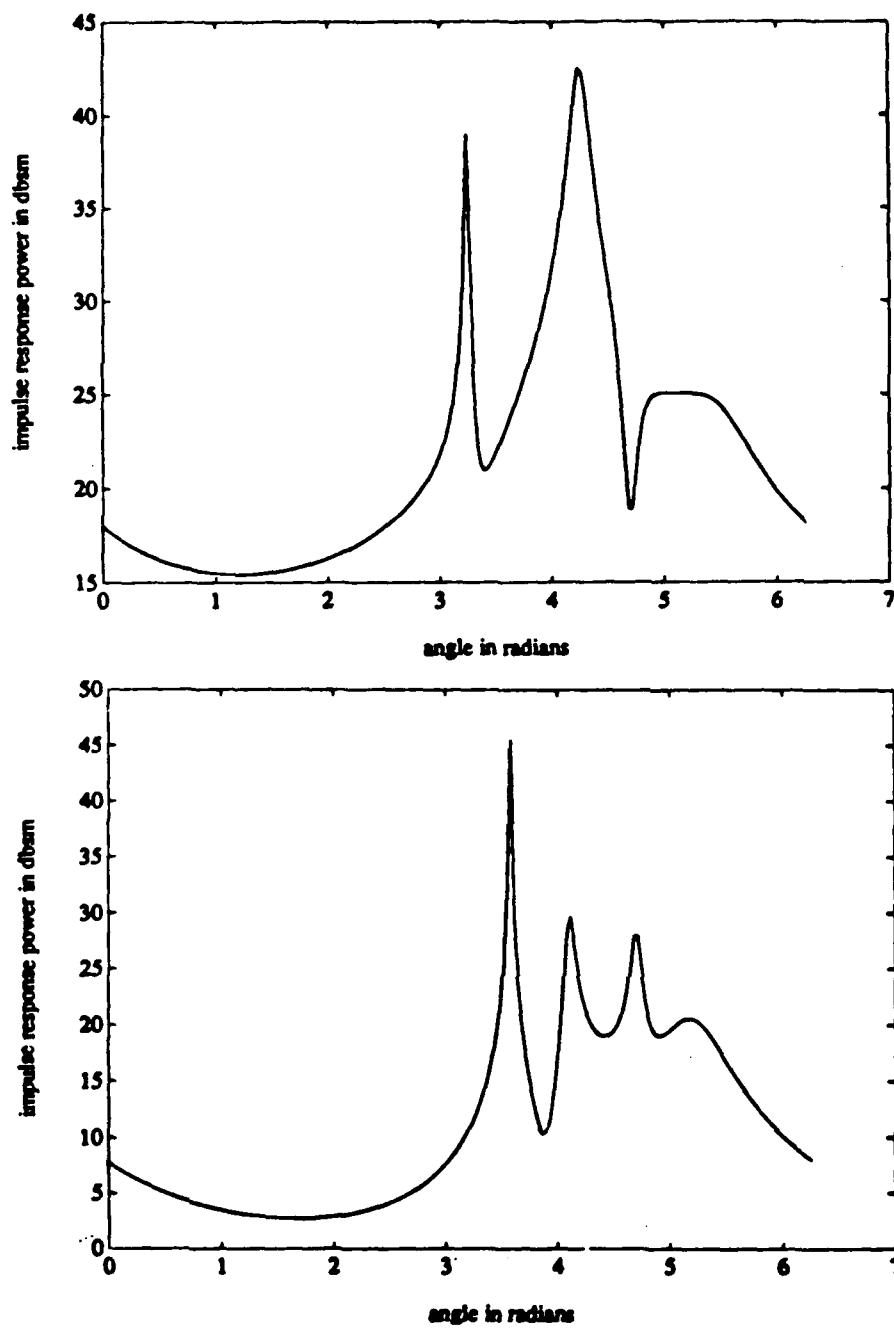


Figure 2.4: Response of the Concord for $N = 20$, $M = 10$, $n = 7$, $m = 4$. Data taken between 6.25–12 GHz at 0 and 20 degree aspect angle.

Figure 2.3 shows estimates for $M = 7$, $n = 5$ and $m = 2$ but with Gaussian noise added at 10 dB SNR.

The above figures demonstrate by their similarity that the algorithm is robust with respect to the effects of noise, choice of order and choice of the number of singular values to keep.

Figure 2.4 shows estimated responses for the Concord taken from $N = 20$ data points in a 6.25–12 GHz range (48–92 MHz for a full-scale target) using $M = 10$, $n = 7$ and $m = 4$. We have used two data sets here, one taken at an aspect angle of zero degrees, the other at 20 degrees. The figure clearly shows the relation between the two estimated responses. We can see that the second large peak has split into two peaks at 20 degrees, and all the scattering centers are a bit closer to each other, as a result of the apparent foreshortening of the target in the downrange direction.

For reference, Figure 2.5 gives the result of an IFFT performed on the 18–26 GHz data, and Figure 2.6 gives a properly scaled picture of the Concord.

2.3.2 Direct Estimation of the Canonical Scatterer Model

In this section we detail an algorithm that directly estimates the $\{K_i\}$, $\{r_i\}$ and $\{t_i\}$ parameters of equation (2.1). The order of estimation is first the $\{r_i\}$, then the $\{t_i\}$ and finally the $\{K_i\}$ parameters.

The $\{r_i\}$ parameters are estimated in the same way as as for the approximate model in the previous section. We then find the $\{t_i\}$ parameters by applying the following three step procedure for all scatterers.

1. For the i^{th} scatterer, modulate the sequence $\{y_k\}$ with $e^{\frac{j2r_i 2\pi f_k}{c}}$, thus translating the i^{th} scatterer to relative range zero.
2. Apply a low-pass filter to the modulated data y_k . Note that this is a low-range filter, *not* a low-frequency filter. This filtering operation should leave the i^{th} scatterer as the only component of the filtered data. Note that it is important that the filter have linear phase for the third step to succeed.
3. The filtered data can now be described by

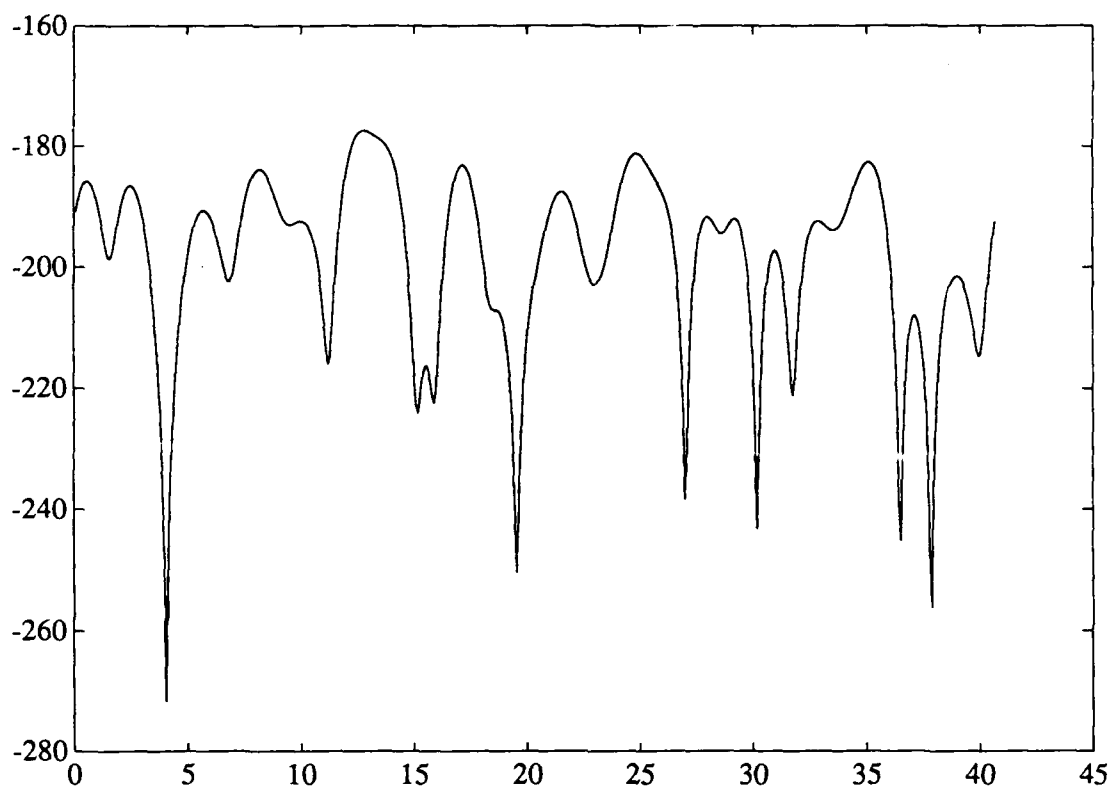
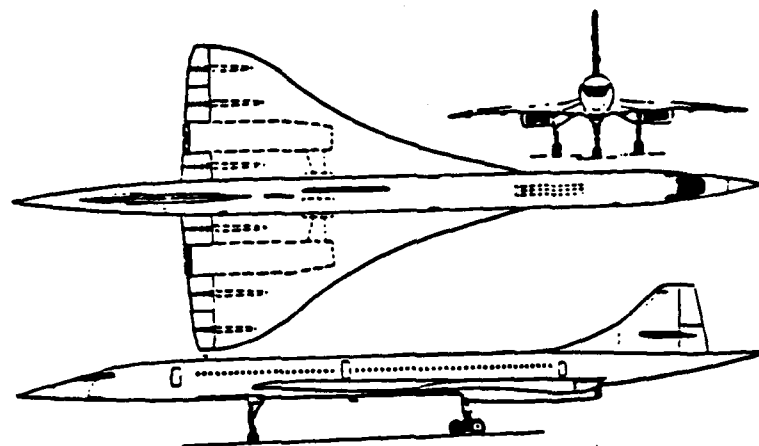


Figure 2.5: Concord, 18-26 GHz, FFT using 30 data points zero padded to 512, 0 degree aspect angle.



External Dimensions:

Length overall	202 ft 3.6 in (61.66m)
Height overall	40 ft 0.0 in (12.19m)
Wing span	83 ft 10.0 in (25.56m)

Figure 2.6: Scaled Picture of the Concorde.

$$y'_k = K_i(j2\pi f_k)^{t_i}$$

From which it follows that

$$\text{Ln } y'_k = \text{Ln} K_i + t_i \text{Ln } (j2\pi f_k) \quad (2.11)$$

where **Ln** is the main branch of the complex natural logarithm. The parameters $\{t_i\}$ can be found from a least squares solution to equation (2.11). and finding the least squares solution.

Finally, the $\{K_i\}$ can be found using a least squares method in equation (2.1), using the estimates for $\{r_i\}$ and $\{t_i\}$ found above.

If desired, the estimates found with the aid of the multi-step procedure above can be used as an initial guess for a non-linear least squares estimator. The accuracy of the estimates for simulated data has been sufficient that this has not been necessary so far, but we anticipate that such refinement may be needed for real data.

3. Exponential Modeling of Fully Polarized Radar Return

The horizontal and vertical radar return from a target illuminated with stepped frequency circularly polarized radiation can each be modeled a sum of complex exponentials. The scattering points of the target are thus the poles of these models, and amplitudes associated with each pole represent the scatterer's horizontal and vertical return. One approach is to use this modeling on both the horizontal data and the vertical data independently. This model can then be used to identify the target.

However, it is reasonable to assume that if a scattering center appears in the horizontal return then it is also present in the vertical return. Thus when estimating the poles of the model, both the horizontal and vertical information are used simultaneously to estimate the ranges of the scattering centers. To make the estimate more resilient to noise we employ Singular Value Decomposition (SVD) on the associated linear prediction matrix. Also, since scatterers can be expected to cause peaky responses, poles in the linear prediction model which are not within a certain distance from the unit circle are eliminated. Finally, we estimate the horizontal and vertical amplitude characteristics independently using the appropriate polarization data.

Once the model has been determined, the angle at which the poles appear in the z -plane represent the downrange location of each of the scatterers. The horizontal and vertical amplitudes associated with each pole contain the information about that scatterer's polarization effect on the incident radar wave. These polarizations are in general elliptical and, along with the scatterer's range, can be used to identify the target.

3.1 Modeling the Scatterers

Assume that two sets of N data points are generated from M complex exponentials with white Gaussian noise added, where each set represents the horizontal and vertical return from a left circularly polarized incident wave, s_{hl} and s_{vl} respectively.

$$\begin{bmatrix} s_{hl}(n) \\ s_{vl}(n) \end{bmatrix} = \sum_{k=1}^M \begin{bmatrix} a_{hk} \\ a_{vk} \end{bmatrix} p_k^n + \begin{bmatrix} w_h(n) \\ w_v(n) \end{bmatrix} \quad n = 1, \dots, N. \quad (3.1)$$

Where p_k is the k th common pole, a_{hk} is the horizontal amplitude associated with that pole, and a_{vk} is the vertical amplitude associated with the same pole. The backward linear prediction equations can then be set up as follows[6][7][8].

$$\begin{bmatrix} s_{hl}(2) & s_{hl}(3) & \dots & s_{hl}(L+1) \\ s_{hl}(3) & & & \vdots \\ \vdots & & & \vdots \\ s_{hl}(N-L+1) & \dots & \dots & s_{hl}(N) \\ s_{vl}(2) & s_{vl}(3) & \dots & s_{vl}(L+1) \\ s_{vl}(3) & & & \vdots \\ \vdots & & & \vdots \\ s_{vl}(N-L+1) & \dots & \dots & s_{vl}(N) \end{bmatrix} \begin{bmatrix} \hat{b}_1 \\ \vdots \\ \hat{b}_L \end{bmatrix} = - \begin{bmatrix} s_{hl}(1) \\ \vdots \\ \vdots \\ s_{hl}(N-L) \\ s_{vl}(1) \\ \vdots \\ \vdots \\ s_{vl}(N-L) \end{bmatrix} \quad (3.2)$$

or

$$S\hat{b} = -s \quad (3.3)$$

where L is the order of prediction, and \hat{b} is the coefficient vector of the polynomial $\hat{B}(z)$ given by

$$\hat{B}(z) = 1 + \hat{b}_1 z^{-1} + \dots + \hat{b}_L z^{-L} \quad (3.4)$$

Note that both sets of data are used simultaneously to estimate a single set of prediction coefficients.

The solution involves forming the matrix $[s : S]$, performing a Singular Value Decomposition (SVD) on it, then truncating all but the first M singular values to arrive at a better estimate $[\hat{s} : \hat{S}]$. Next, \hat{b} is found using the pseudoinverse of \hat{S} ,

$$\hat{b} = -\hat{S}^+ \hat{s}. \quad (3.5)$$

Now the estimated poles can be determined as:

$$\hat{p}_i = \frac{1}{\text{root}_i(\hat{B}(z))} \quad i = 1, \dots, L \quad (3.6)$$

Since scatterers result in peaky responses, those poles which do not lie within a given annular region about the unit circle can be eliminated from the model. The following criterion has been found to work well for radar data:

$$\frac{1}{100} < |\hat{p}_i|^N < 100 \quad (3.7)$$

We keep only those poles in (3.6) which satisfy (3.7). Once these L' poles have been determined, the amplitude equations for both the horizontal and vertical components can be formed.

$$\begin{bmatrix} \hat{p}_1^1 & \dots & \hat{p}_{L'}^1 \\ \vdots & & \vdots \\ \hat{p}_1^N & \dots & \hat{p}_{L'}^N \end{bmatrix} \begin{bmatrix} \hat{a}_{h1} & \hat{a}_{v1} \\ \vdots & \vdots \\ \hat{a}_{hL} & \hat{a}_{vL} \end{bmatrix} = \begin{bmatrix} s_{hl}(1) & s_{vl}(1) \\ \vdots & \vdots \\ s_{hl}(N) & s_{vl}(N) \end{bmatrix} \quad (3.8)$$

or

$$\hat{P}\hat{A} = S_a \quad (3.9)$$

Total least squares can now be used to estimate the amplitudes.

$$\hat{A} = (\hat{P}^H \hat{P})^{-1} \hat{P}^H S_a \quad (3.10)$$

3.2 Determining Scatterer Locations and Associated Polarizations

Now that we have \hat{a}_{hi} , \hat{a}_{vi} , and \hat{p}_i , for each scatterer i , we can determine its range \hat{r}_i and its polarization in terms of tilt $\hat{\tau}_i$, ellipticity $\hat{\epsilon}_i$, and major axis \hat{A}_i . They are given by the following:

$$\hat{r}_i = \angle \hat{p}_i \quad (3.11)$$

$$\hat{\tau}_i = \frac{1}{2} \tan^{-1} \left(\tan(2\hat{\gamma}_i) \cos(\hat{\delta}_i) \right) \quad (3.12)$$

$$\hat{\epsilon}_i = \frac{1}{2} \sin^{-1} \left(\frac{\sin(2\hat{\gamma}_i)}{\sin(\hat{\delta}_i)} \right) \quad (3.13)$$

$$\hat{A}_i = \frac{\sqrt{|\sin(\hat{\delta}_i)| |\sec(\hat{\tau}_i)|}}{\sqrt{\frac{1}{\hat{E}_{1i}^2} - \frac{2 \tan(\hat{\tau}_i) \cos(\hat{\delta}_i)}{\hat{E}_{1i} \hat{E}_{2i}} + \frac{\tan^2(\hat{\tau}_i)}{\hat{E}_{2i}^2}}} \quad (3.14)$$

where

$$\hat{\gamma}_i = \tan^{-1} \left(\frac{\hat{E}_{2i}}{\hat{E}_{1i}} \right) \quad (3.15)$$

and

$$\hat{\delta}_i = \angle \hat{a}_{vi} - \angle \hat{a}_{hi} \quad (3.16)$$

$$\hat{E}_{1i} = |\hat{a}_{hi}| \quad (3.17)$$

$$\hat{E}_{2i} = |\hat{a}_{vi}| \quad (3.18)$$

The ranges of a target's scatterers and their respective polarization characteristics can thus be used to identify the target.

3.3 Simulation Results

The above estimation procedure was applied to data obtained from compact range measurements of several small aircraft models; in particular, we used scale models of the 707, 727, 747, DC10, and the Concord. The ESL compact range was used to measure horizontal transmit with horizontal and vertical receive and vertical transmit with horizontal and vertical receive, $s_{hh}(f)$, $s_{vh}(f) = s_{hv}(f)$, and $s_{vv}(f)$ respectively. The measurements were made for frequencies f between 1.5 and 12 GHz at 50 MHz steps, thus resulting in 211 data points for each polarization. From this data, $s_{hl}(f)$ and $s_{vl}(f)$ are found using the following transformation:

$$\begin{bmatrix} s_{hl}(f) \\ s_{vl}(f) \end{bmatrix} = \begin{bmatrix} s_{hh}(f) & s_{hv}(f) \\ s_{vh}(f) & s_{vv}(f) \end{bmatrix} \begin{bmatrix} 1 \\ j \end{bmatrix} \frac{1}{\sqrt{2}} \quad (3.19)$$

The following simulations were done with $N = 80$ data points from the upper half of frequency range. In all cases, the nose on aspect angle data was used.

The models range from about 23 to 43 cm in length, so an unambiguous range $R = 75\text{cm}$ is needed to get resolution between the model's individual scatterers. Since $\Delta f = \frac{c}{2R}$, where c is the speed of light, for this R , $\Delta f = 200\text{MHz}$. This corresponds to every fourth point in the data set. To allow use of all 80 points, the backward prediction equations were written so as to interleave four sets of 20

points each. The amplitudes associated with each pole similarly used the four sets of data.

Finally, model order and the number of singular values to keep were chosen as: $L = 10$ and $M = 5$. The results for each plane with no noise added to the data appear in Figs. 3.1-3.5. Each scatterer is represented by an ellipse which describes its polarization effect at the appropriate range. The scale is in meters and is for ellipse location. The ellipse factor of .2 can be used to multiply the range scale to see ellipse magnitudes. A scale plan view for each plane also appears in order to match up ellipses with their physical scatterer.

ellipse factor=0.2

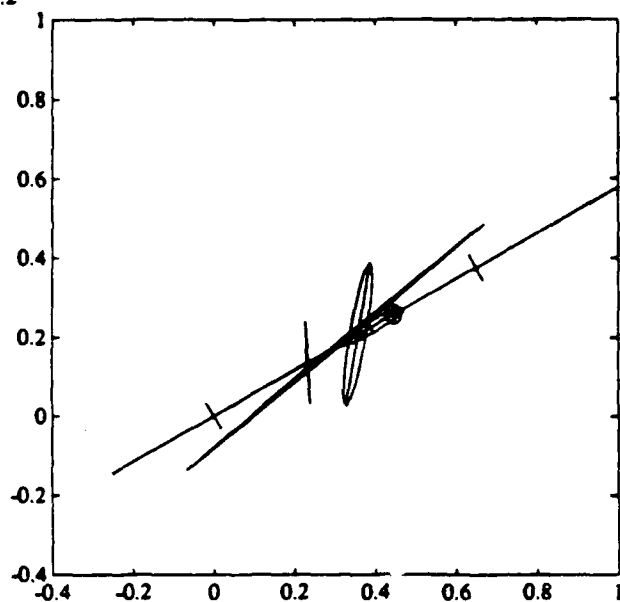


Figure 3.1: 707 Scatterers and Polarizations

ellipse factor=0.2

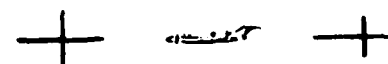
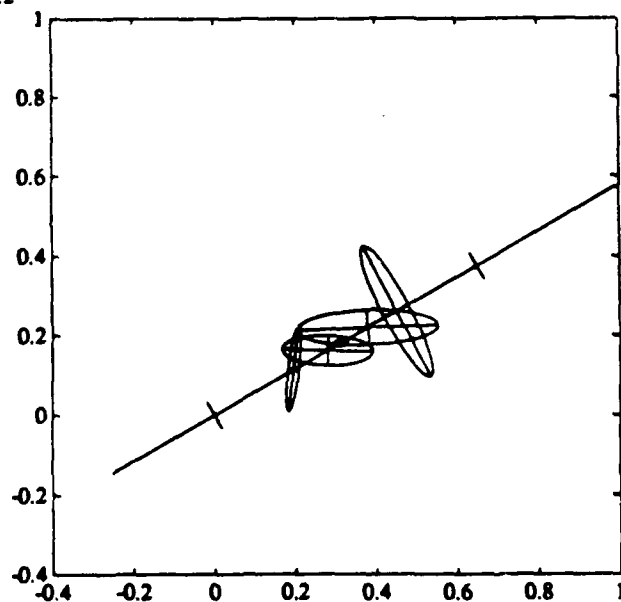


Figure 3.2: 727 Scatterers and Polarizations

ellipse factor=0.2

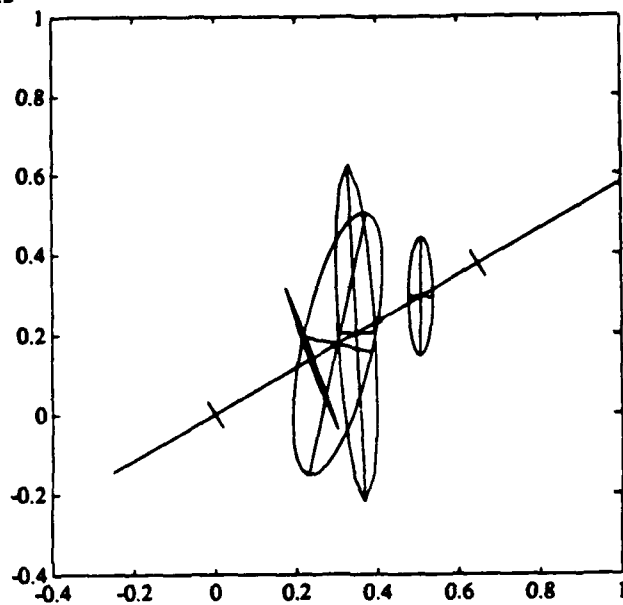


Figure 3.3: 747 Scatterers and Polarizations

ellipse factor=0.2

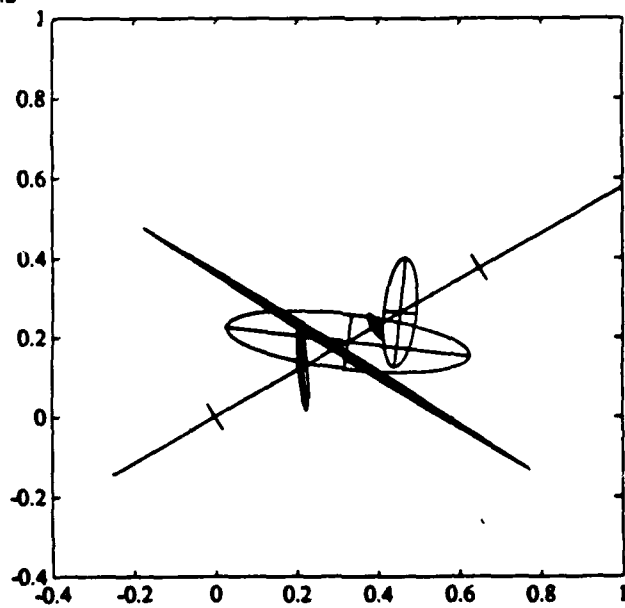


Figure 3.4: DC10 Scatterers and Polarizations

ellipse factor=0.2

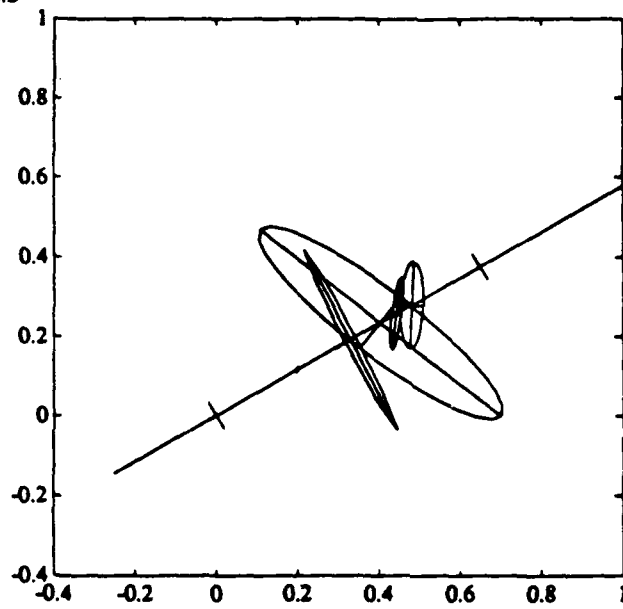
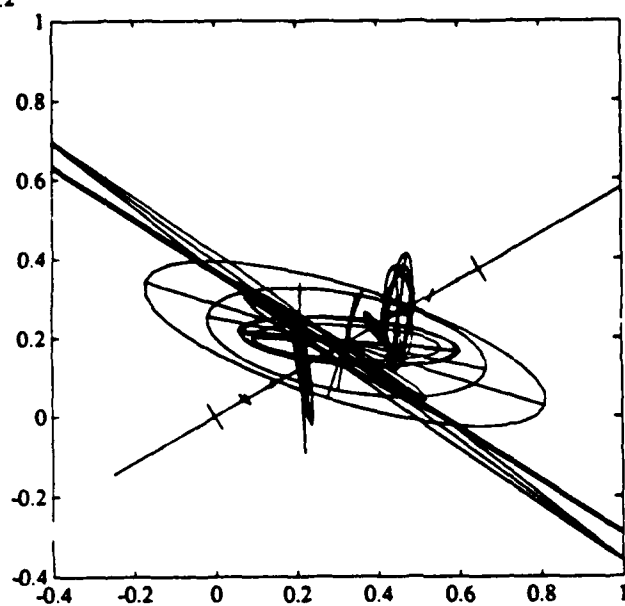


Figure 3.5: Concord Scatterers and Polarizations

Noise was then added for SNRs of $10dB$, $5dB$, and $0dB$ to the DC10 data. Five simulations with different noise realizations for each SNR appear in Figures 3.6–3.8. Since the noise tends to make discrimination of ellipses difficult, a plot of range vs. the length of the hypotenuse between each ellipse's major and minor axis also appears in each figure.

ellipse factor=0.2



ellipse factor=0.2

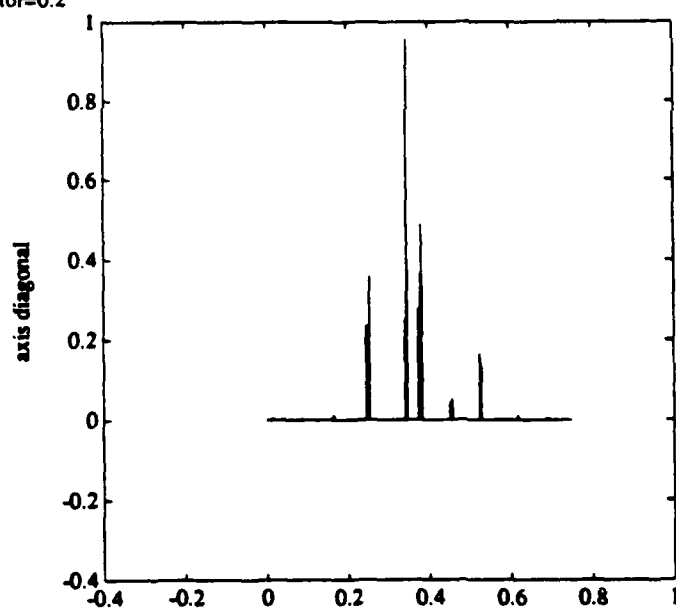
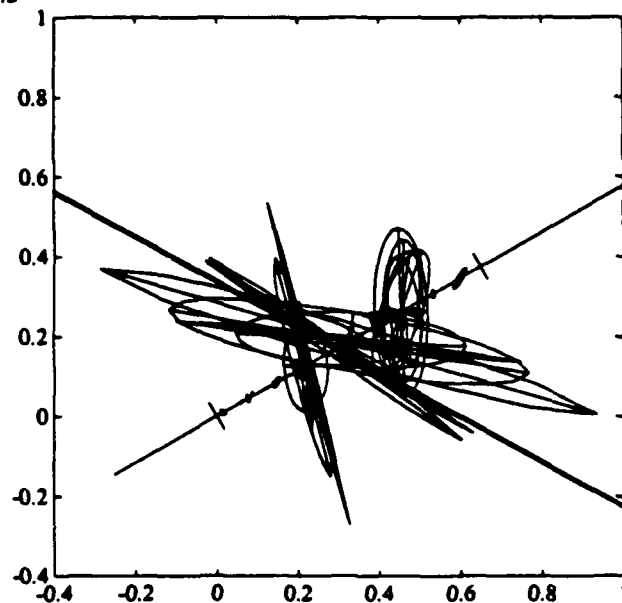


Figure 3.6: DC10 Scatterers and Polarizations, SNR of 10dB

ellipse factor=0.2



ellipse factor=0.2

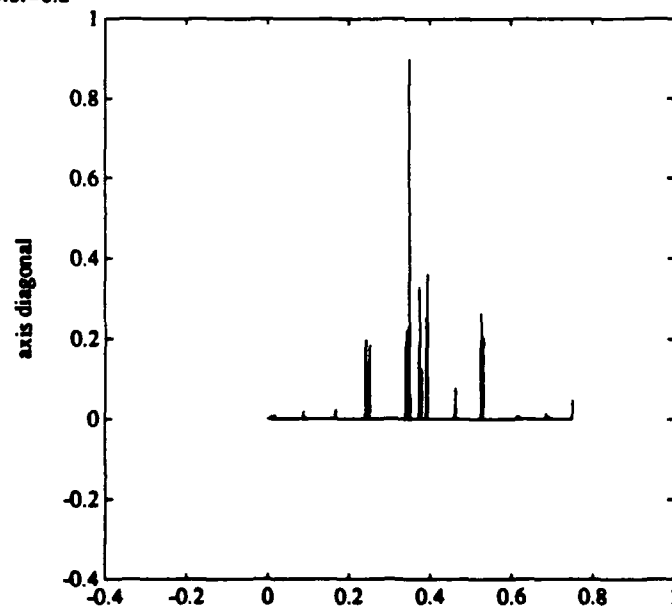
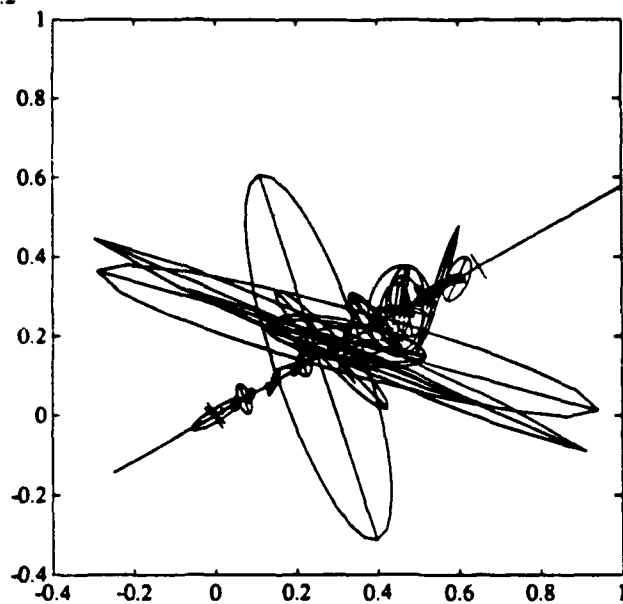


Figure 3.7: DC10 Scatterers and Polarizations, SNR of 5dB

ellipse factor=0.2



ellipse factor=0.2

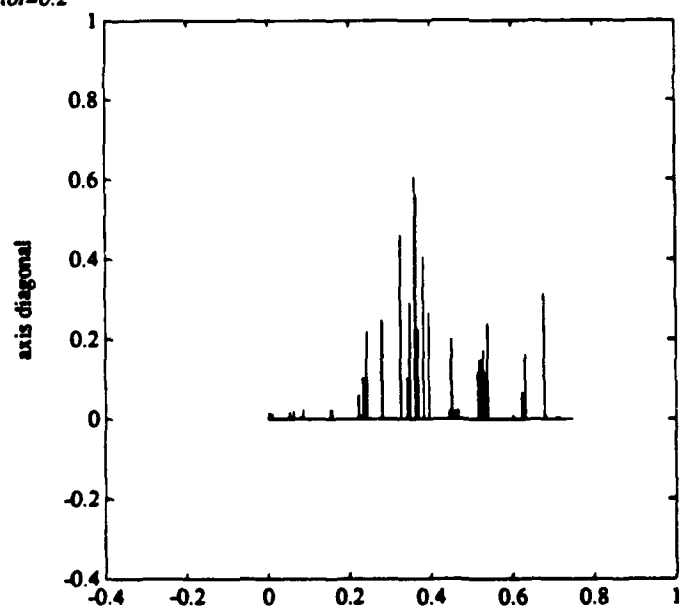


Figure 3.8: DC10 Scatterers and Polarizations, SNR of 0dB

The simulation results demonstrate that the procedure produces target signatures which are unique and identifiable and that it stands up well in noise, particularly in finding the existence and range of a scatterer. This is due to the fact that both sets of data, s_{hl} and s_{vl} , are used to determine the poles of the model. Even at 0dB SNR the scattering centers are quite distinguishable, particularly in the hypotenuse plots. The polarization ellipse for each scatterer, however, is not as robust since its components are each derived from half of the data separately. Still, the scatterer center location makes identification of the target possible in these high noise situations. The scatterers also appear at downrange locations which correspond with features of the planes such as wings, engine inlets, rudders, etc., which gives physical significance to the model and helps to justify its use.

4. A Study of The Bispectral Estimates of Radar Signals And Application To Radar Target Identification

4.1 Introduction

This Chapter is concerned with the application of bispectrum estimation to the analysis of radar signatures. The recent interest in bispectrum estimation is motivated by the broad area of applications of higher order spectral estimates, especially the bispectrum. Problems such as phase decoupling, signal nonlinearities and skewness from Gaussian-like features can be solved and better understood using bispectrum estimation. The use of higher order spectra is not an alternative for lower order spectral analysis but rather a complementary process. Many features embedded in measured data may not appear in lower order spectral analysis or could be misinterpreted or misread. High order spectra may uniquely identify such features and present them in a way which leaves less room for misinterpretation.

Radar measurement data contain a wide spectrum of information that corresponds to various scattering mechanisms. In this study an attempt is made to use bispectral analysis to identify such mechanisms. This attempt is motivated by the fact that such mechanisms are often confused using first order spectral analysis. Moreover, radar targets at certain signal to noise ratio and certain conditions of azimuth and elevation may have similar lower order spectral responses but different higher order spectral responses. Thus, the bispectrum can be used to discriminate among targets that differ in fine details only.

Therefore, the two main reasons for studying bispectrum in radar signature analysis is to recover complex scattering features and to discriminate among targets that differ in fine details rather than major features. Also, in this study we looked at bispectral responses for frequency dispersive scatterers and found some interesting advantages of the bispectrum under these conditions. Moreover, due to the correlation involved in bispectrum estimation, the behavior of bispectral responses under conditions of high noise is relatively less sensitive to noise corruption than lower order spectral responses. Finally an attempt is made to classify radar targets based on the corresponding bispectral responses.

4.2 Problem Formulation: Birange Profile Theory

Radar scattering from an object is often measured as amplitude and phase at a set of evenly spaced frequencies. This permits a transformation to the time domain and thus the range domain by taking an inverse Fourier transform of the data. The result is called the radar target impulse response [9]. In general there is a one to one relationship between specific scattering mechanisms and the time such mechanisms appear in the impulse response. One of the difficulties that this type of analysis has is that complex targets often have multiple interactions. The result is that many of the terms in the impulse response are related to the interactions rather than due to the result of simple subcomponent scattering. Many of these multiple interaction mechanisms can be identified as such by the application of the bispectrum to the radar scattering data.

Also, this study indicates that the individual target scattering mechanisms are more easily observed using the bispectrum under conditions of high noise or target dispersive effects. It will be shown that these bispectral responses constitute robust features which may be used in radar target identification schemes.

The radar scattering from a complex target can be effectively modeled as a sequence of discrete scatterers. With this model each element of the set of complex radar scattering data

$$\tilde{S}_p(f_j) = A_p \exp(-j2\pi R_p f_j / c), \quad (4.1)$$

where

$$\tilde{S}_p(f_j) = \begin{array}{l} p^{th} \text{scattering coefficient at} \\ j^{th} \text{ frequency} \end{array}$$

$$A_p = \begin{array}{l} \text{amplitude of } p^{th} \text{ scattering} \\ \text{coefficient} \end{array}$$

$$R_p = \begin{array}{l} \text{line of sight range between} \\ \text{scatterers and radar zero phase} \\ (\& \text{ time) reference plane.} \end{array}$$

$$f_j = j^{th} \text{ radar carrier frequency}$$

$$c = \text{speed of light.}$$

This can be usefully converted to scalar form by simply taking the real part of the scattering value.

$$\Re\{\tilde{S}_p(f_j)\} = A_p \cos(2\pi R_p f_j / c) \quad (4.2)$$

Note that when data are represented in this form for the scattering from a particular single point scatterer at a particular range from the radar phase zero reference plane (which may be located near or on the target), a sinusoidal variation in the data as a function of frequency results. The amplitude of the sinusoid is proportional to the scattering coefficient of the scatterer, and the periodicity of the sinusoidal variation (as a function of radar carrier frequency) of the real part of the scattered signal is proportional to the line of sight distance of the scatterer to the zero phase reference plane. If the scatterers do not interact, then the total received signal will have the form

$$\tilde{S}_t(f_j) = \sum_p A_p \cos(2\pi R_p f_j / c) \quad (4.3)$$

Note that computation of the spectrum of \tilde{S}_t will yield values of A_p for each R_p . Note on the other hand that if the scatterers interact (multiple interaction), then a signal scattered from the latter part of a particular target will be influenced (or modulated) by interaction with components of the target closer to the radar. This interaction with other parts of the radar target prior to scattering from a particular object on the radar target results in modulation-like effects in the range domain profile which can be uniquely identified when the bispectral estimation process is applied to \tilde{S}_t .

The definition of the bispectrum is the two dimensional Fourier transform of the third moment sequence. In this study the bispectrum is a birange profile obtained by computing a two dimensional Fourier transform of the third order autocorrelation function which is function of frequencies f_1, f_2 in the two dimensional frequency domain.

$$R_{S_t}(f_1, f_2) = E\{\tilde{S}_t(f_j)\tilde{S}_t(f_j + f_1)\tilde{S}_t(f_j + f_2)\} \quad (4.4)$$

$$B_{S_t}(R_1, R_2) = \sum_{f_1} \sum_{f_2} R_{S_t}(f_1, f_2) \exp(-j2\pi/c[R_1 f_1 + R_2 f_2]) \quad (4.5)$$

where $E\{\cdot\}$ stands for the expected value and $R_{S_t}(f_1, f_2)$ is the third moment sequence of $\tilde{S}(t)$. The birange is denoted by $B_{S_t}(R_1, R_2)$ where R_1, R_2 belong to the two dimensional down range domain.

The bispectral estimates in this study are computed using the indirect classical method which is based on computing an estimate of the third moment sequence. Windowing can also applied to the estimates of the autocorrelation values. In this study the optimum window (minimum bispectrum bias supremum) [10,11] is used.

The above definition can be used as an indirect way to estimate the bispectrum but to get some kind of a physical insight of what the bispectrum really means it is better to use the following which is considered as a direct way of estimating the bispectrum.

$$y(r) = \frac{1}{N} \sum_0^N \tilde{S}(f) \exp(+j2\pi \frac{fr}{N}) \quad (4.6)$$

$$B_{S_t}(r_1, r_2) = \beta y(r_1)y(r_2)y^*(r_1 + r_2) \quad (4.7)$$

where $y(r)$ is the impulse response and $B_{S_t}(R_1, R_2)$ is the direct estimate of the birange and β is a constant ($\beta = (\frac{N}{f_s})^2$, where f_s is the sampling frequency of the radar frequency data. Thus, if $y(r)$ is the impulse response of the radar backscatter then the birange $B_{S_t}(R_1, R_2)$ is nonzero only when $y(r_1)$, $y(r_2)$, and $y(r_1 + r_2)$ are not equal to zero. This is mostly the case when we have an interaction term among different scatterers. Notice that $b(r_1, r_1) = \beta y^2(r_1)y(2r_1)$ which indicates that there exist scatterers at r_1 and $2r_1$ respectively. Also, it is important to notice that;

$$b(r_1, 0) = y(r_1)y(0)y^*(r_1) \quad (4.8)$$

which means that for the bispectrum to exist at either time (range) axis we need to have a scatterer at $r = 0$ then the r_1 axis represents the impulse response, similarly for the other axis. Thus if a scatterer exists at $r = 0$ then the bispectrum at the r axis represents the impulse response.

An expression for the third moment sequence of complex data can be obtained from the direct method as follows;

$$R(m, n) = E\{\hat{S}^*(f)\hat{S}(f+m)\hat{S}(f+n)\} \quad (4.9)$$

where

$$R(m, n) = R(n, m) \quad (4.10)$$

Thus the only symmetry property for the bispectrum in this case is

$$B_{S_t}(R_1, R_2) = B_{S_t}(R_2, R_1) \quad (4.11)$$

Moreover, for complex data we can use more than one form of bispectrum as suggested by Brillinger and Rosenblatt [12] and that is by placing the conjugate at different combinations of $\tilde{S}(f)$. However, the above definition is most appropriate for interpretation purposes. Also, the real part of the radar data could be used only to compute the bispectrum with little loss of information.

4.3 Classical Bispectrum Estimation Algorithms

Classical methods for bispectral estimation were used in this study. High resolution technique that involve ARMA modeling algorithms may be used also to obtain bispectral estimates. Classical bispectral estimators, often called conventional estimators are divided into two categories. Indirect methods that follow the definition of the bispectrum as the two dimensional Fourier transform of the third order moment sequence, and Direct methods similar to the periodogram estimate of the spectral density.

4.3.1 Indirect Method

Let $\{X(1), X(2), \dots, X(N)\}$ be the frequency data set. Then the estimate of the third moment sequence is

$$\hat{R}(m, n) = \frac{1}{N} \sum_{i=s_1}^{s_2} X(i)X(i+m)X(i+n) \quad (4.12)$$

where $s_1 = \max(0, -m, -n)$ and $s_2 = \min(N-1, N-1-m, N-1-n)$. Then the estimate of the bispectrum $\hat{B}(R_1, R_2)$ as a function of range R is generated as:

$$\hat{B}(r_1, r_2) = \sum_{m=-L}^L \sum_{n=-L}^L \hat{R}(m, n)W(m, n) \exp(-j4\pi/c(r_1m + r_2n)) \quad (4.13)$$

where $L < N-1$ and $W(m, n)$ is a two dimensional window function. The optimum window is used in this study and it can be generated from a one dimensional window as:

$$W(m, n) = d(m)d(n)d(n-m) \quad (4.14)$$

$$\begin{aligned} d(m) &= \frac{1}{\pi} \left| \sin \frac{\pi m}{L} \right| + \left(1 - \frac{|m|}{L} \right) \left(\cos \frac{\pi m}{L} \right), \quad |m| \leq L \\ &= 0, \quad |m| > L \end{aligned} \quad (4.15)$$

The frequency and time domain responses of the two dimensional window are shown in Figures 4.1-4.2. Notice that the optimum window has a wide main lobe and low sidelobes.

4.3.2 Direct Method

Compute the impulse response $Y(r)$:

$$Y(r) = \frac{1}{N} \sum_{k=0}^{N-1} X(k) \exp(-j4\pi kr/cN) \quad (4.16)$$

A Hanning window $d(m)$ may be applied to the frequency samples

$$d(m) = \frac{1}{2} \left(1 + \cos \left(\frac{2\pi(m - (N-1)/2)}{N-1} \right) \right) \quad (4.17)$$

then the bispectrum can be computed over the triangle $0 \leq r_1 \leq r_2$, $r_1 + r_2 \leq f_s/2$ where f_s is the sampling frequency.

$$B(r_1, r_2) = K y(r_1) y(r_2) y^*(r_1 + r_2) \quad (4.18)$$

where K is constant and depends on the spacing between frequency samples ($K = (\frac{N}{f_s})^2$), f_s is the sampling frequency of the data.

For sufficiently large number of data points, both methods provide unbiased estimates. In general classical methods have high variance and the estimates obtained are not usually smooth. The advantage of using classical techniques is the fact that fast computations algorithms such as the FFT are available.

4.4 Blade-Sphere Example

Consider a blade of width $r_1 - r_0$ and a sphere at a distance $r_2 - r_1$ from the trailing edge of the blade. The zero reference is set at a distance r_0 from the leading edge of the blade (see Figure 4.3). It can be shown that if one considers four ray paths the backscattered signal is;

$$\begin{aligned} \tilde{S}_t(f_j) = & A_1 + A_2 \exp(-j2\pi r_1 \frac{f_j}{c}) \\ & + A_3 \exp(-j2\pi r_2 \frac{f_j}{c}) \\ & + A_4 \exp(-j2\pi(r_1 + r_2 - r_0) \frac{f_j}{c}) \end{aligned} \quad (4.19)$$

assuming that the amplitudes A_1, A_2, A_3 , and A_4 are frequency independent. The corresponding amplitude and phase of this structure are shown in Figure 4.4. The impulse response of the blade and sphere target as computed using the inverse Fourier transform (with a Hanning window over a frequency band from 1.5 GHz to 12 GHz) is shown in Figure 4.5. Note the one to one relationship for the first three responses with the geometry of the target. The fourth response, however, is an interaction term and there is no single discrete target component which corresponds to it.

Figure 4.6 shows the bispectral response of the backscatter from the blade-sphere combination without using a window. The bispectral response of the windowed third moment sequence is shown in Figure 4.7. In these figures, $r_0 = 0$ (zero reference at

leading edge of the blade). Note the response at ($r_1 = 1.6\text{meters}$, $r_2 = 2.4\text{meters}$) which is due to interaction between the trailing edge of the blade and the sphere and is represented by the term $\exp(-j2\pi(r_1 + r_2 - r_0)\frac{f}{c})$. We can also notice the twelve symmetry regions of the bispectrum.

If the value of r_0 is increased to 1 meter, the bispectral response shown in Figure 4.8 results. Note that all of the response terms have moved along the associated diagonals, but the particular scattering and interaction terms are still observable. A three dimensional display of the bispectral response is shown in Figure 4.9.

4.5 Bispectral Response of Noisy Data

If zero mean white Gaussian noise is added to the raw data, the resulting impulse response and bispectral response are shown in Figures 4.10 and 4.11 respectively. Note that the detectability of the target scattering terms is greatly reduced in the impulse response, and noise components in the time domain can be misinterpreted as discrete scatterers. This problem is less effective in the bispectrum case where discrete scatterers and interaction terms can still be identified under the same noise conditions used in the impulse response. This is due to the fact that in the bispectrum case the noise components at different frequencies are uncorrelated.

4.5.1 Mean Square Error

Consider the measured observation $y(f)$ at frequency f . Assume that the noisy data is $y(f) = x(f) + n_f$ where n_f is a Gaussian distributed random variable. Also, assume that the data are wide sense stationary. The frequency bandwidth is $f_h - f_l$ where $f_l \geq 0$ Hz.

The third order autocorrelation function of the measured noisy data is;

$$R_y(f_1, f_2) = E\{y(f)y(f + f_1)y(f + f_2)\} \quad (4.20)$$

then

$$\begin{aligned} R_y(f_1, f_2) &= E\{x(f)x(f + f_1)x(f + f_2) \\ &\quad + x(f)n_{f+f_1}n_{f+f_2} + x(f + f_1)n_f n_{f+f_2} \end{aligned}$$

$$\begin{aligned}
& + x(f+f_2)n_f n_{f+f_1} + x(f)x(f+f_1)n_{f+f_2} \\
& + x(f)x(f+f_2)n_{f+f_1} + x(f+f_1)x(f+f_2)n_f \\
& + n_f n_{f+f_1} n_{f+f_2}
\end{aligned} \tag{4.21}$$

therefore

$$R_y(f_1, f_2) = R_x(f_1, f_2) + \bar{x}\{R_n(f_1) + R_n(f_2) + R_n(f_1 - f_2)\} + \beta R_n(f_1, f_2) \tag{4.22}$$

However, for a Gaussian noise $\beta = 0$ then

$$R_y(f_1, f_2) = R_x(f_1, f_2) + \sigma^2 \bar{x}\{\delta(f_1) + \delta(f_2) + \delta(f_1 - f_2)\} \tag{4.23}$$

where σ^2 is the noise power.

The second order autocorrelation is given as

$$\begin{aligned}
R_y(F) &= E\{y(f)y(f+F)\} \\
&= E\{(x(f) + n_f)(x(f+F) + n_{f+F})\} \\
&= R_x(F) + R_n(F) \\
&= R_x(F) + \sigma^2 \delta(F)
\end{aligned} \tag{4.24}$$

Consider the following as an error measure for estimating the impulse response for noisy targets;

$$E_I = E\left\{\int_t |h_x(t) - h_y(t)|^2 dt\right\} \tag{4.25}$$

where $h_y(t)$ and $h_x(t)$ represent the impulse response for noisy and noiseless data respectively and $E\{.\}$ stands for the expected value. Then E_I can be written as ;

$$E_I = E\left\{\int_f |H_x(f) - H_y(f)|^2 df\right\} \tag{4.26}$$

using Parseval's theorem. then E_I is equal to;

$$\begin{aligned}
E_I &= E\left\{\int_{f_l}^{f_h} |n(f)|^2 df\right\} \\
E_I &= 2\sigma^2(f_h - f_l)
\end{aligned} \tag{4.27}$$

If the spectral density is computed then the error measure is;

$$\begin{aligned}
 E_S &= \int_t |S_x(t) - S_y(t)|^2 dt \\
 &= \int_f |R_x(f) - R_y(f)|^2 df \\
 &= \int_f |\sigma^2 \delta(f)|^2 df \\
 &= 0
 \end{aligned}$$

Notice that in this case the mean-square error is not dependent on the bandwidth.

Consider the following as an error measure for bispectrum of noisy signals;

$$E_B = \sqrt{\int_{t_1} \int_{t_2} |B_x(t_1, t_2) - B_y(t_1, t_2)|^2 dt_1 dt_2} \quad (4.28)$$

where $B_x(t_1, t_2)$, $B_y(t_1, t_2)$ are the bispectrum for ideal noiseless data and noisy data respectively. Then using Parseval's theorem in two dimensions E_B can be written as;

$$E_B = \sqrt{\int_{f_1} \int_{f_2} |R_x(f_1, f_2) - R_y(f_1, f_2)|^2 df_1 df_2} \quad (4.29)$$

Then using equation (4)

$$E_B = \sigma^2 \bar{x} \sqrt{\int_{f_1} \int_{f_2} |\delta(f_1) + \delta(f_2) + \delta(f_1 - f_2)|^2 df_1 df_2} \quad (4.30)$$

$$= 2\sigma^2 \bar{x} \sqrt{(2 + \sqrt{2})(f_h - f_l)} \quad (4.31)$$

Therefore :

$$E_B = E_I \bar{x} \sqrt{\frac{2 + \sqrt{2}}{f_h - f_l}} \quad (4.32)$$

Therefore the mean square error is directly dependent on the frequency bandwidth in the impulse response case as well as the bispectral response. However, in the bispectrum case a new factor is included that depends on the signal itself.

4.6 Bispectral Response For Dispersive Scatterers

The effect of dispersion in the data is shown in Figures 4.12 and 4.13. Dispersion is the result of scattering from a subcomponent of the radar target where the scatterer behavior varies as a function of frequency. In this case, the behavior is modeled as follows.

$$A_i(f_j) = A_i(1 + \alpha \exp(-k f_j) \cos(\beta f_j)) \quad (4.33)$$

where

$A_i(f_j)$ = is the frequency dependent amplitude of the backscatter coefficient from the i^{th} scatterer. and

α , k , and β are constants.

In this study, $\alpha = 0.6$ and $k = 0.01$, and $\beta = 20\pi$.

These figures show that the effect of dispersion is not critical to the bispectrum response.

4.6.1 Single Edge Dispersion

The above form of dispersion effects the amplitude of the response only. In general dispersion effects the amplitude and the phase of the radar back-scatter. This type of dispersion results in energy loss along the physical target thus effectively moving the scattering centers in the down range profile.

In this section we study the case where only one edge is dispersive in amplitude and phase. This is rather a realistic model and matches to a certain extent scattering from a rocket where the front end scatterer (the nose) is highly dispersive. In this case the amplitude of the returned signal can be modeled as:

$$A_i(f_j) = A_i\{(1 + \alpha \exp(-k f_j) \cos(\beta f_j))\} \exp(j\rho/f) \quad (4.34)$$

where ρ depends on the scatterer. This model indicates that scattering takes place near the point of the nose for high frequency components and further away from that point at low frequencies. Figures 4.14-4.15 show the impulse response and the

bispectral response of this type of scattering. As expected the scatterers location will be displaced and the response will be smeared. The bispectral response shows a similar type of behavior except that the energy loss phenomenon and the frequency dependent scattering is recognizable. Notice that the interaction term response indicates that scattering takes place somewhere between the nose and the second scatterer.

4.7 Bispectral Responses for Canonical Aircraft

Experimental data for scattering from a 6 Inches canonical aircraft for frequencies between 1 – 18 GHz were used in determining the bispectral responses from various components of the aircraft. Back-scattering from wing only, fuselage, fuselage and stabilizer, and complete aircraft parts were measured at the Ohio State ElectroScience laboratory [13].

Figures 4.16-4.19 show the bispectral response for such models corresponding to different parts of the aircraft. In the case where the scattering from the fuselage only is measured no considerable interaction term is observed. The addition of the stabilizer introduces some interactions. In the case where only the wing is present, it is shown that many high order scattering mechanisms take place along the wing area. The bispectral response for the complete aircraft is dominated by the interactions that take place in the wing area. These figures will help us understand bispectral responses from real targets where many complicated scattering mechanisms are involved.

4.8 Bispectral Responses for Commercial Aircraft

The compact radar cross section measurement range at the Ohio State University ElectroScience Laboratory[13] was used to make measurements of the radar scattering of a set of 5 scale models of commercial transport aircraft (see Figure 4.20). The measurements were calibrated so that absolute values of amplitude (in square centimeters) and phase (in degrees from an absolute reference plane) were available over the band of frequencies from 1.5 to 12.0 GHz. This corresponds to frequencies in the HF band for full scale aircraft and means that the targets are in

the resonance region of the radar (ie: The wavelength is on the order of the target size)[13].

Using the techniques described above (including the use of the optimum window function), the bispectrum of each radar target signature was computed. The results are shown in Figures 4.21 to 4.25. Note that the different radar targets yield distinctly different bispectral responses. It can be shown that this implies that such responses are likely candidates as features for radar target identification.

Since each radar target is being measured in the resonance region (as mentioned above), it can be shown that the target signature is relatively insensitive to changes in aspect angle. (especially the impulse response signature.) The result of taking the bispectral response for the Boeing 707 as the aspect angle varies from 10 to 30 degrees is shown in Figures 4.26-4.28. It can be seen that the bispectral response is rather stable between each 10 degree angle change. Figure 4.29 shows the bispectral response of a 747 at 0 degrees azimuth and -5 dB signal to noise ratio (SNR). In the next section bispectral images (as such) are used in classifying different targets.

4.9 Classification Methods

In this section we describe how to classify radar targets based on their bispectral response using two dimensional cross-correlation. The concept of the "catalog" of data will be used with a bispectral feature space. In this technique a catalogue of noise free bispectral responses are used to determine the identity of a target from which a noisy bispectrum is available. It is known (in this study) that the target corresponds to one of the entries in the catalogue. First, the goal to find a catalogue bispectral response that most closely matches the bispectral response $B_j(r_1, r_2)$ of an unknown target. That is to minimize

$$\min_i \left\{ \int_{r_1} \int_{r_2} (B_i(r_1, r_2) - B_j(r_1, r_2))^2 dr_1 dr_2 \right\} = \quad (4.35)$$

$$\min_i \left\{ \int \int B_i^2(r_1, r_2) dr_1 dr_2 + \int \int B_j^2(r_1, r_2) dr_1 dr_2 \right. \quad (4.36)$$

$$\left. - \int \int B_i(r_1, r_2) B_j(r_1, r_2) dr_1 dr_2 \right\} \quad (4.37)$$

where $B_i(r_1, r_2)$ and $B_j(r_1, r_2)$ are the bispectral responses of catalogue target i and unknown target j . This requires maximizing

$$\int_{r_1} \int_{r_2} B_i(r_1, r_2) B_j(r_1, r_2) dr_1 dr_2 \quad (4.38)$$

and this can be done by shifting $B_j(r_1, r_2)$ over all the domain of $B_i(r_1, r_2)$. This is equivalent to maximizing

$$\rho_{ij}(R_1, R_2) = \frac{\int_{r_1} \int_{r_2} B_i(r_1, r_2) B_j(r_1 + R_1, r_2 + R_2) dr_1 dr_2}{\left[\int_{r_1} \int_{r_2} |B_j(r_1 + R_1, r_2 + R_2)|^2 dr_1 dr_2 \right]^{\frac{1}{2}} \left[\int_{r_1} \int_{r_2} |B_i(r_1, r_2)|^2 dr_1 dr_2 \right]^{\frac{1}{2}}} \quad (4.39)$$

where $\rho_{ij}(R_1, R_2)$ is the normalized cross correlation coefficient of catalogue target bispectral response $i = 1, 2, \dots, 5$ and test target response j . Notice that the factor in the denominator depends on R_1, R_2 and this is in order to compute a normalized crosscorrelation.

4.9.1 Indirect method

Using Fourier transform identities and Parsevals theorem the cross correlation can be written as

$$\rho_{ij}(R_1, R_2) = \frac{I2FT\{R_i(f_1, f_2) R_j^*(f_1, f_2)\}}{\left[\int_{f_1} \int_{f_2} |R_i(f_1, f_2)|^2 df_1 df_2 \right]^{\frac{1}{2}} \left[\int_{f_1} \int_{f_2} |R_j(f_1, f_2)|^2 df_1 df_2 \right]^{\frac{1}{2}}} \quad (4.40)$$

where $I2FT$ stands for the inverse two dimensional Fourier transform and $R_j^*(f_1, f_2)$ is the conjugate of $R_j(f_1, f_2)$. For the discrete frequency case the cross correlation is

$$\rho_{ij}(R_1, R_2) = \frac{I2FFT\{R_i(f_1, f_2) R_j^*(f_1, f_2)\}}{\left[\sum_{f_1} \sum_{f_2} |R_i(f_1, f_2)|^2 \right]^{\frac{1}{2}} \left[\sum_{f_1} \sum_{f_2} |R_j(f_1, f_2)|^2 \right]^{\frac{1}{2}}} \quad (4.41)$$

where $I2FFT$ is the inverse two dimensional fast Fourier transform. The test target is classified to a catalogue class c if

$$\rho_{cj}(R_1, R_2) = \max_i \{ \max_{R_1, R_2} \rho_{ij}(R_1, R_2) \} \quad i = 1, \dots, 5. \quad (4.42)$$

4.9.2 Direct method

If the direct method for estimating the birange profile for radar targets was used then the classification would follow as

- Compute the birange estimate of both catalogue target i and test target j as

$$B_i(r_1, r_2) = \beta y_i(r_1) y_i(r_2) y_i(r_1 + r_2) \quad (4.43)$$

over the triangle $\Delta : r_1 < r_2, r_1 + r_2 < c\pi$, and $r_2 > 0$. where β is a constant and $y(r)$ is the impulse response,

$$y_i(r) = \frac{1}{N} \sum_{n=0}^{N-1} X_i(n) \exp(j2\pi nr/N) \quad (4.44)$$

and $X(n)$ is the measured frequency data for target i .

- Compute the crosscorrelation $\rho_{ij}(R_1, R_2)$ as

$$\rho_{ij}(R_1, R_2) = \frac{\sum_{r_1} \sum_{r_2} B_i(r_1, r_2) B_j(r_1 + R_1, r_2 + R_2)}{[\sum_{r_1} \sum_{r_2} |B_i(r_1, r_2)|^2]^{\frac{1}{2}} [\sum_{r_1} \sum_{r_2} |B_j(r_1 + R_1, r_2 + R_2)|^2]^{\frac{1}{2}}} \quad (4.45)$$

where $R_1, R_2 \in \Delta$.

- The decision rule is;

$$\rho_{cj}(R_1, R_2) = \max_i \{ \max_{R_1, R_2} \rho_{ij}(R_1, R_2) \} \quad i = 1, \dots, 5. \quad (4.46)$$

4.9.3 Comparison

The first method does not require bispectrum estimation but still requires estimates of third order autocorrelation, while the second method requires computation of two dimensional crosscorrelation but no third order autocorrelation. Also, the first method involves a two dimensional window, while second method involves a bispectral estimate of Hanning window. Another important difference is that the first method requires computation of third order autocorrelation over all birange domain while second method makes use of the triangular symmetry. Moreover,

the first method requires third order correlation over all R_1, R_2 , two dimensional Fourier transform. The, second method requires one dimensional Fourier transform, birange estimate over a triangle Δ , and crosscorrelation estimate of biranges over Δ .

In order to compute a normalized cross correlation coefficient we need to compute the normalizing factor $\forall R_1, R_2 \in \Delta$. This is a major disadvantage for the second method. Also, the decision criteria for the first method is over all R_1, R_2 while the other method is over one triangle(1/8) of R_1, R_2 domain.

4.9.4 Classification Algorithm

It has been shown that both classical methods in bispectrum estimation require many computations if used for radar target identification. An algorithm that combines both approaches can be implemented as follows;

- 1) Compute the Impulse response of the test target j using discrete Fourier transform which can be implemented as Fast Fourier transform.

$$x_j(r) = \frac{1}{N} \sum_{f=0}^{N-1} X_j(f) \exp j4\pi fr/c \text{ --- FFT} \quad (4.47)$$

- 2) Compute the third order autocorrelation estimate

$$R_j(f_1, f_2) = \frac{1}{N^2} \sum_{r_1} \sum_{r_2} x_j(r_1) x_j(r_2) x_j(r_1 + r_2) \exp j4\pi(f_1 r_1 + f_2 r_2)/c \text{ --- 2FFT} \quad (4.48)$$

- 3) Compute the cross correlation coefficient as

$$\rho_{ij}(R_1, R_2) = \frac{I2FFT\{R_i(f_1, f_2) R_j^*(f_1, f_2)\}}{\left[\sum_{f_1} \sum_{f_2} |R_i(f_1, f_2)|^2\right]^{\frac{1}{2}} \left[\sum_{f_1} \sum_{f_2} |R_j(f_1, f_2)|^2\right]^{\frac{1}{2}}} \text{ --- 2FFT} \quad (4.49)$$

- 4) The test target is classified to a catalogue class c if

$$\rho_{cj}(R_1, R_2) = \max_i \left\{ \max_{R_1, R_2} \rho_{ij}(R_1, R_2) \right\} \quad i = 1, \dots, 5. \quad (4.50)$$

In the above algorithm one one-dimensional FFT and two two-dimensional FFT are needed in order to compute the normalized cross correlation coefficient. Thus, the above algorithm is most suitable for classification of large arrays of data in the

frequency domain where the computation time saved due to the parallel computation feature of the above algorithm becomes considerably large.

4.10 Radar Target Identification Example

A Monte Carlo simulation based on the *Indirect Method* was performed to evaluate the performance of the concepts discussed in this chapter where the bispectral response was used as a feature for characterizing radar targets. The data base used in this example has been used before in radar target identification studies [14,15,16]. The data base consists mainly of experimental measurements in the frequency band from 1 – 12 GHz of scale models of commercial transport aircraft. A photo with corresponding names of these aircraft are shown in Figure 4.20. Moreover, the scale data corresponds to measurements of the radar cross section (RCS) of full scale aircraft in the HF/VHF frequency band.

The classification algorithm is shown in Figure 4.30. In this algorithm Gaussian distributed noise was added to the raw data (complex radar cross section measurements RCS versus frequency). An estimate of the bispectral response of the resulting noisy data is then computed using the indirect method. A two dimensional cross-correlation was performed between the noisy bispectral response and the catalogue ideal bispectral response. A decision is made in favor of the catalogue with the largest cross correlation. The same procedure is repeated for different test targets. Figure 4.31 shows the actual algorithm used to evaluate the classification performance technique shown in Figure 4.30. In this algorithm the third moment sequence of both noise free catalog data noisy data (additive noise) are computed. The normalized inverse two dimensional fast Fourier transform of the product of the two third order moment sequences is then computed. Decision is made in favor of the class with the largest cross correlation with the unknown noisy target. Decision statistics for each target are computed at each noise level and total statistics of classification error are computed for all targets at a certain noise level. One hundred experiments were performed for each test target (total of 500 experiments). The entire test is repeated for different noise levels. Finally the percentage of misclassification is plotted versus signal to noise ratio.

Figure 4.32 shows the classification performance for five commercial aircraft where complete azimuth information is assumed to be known. This performance curve shows that bispectral estimates can be used effectively in radar target identification. Notice that the percentage of misclassification is zero for a signal to noise ratio higher than 0 dB.

The above example shows that reliable target identification can be achieved using the bispectral response as a feature source. The classification performance can be further improved by developing a feature selection algorithm that can be applied to the bispectral responses of both catalogue and unknown test targets. Furthermore, the classification approach used in this example is a non-parametric technique that requires no a priori information about the parametric distribution of the measured radar data.

4.11 Conclusions

In this chapter the application of bispectrum estimation to radar signature analysis is investigated. It has been demonstrated that a bispectral response of radar backscatter signals has the advantage of identifying multiple interactions for complex radar targets. This leads to the conclusion that higher order interactions of radar backscatter may be identified using higher order spectral analysis. Such high order interactions that are relatively smaller in the impulse response because of their amplitudes may be recovered using high orders of spectral analysis. Therefore, the bispectrum and other high order spectral analysis methods may be considered as potential radar feature extraction techniques that may be effectively used jointly with the impulse response in radar target identification. It is shown that bispectral responses of radar backscatter signals are relatively robust under conditions of high noise and frequency dispersion. Finally, it has been shown that radar targets can be successfully identified at zero dB signal to noise ratio using a simple classification algorithm such as cross correlation.

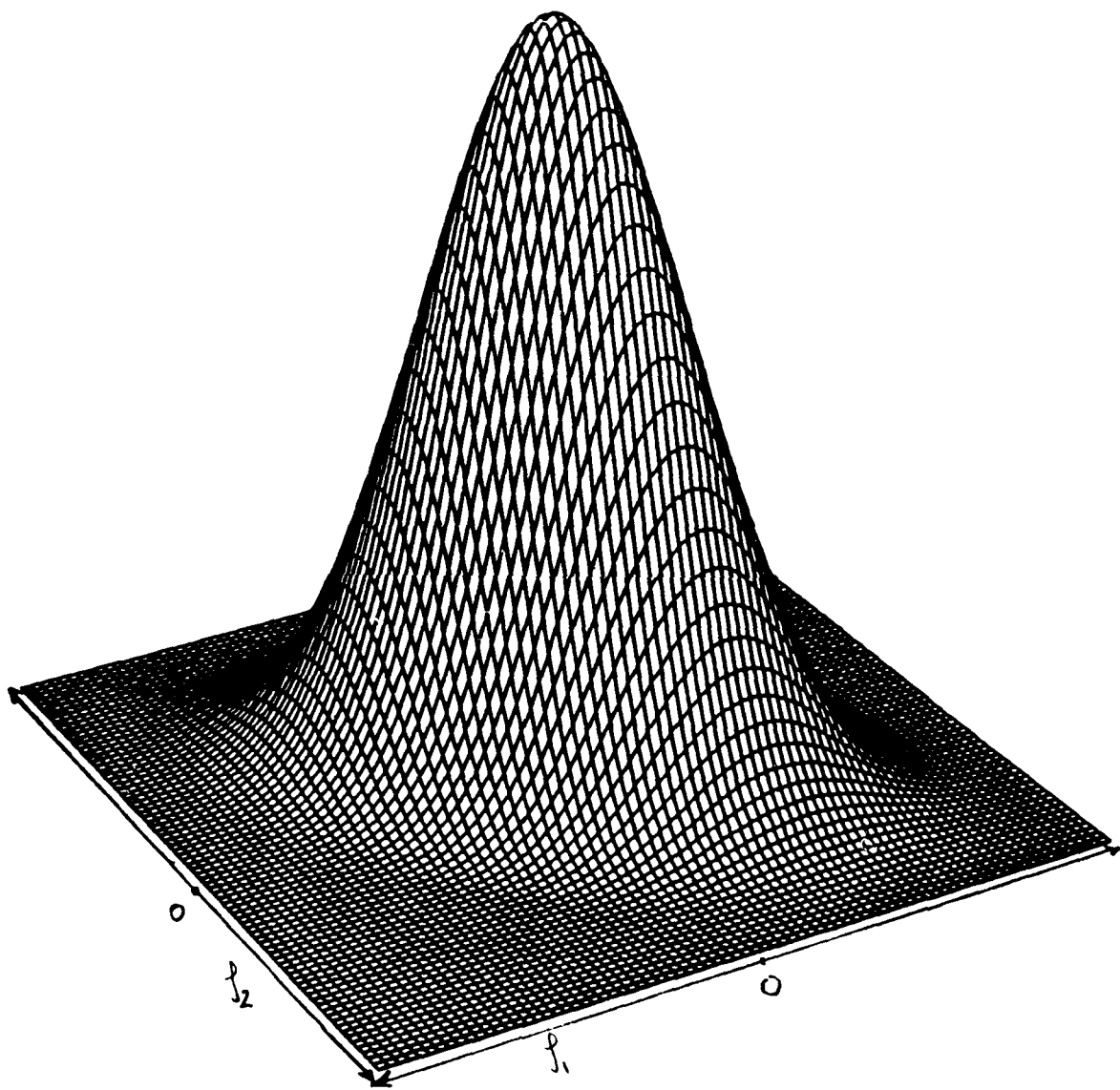


Figure 4.1: Optimum window (minimum bias supremum) in frequency domain.

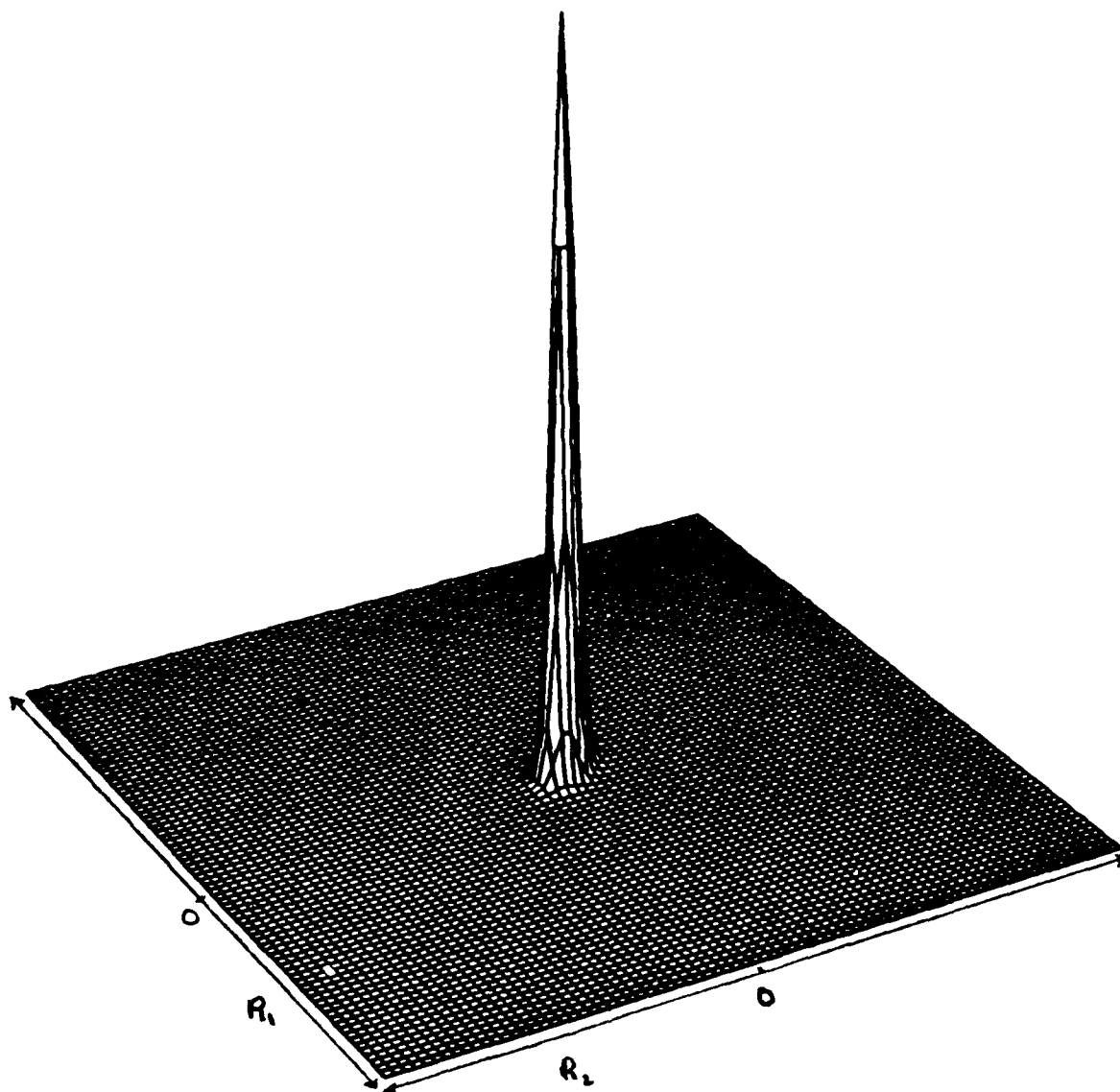
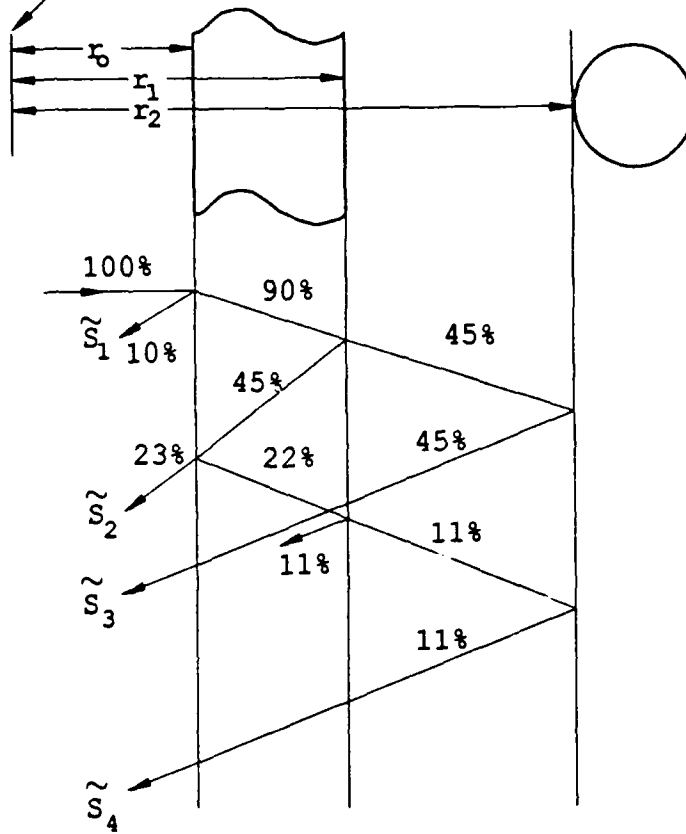


Figure 4.2: Optimum window (minimum bias supremum) in range domain.

ZERO REFERENCE



$$\begin{aligned}\tilde{S}_1 &= A_1 e^{-jk2r_0} & A_1 &= 10 \\ \tilde{S}_2 &= A_2 e^{-jk2r_1} & A_2 &= 23 \\ \tilde{S}_3 &= A_3 e^{-jk2r_2} & A_3 &= 45 \\ \tilde{S}_4 &= A_4 e^{-jk[2(r_2 + (r_1 - r_0))]} & A_4 &= 11 \\ \tilde{S}_T &= \tilde{S}_1 + \tilde{S}_2 + \tilde{S}_3 + \tilde{S}_4\end{aligned}$$

Figure 4.3: Internal bounce diagram for blade-sphere interaction.

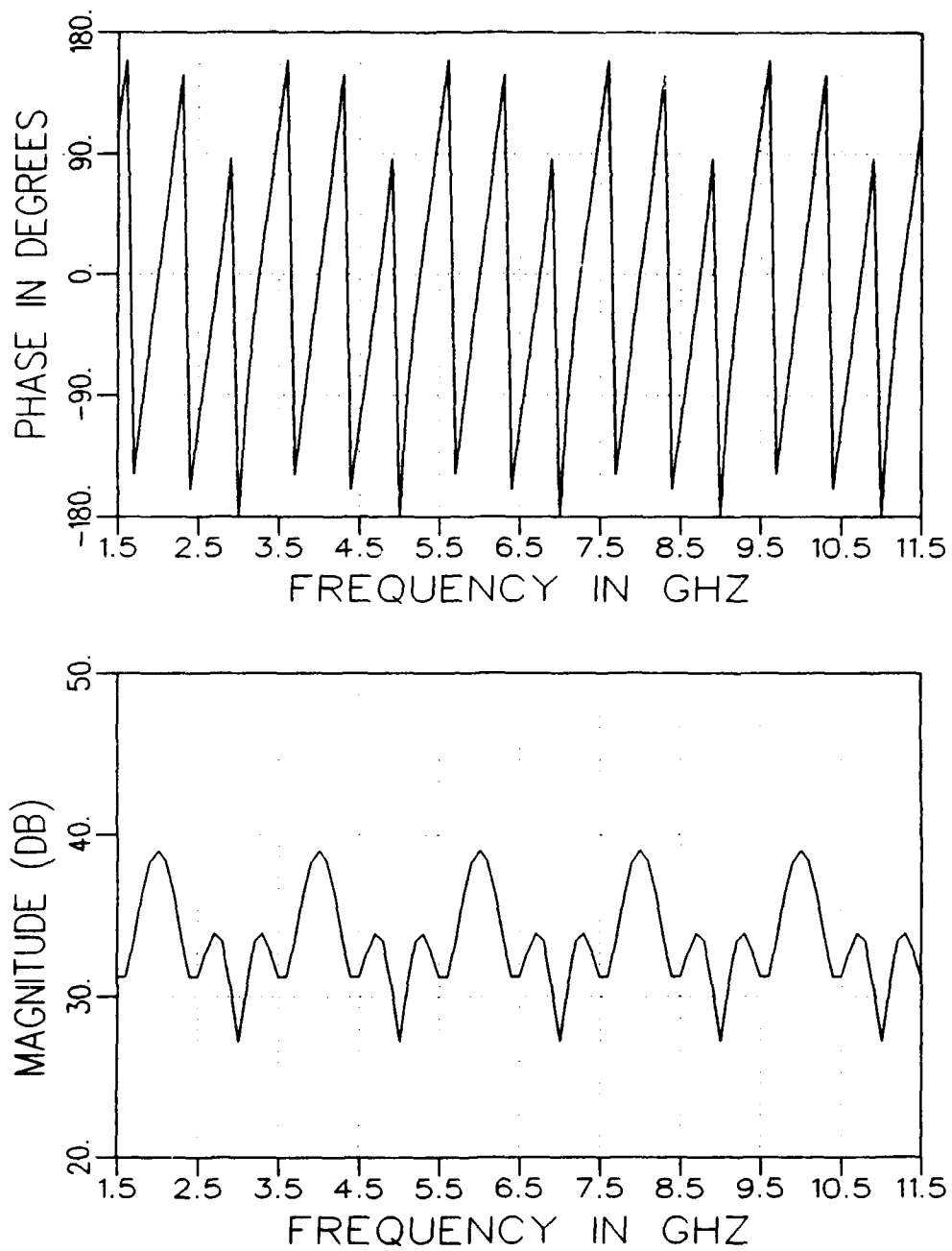


Figure 4.4: Frequency response for blade-sphere target.

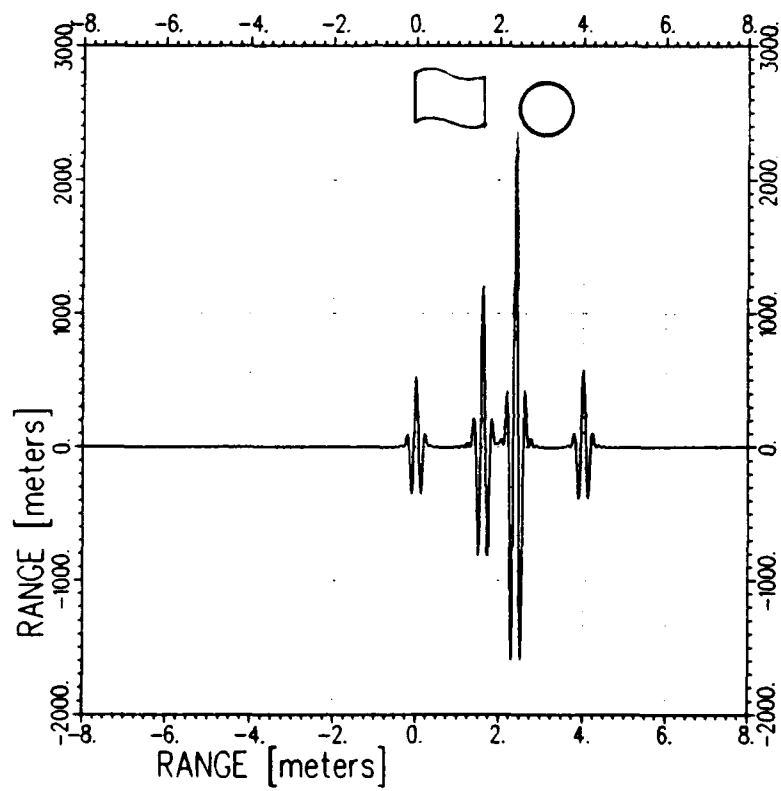


Figure 4.5: Impulse response for blade-sphere, $r_0 = 0$, $r_1 = 1.6$ m, $r_2 = 2.4$ m.

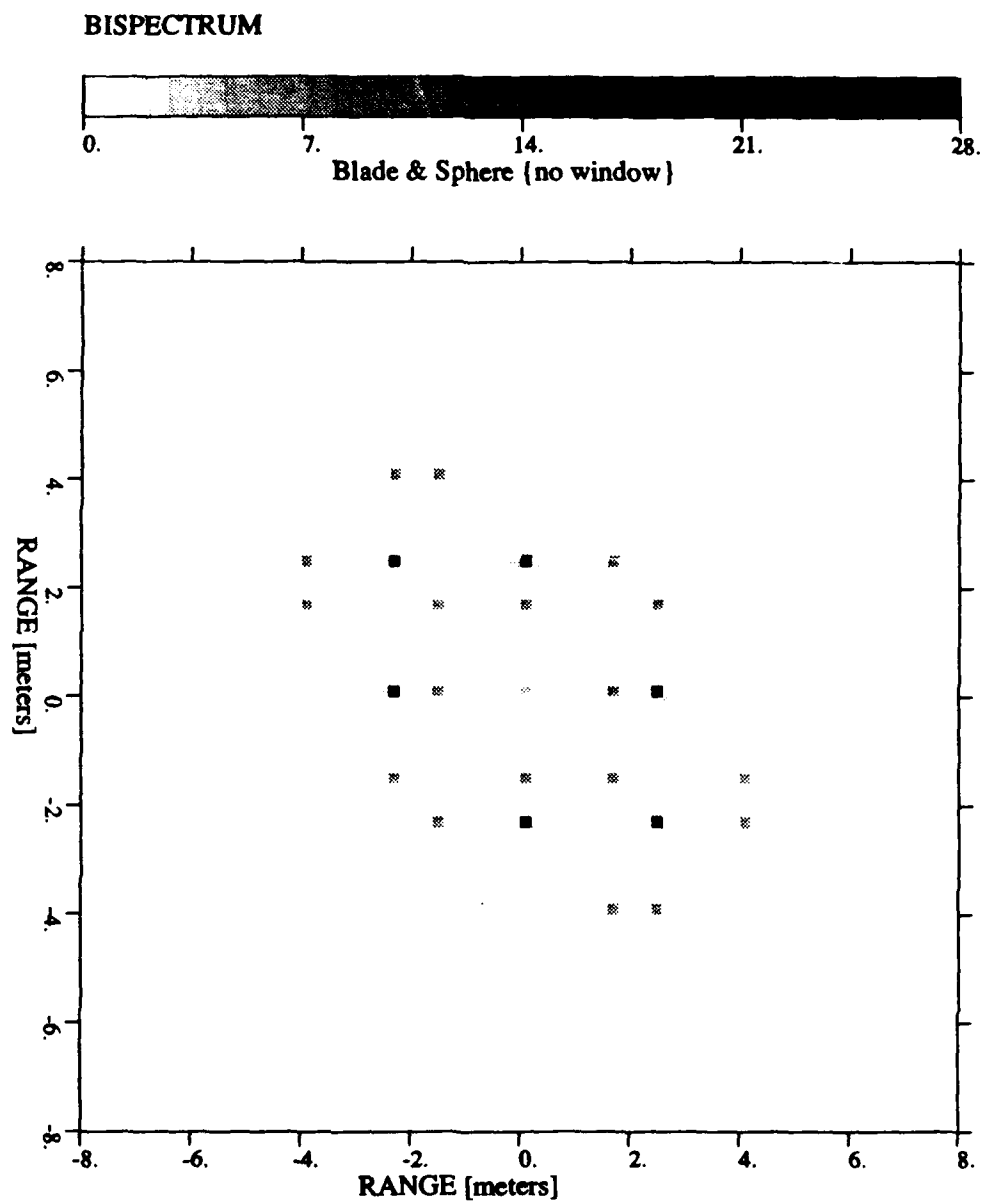


Figure 4.6: Bispectrum for blade-sphere without window.

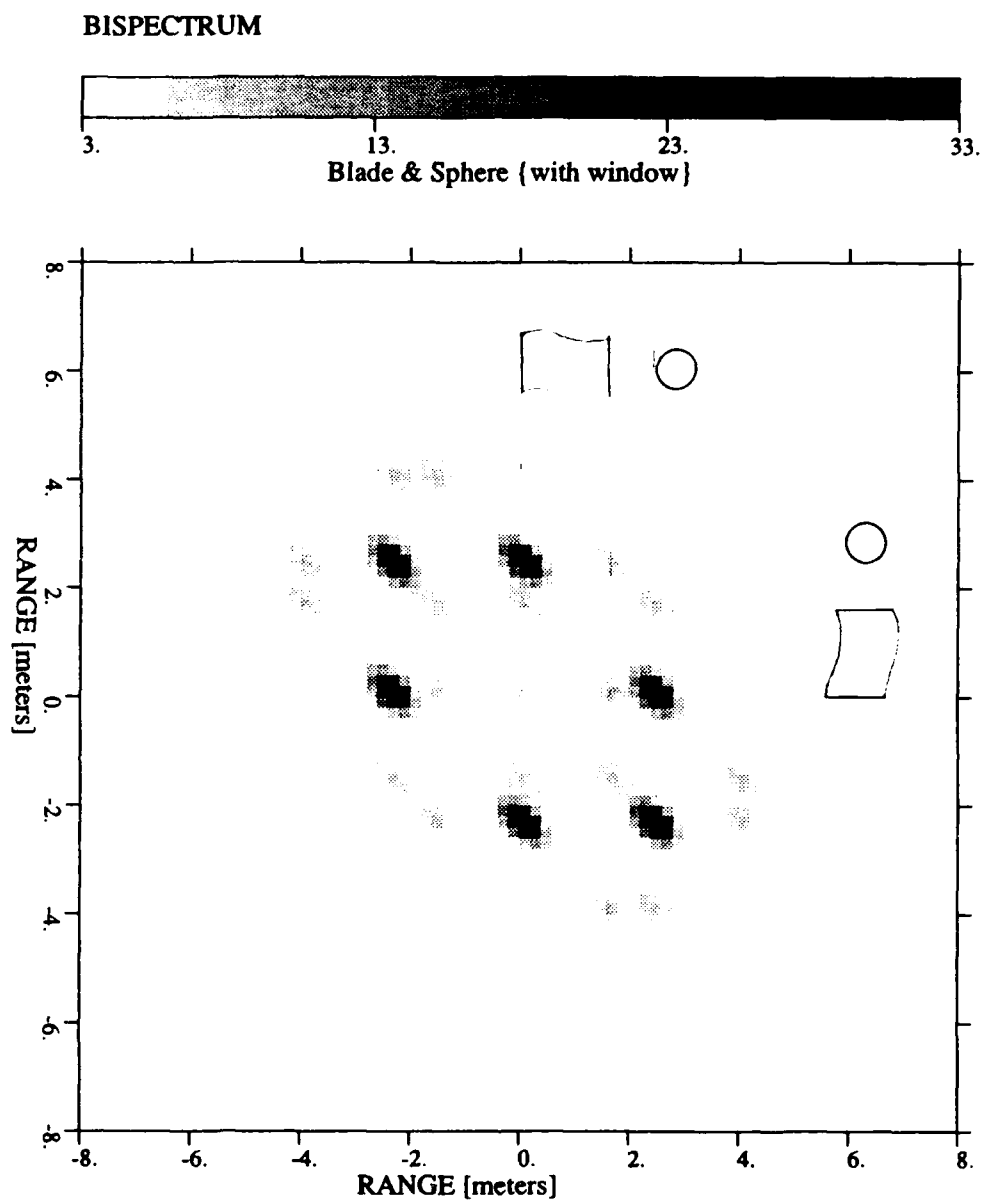


Figure 4.7: Bispectrum for blade-sphere $r_1 = 1.6$ m, $r_2 = 2.4$ m. with window

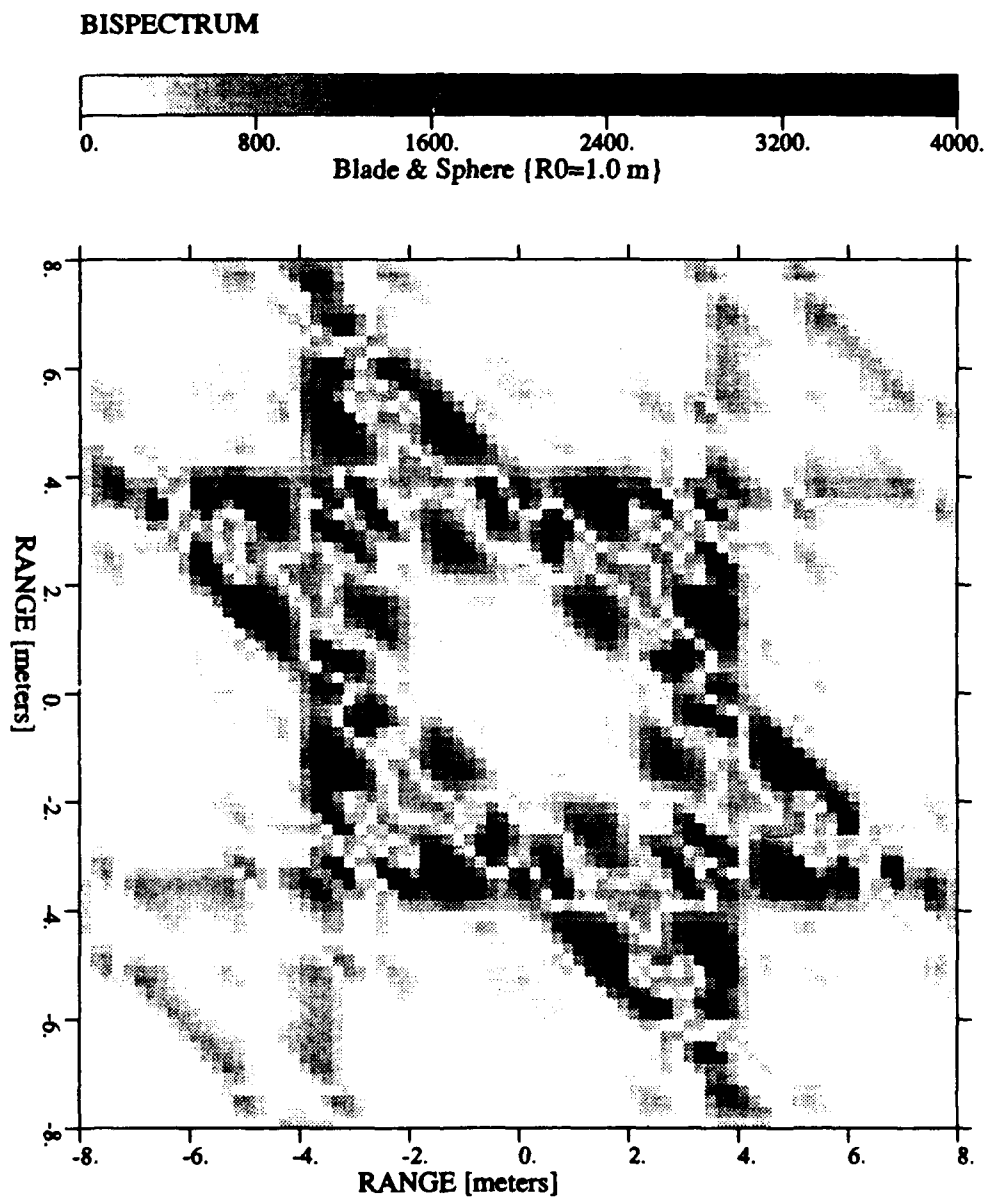


Figure 4.8: Bispectrum for blade-sphere with $r_0 = 1$ m.

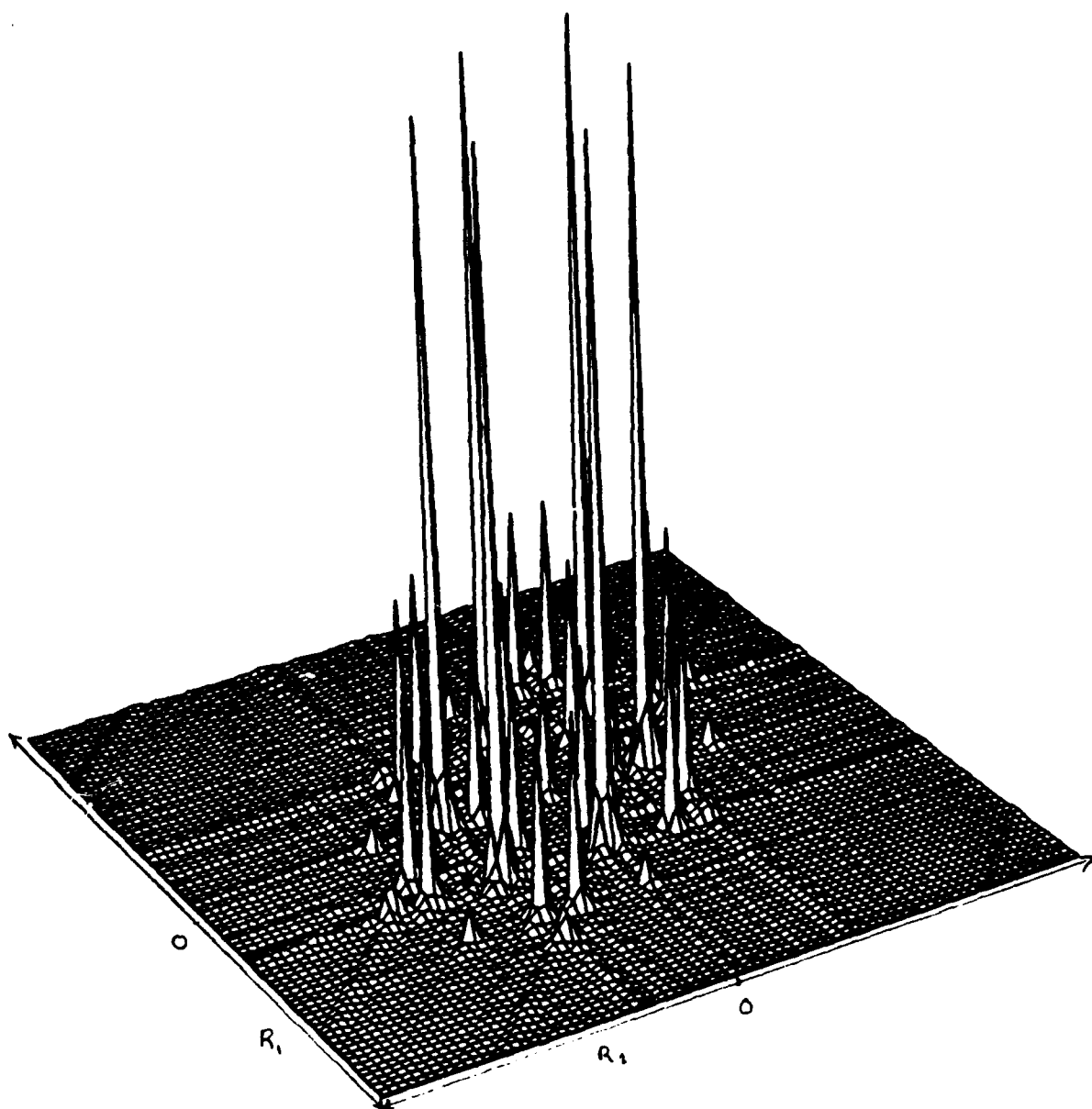


Figure 4.9: 3-D bispectral response for blade-sphere combination

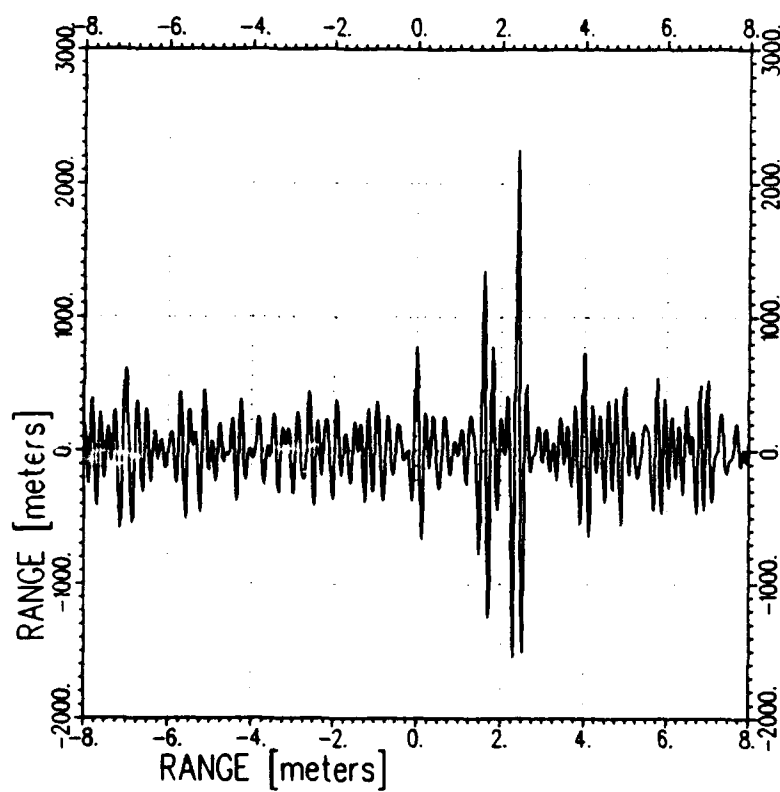


Figure 4.10: Impulse response for noisy backscatter from blade-sphere (SNR= -30 dB)

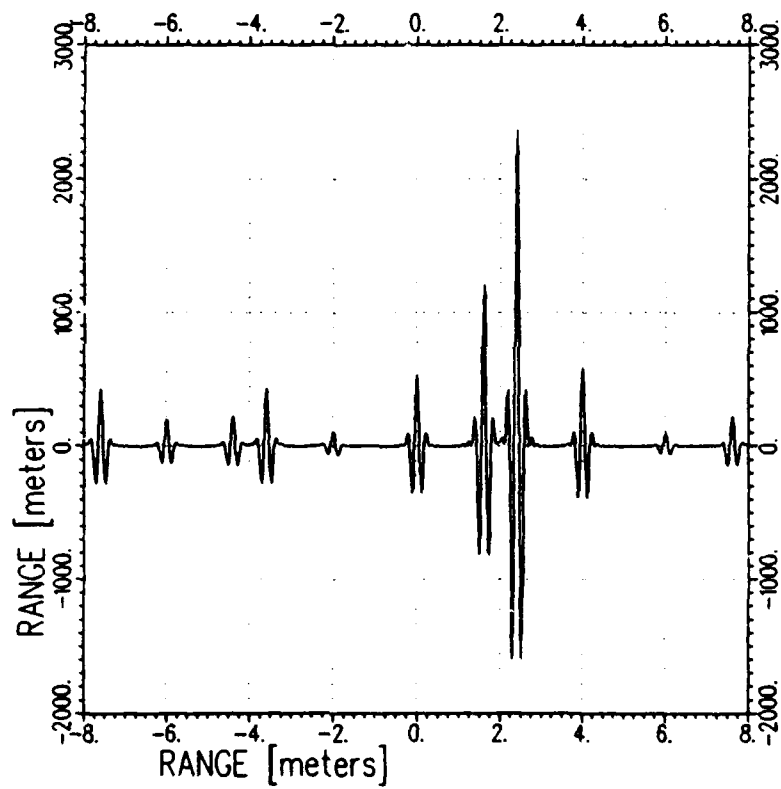


Figure 4.12: Impulse response of frequency dispersive backscatter for blade-sphere.

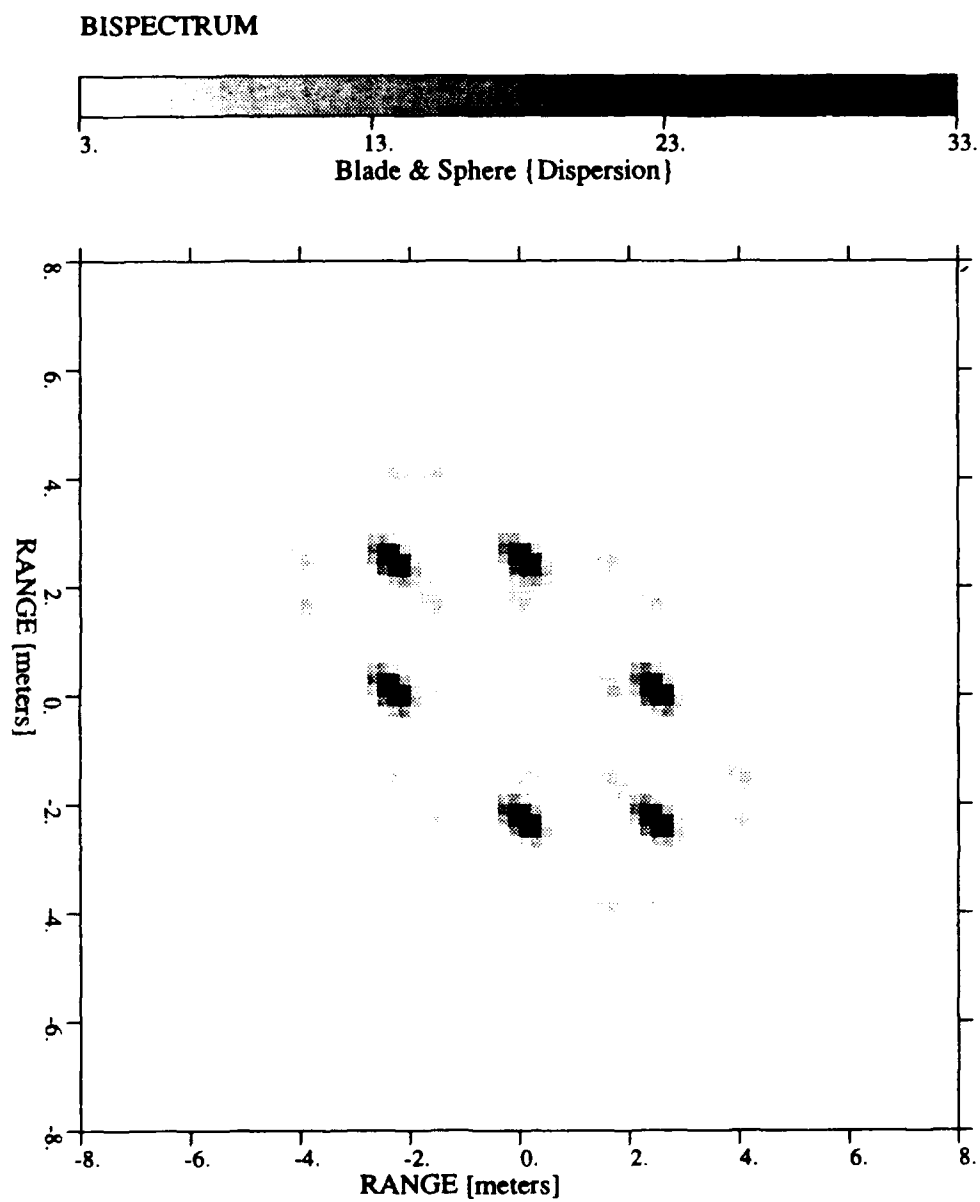


Figure 4.13: Bispectrum of frequency dispersive backscatter for blade-sphere.

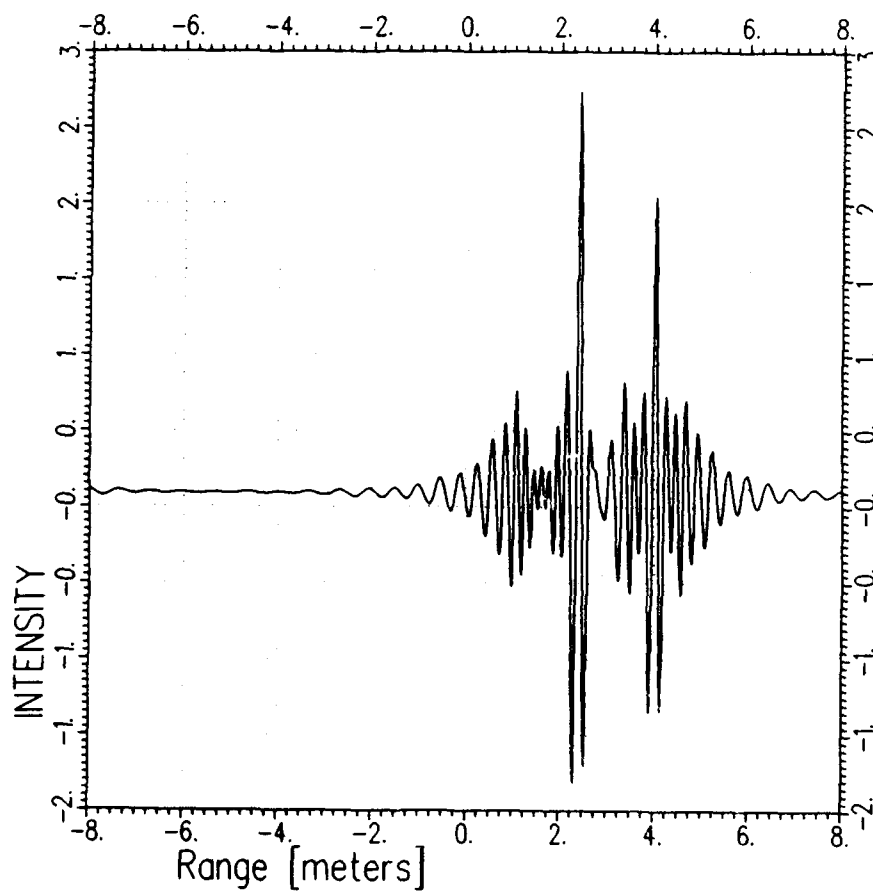


Figure 4.14: Impulse response of frequency dispersive backscatter for blade-sphere.
(single edge dispersion)

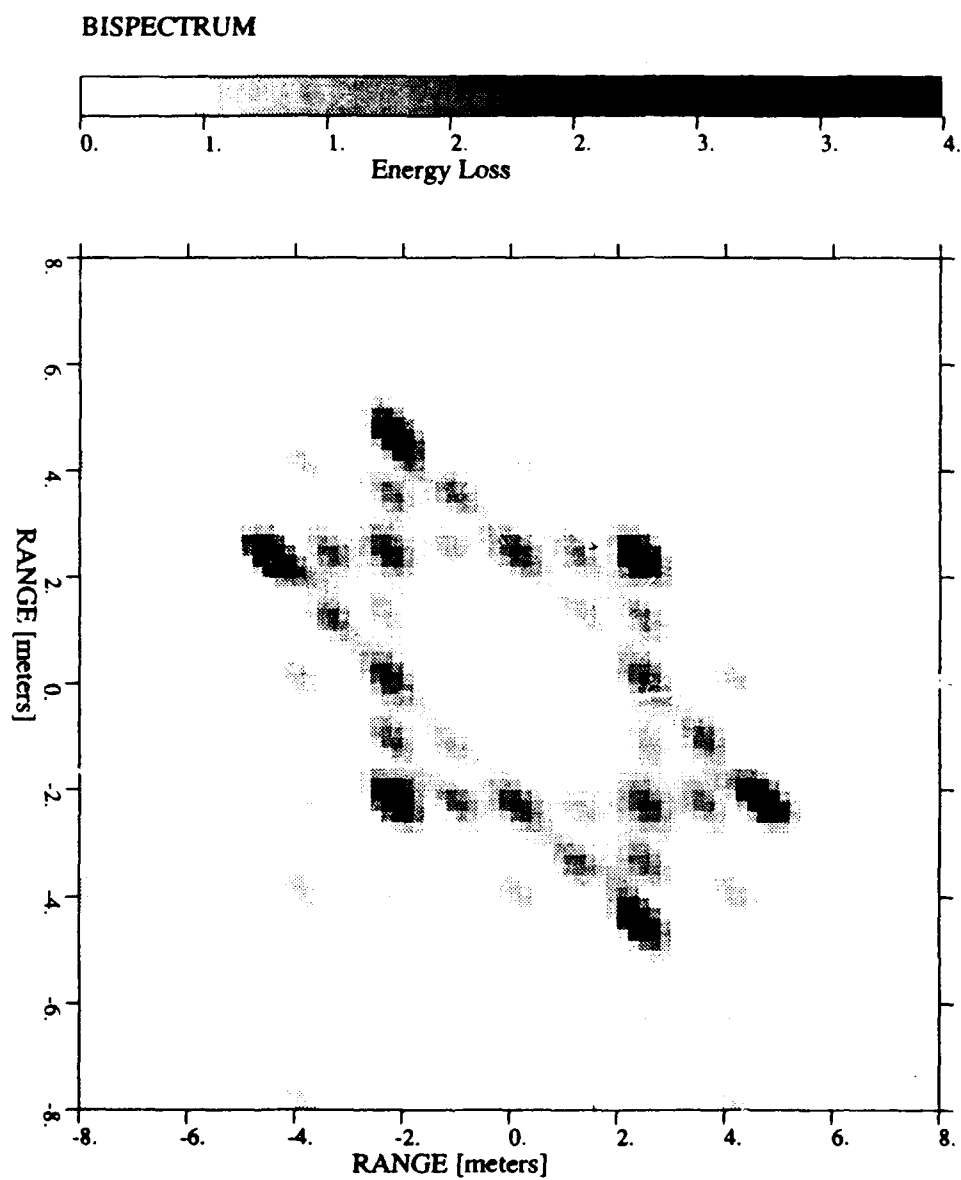


Figure 4.15: Bispectrum of frequency dispersive backscatter for blade-sphere with single edge dispersion

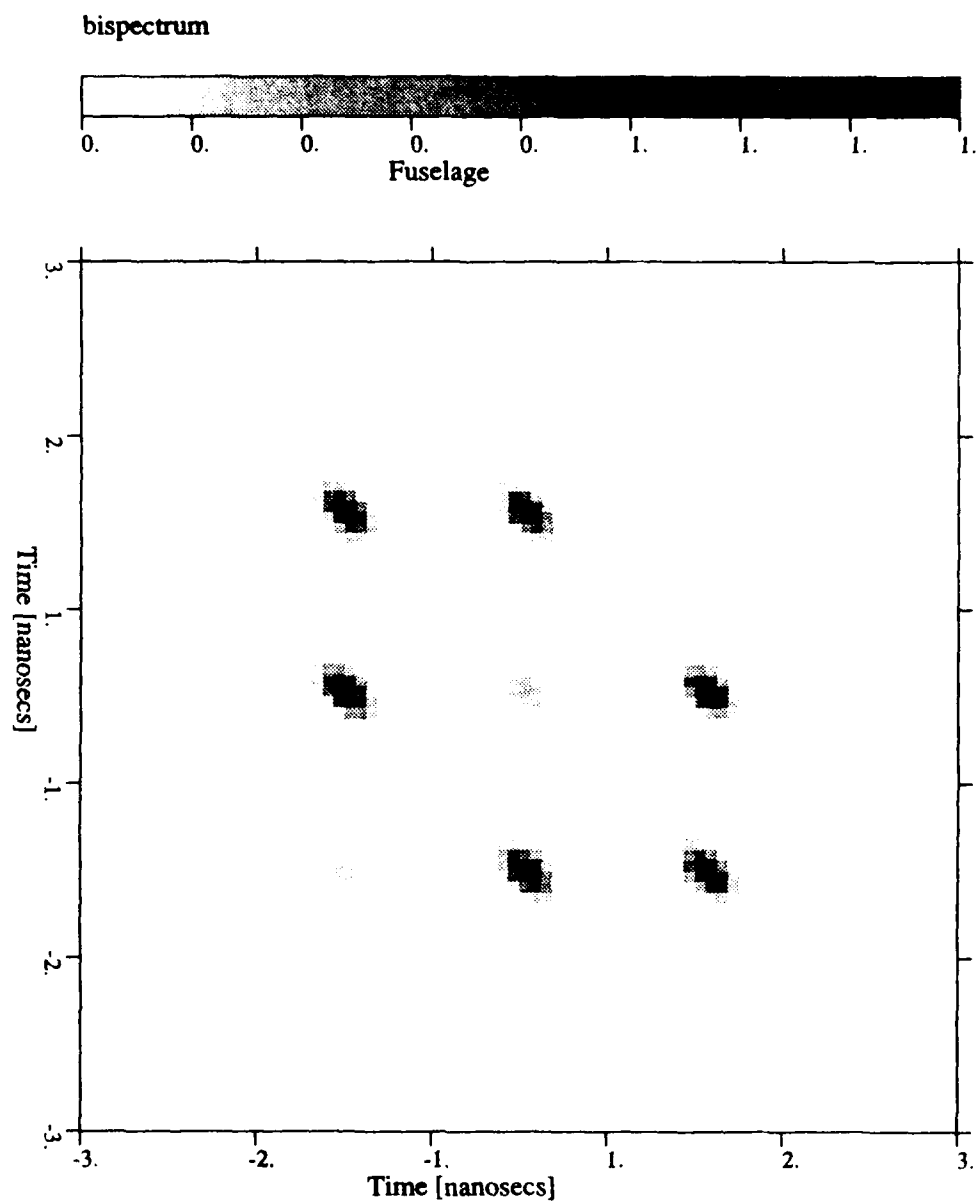


Figure 4.16: Bispectral response for fuselage at 0 degrees azimuth, 0 degrees elevation.

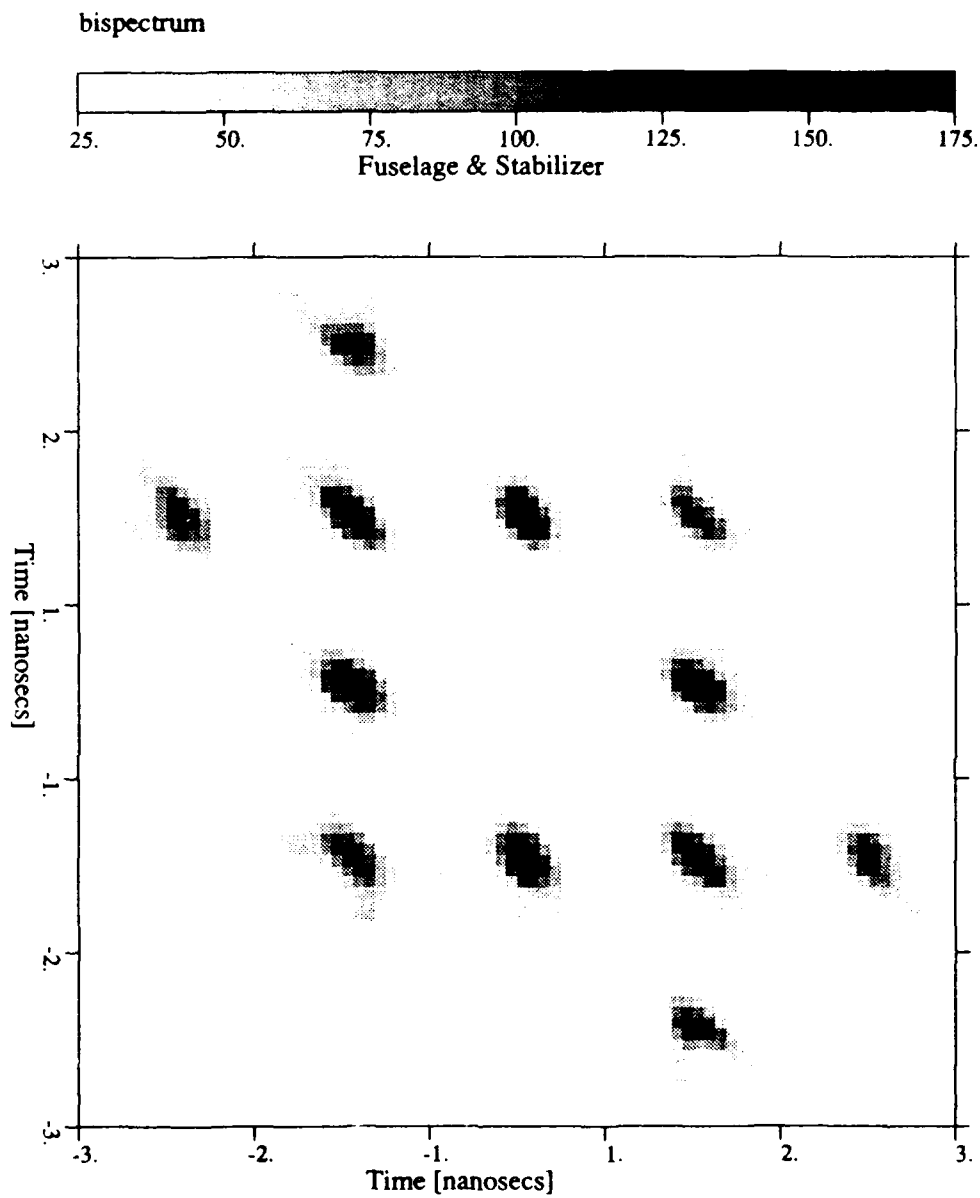


Figure 4.17: Bispectral response for fuselage and stabilizer at 0 degrees azimuth, 0 degrees elevation.

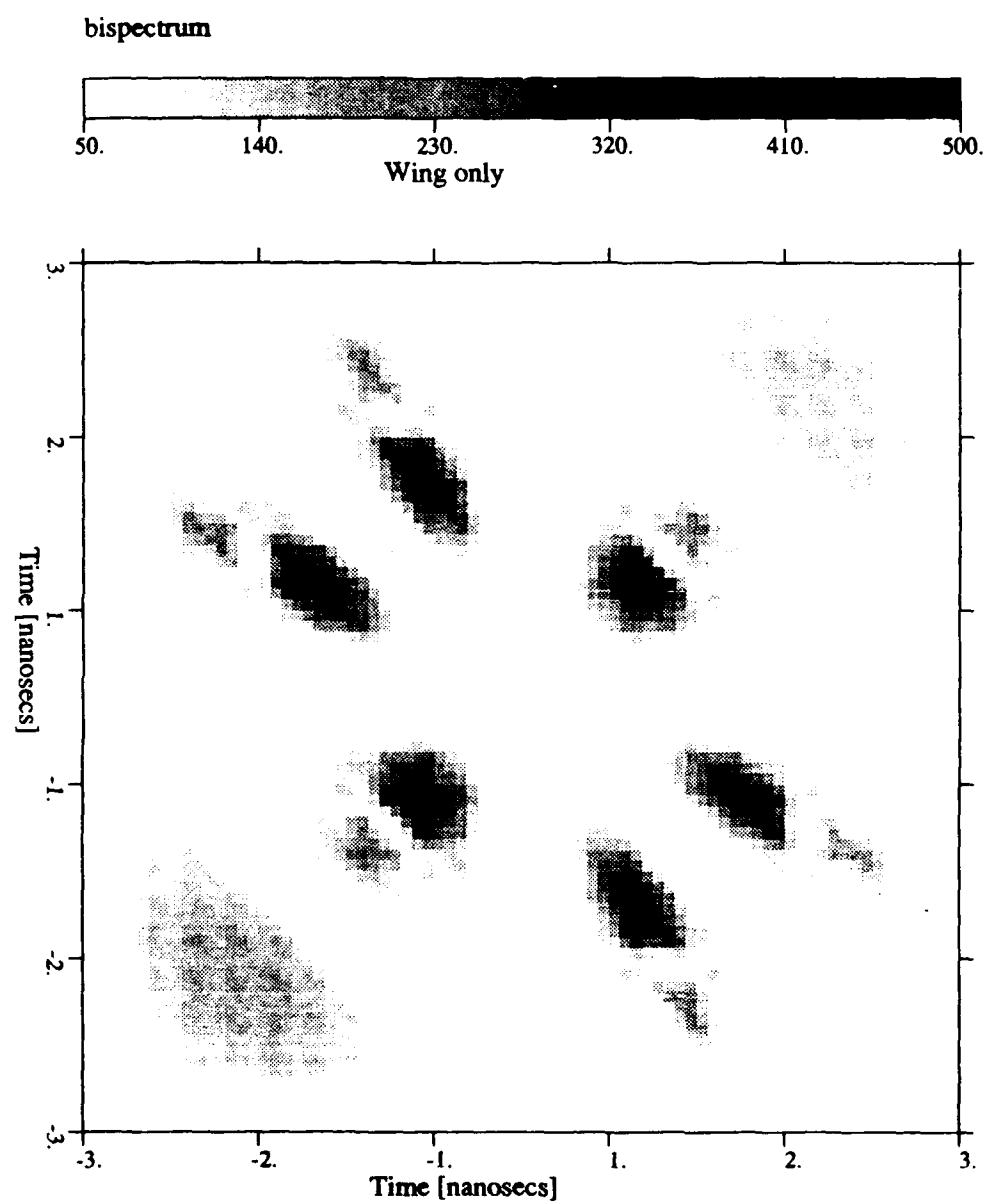


Figure 4.18: Bispectral response for wing at 0 degrees azimuth, 0 degrees elevation.

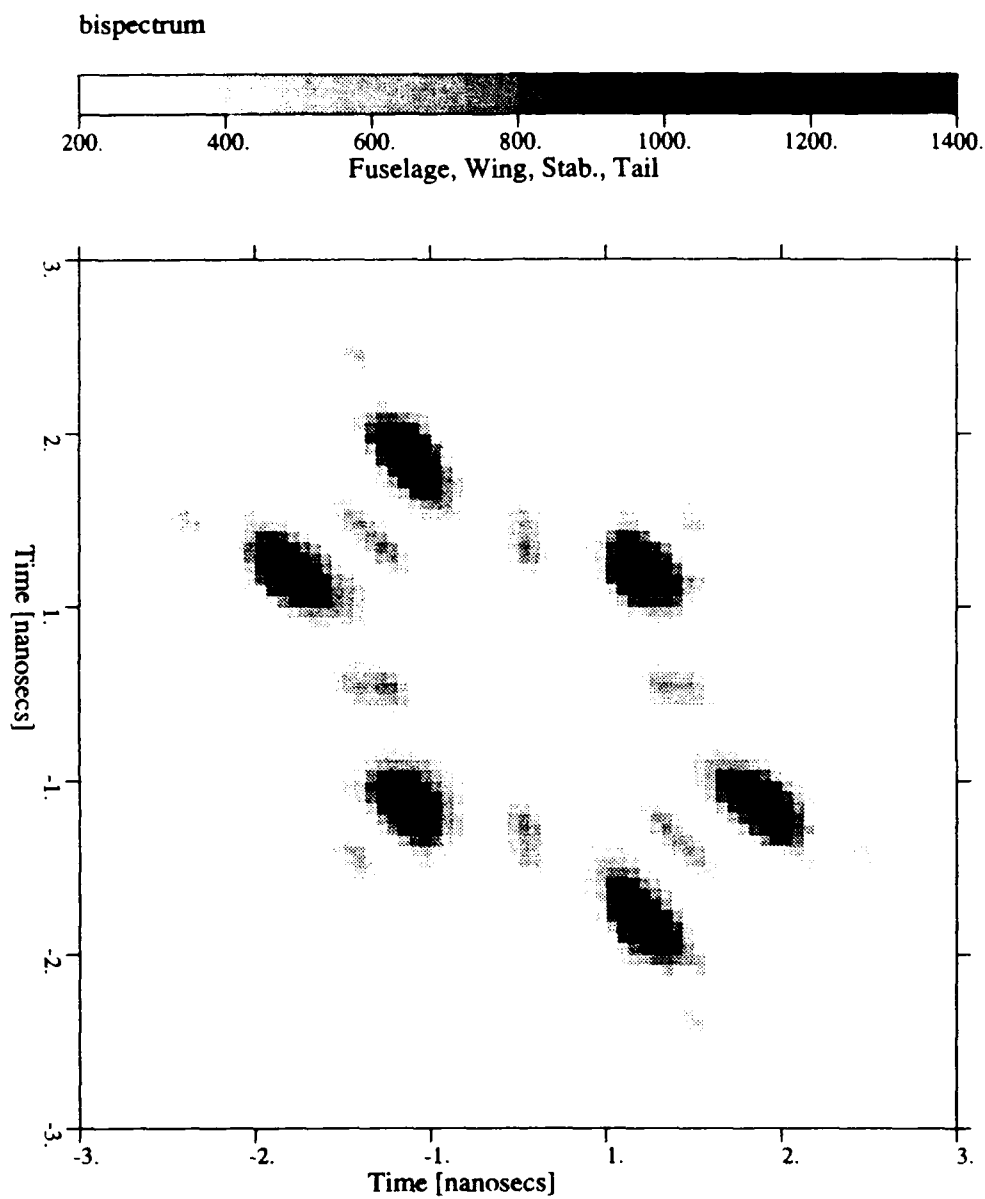


Figure 4.19: Bispectral response for complete canonical aircraft at 0 deg. azimuth, 0 deg. elevation.

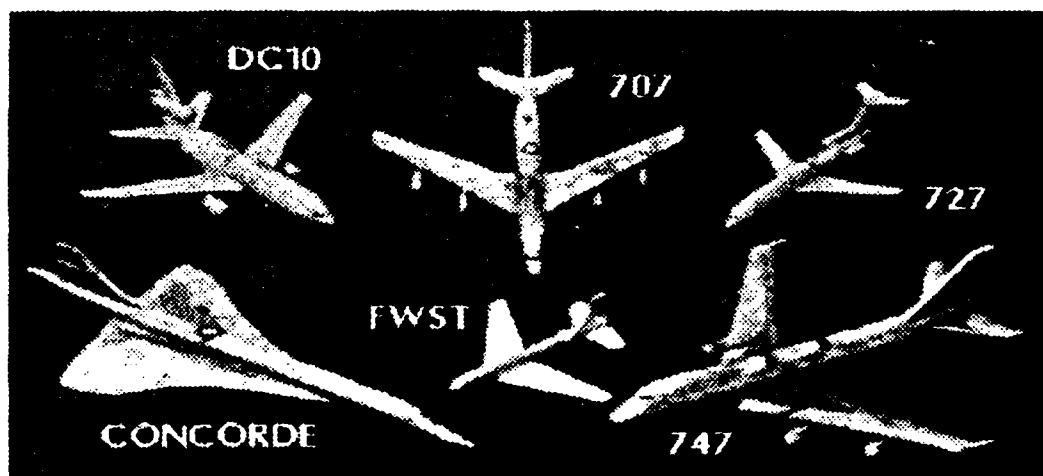


Figure 4.20: Scaled drawings for aircraft used in experimental study

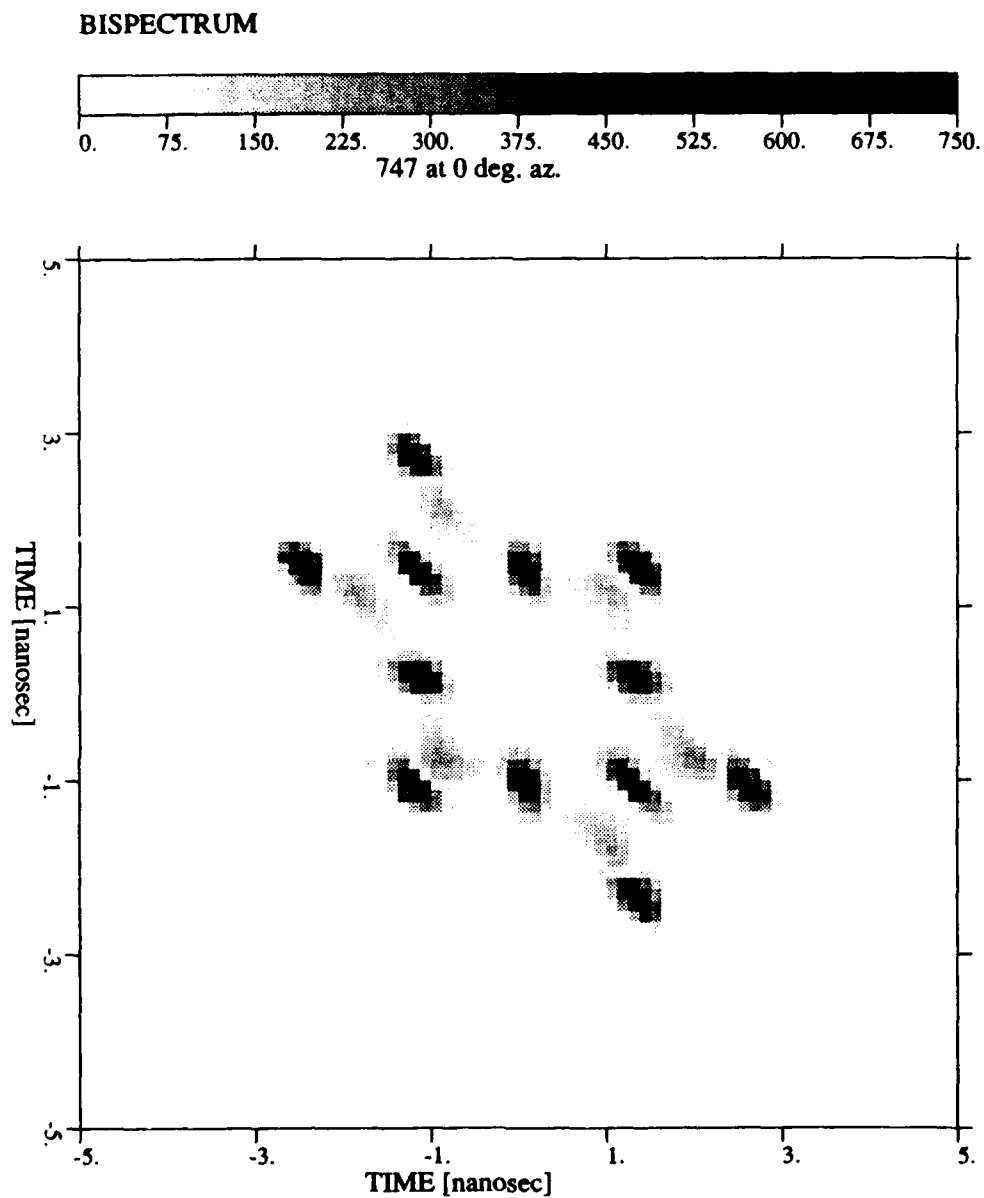


Figure 4.21: Bispectral response for 747 at 0 degrees azimuth, 0 degrees elevation.

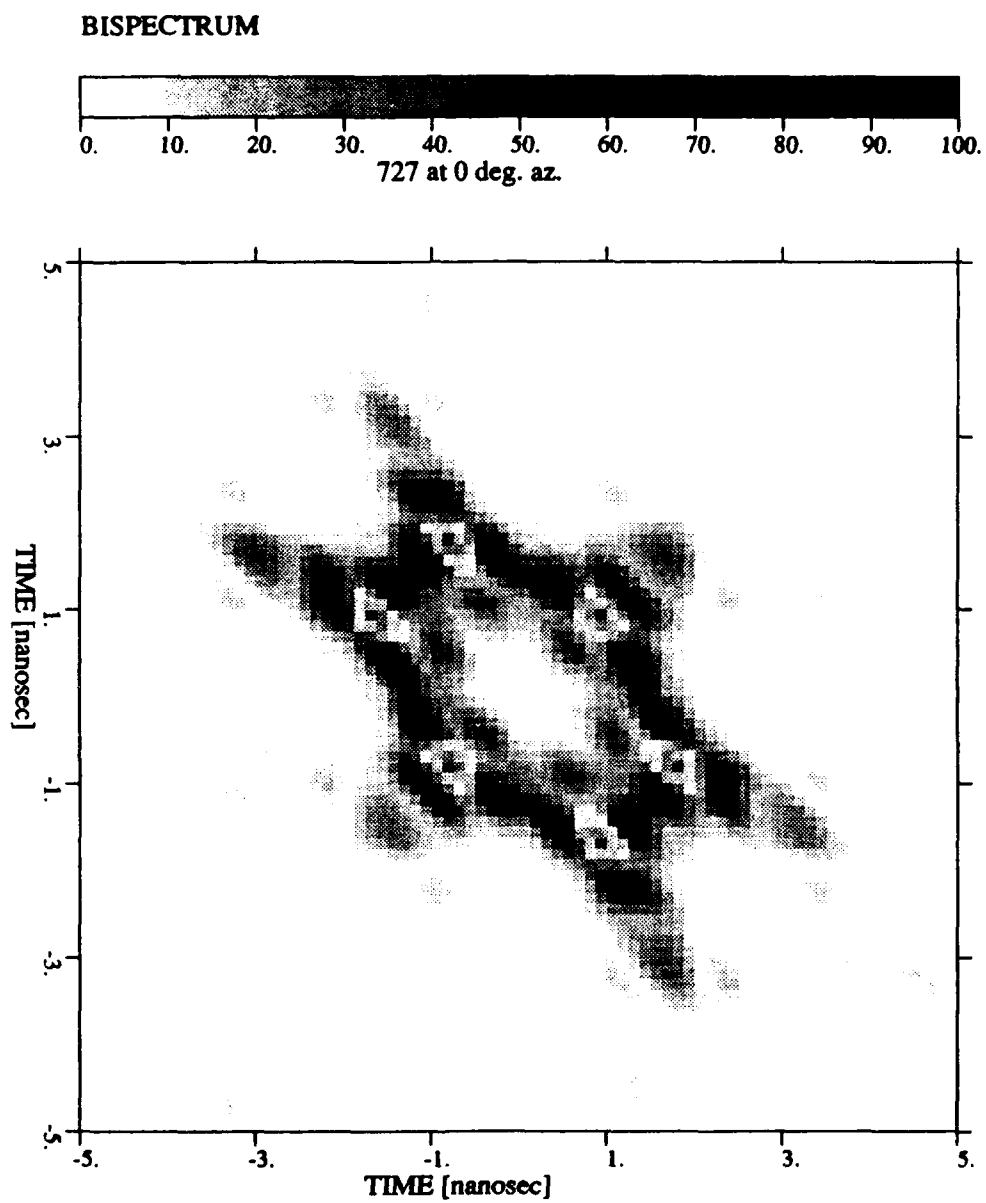


Figure 4.22: Bispectral response for 727 at 0 degrees azimuth, 0 degrees elevation.

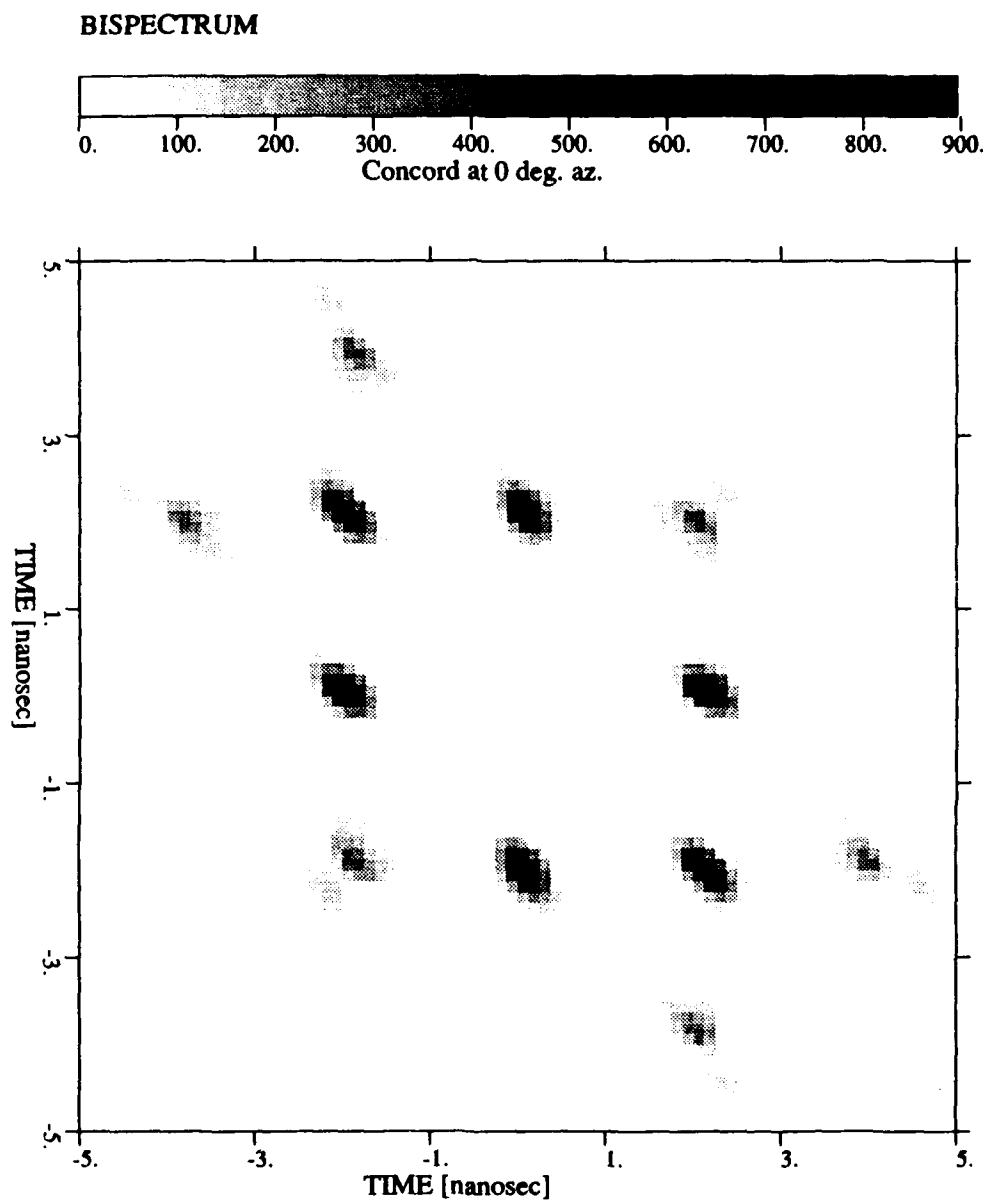


Figure 4.23: Bispectral response for concord at 0 degrees azimuth, 0 degrees elevation.

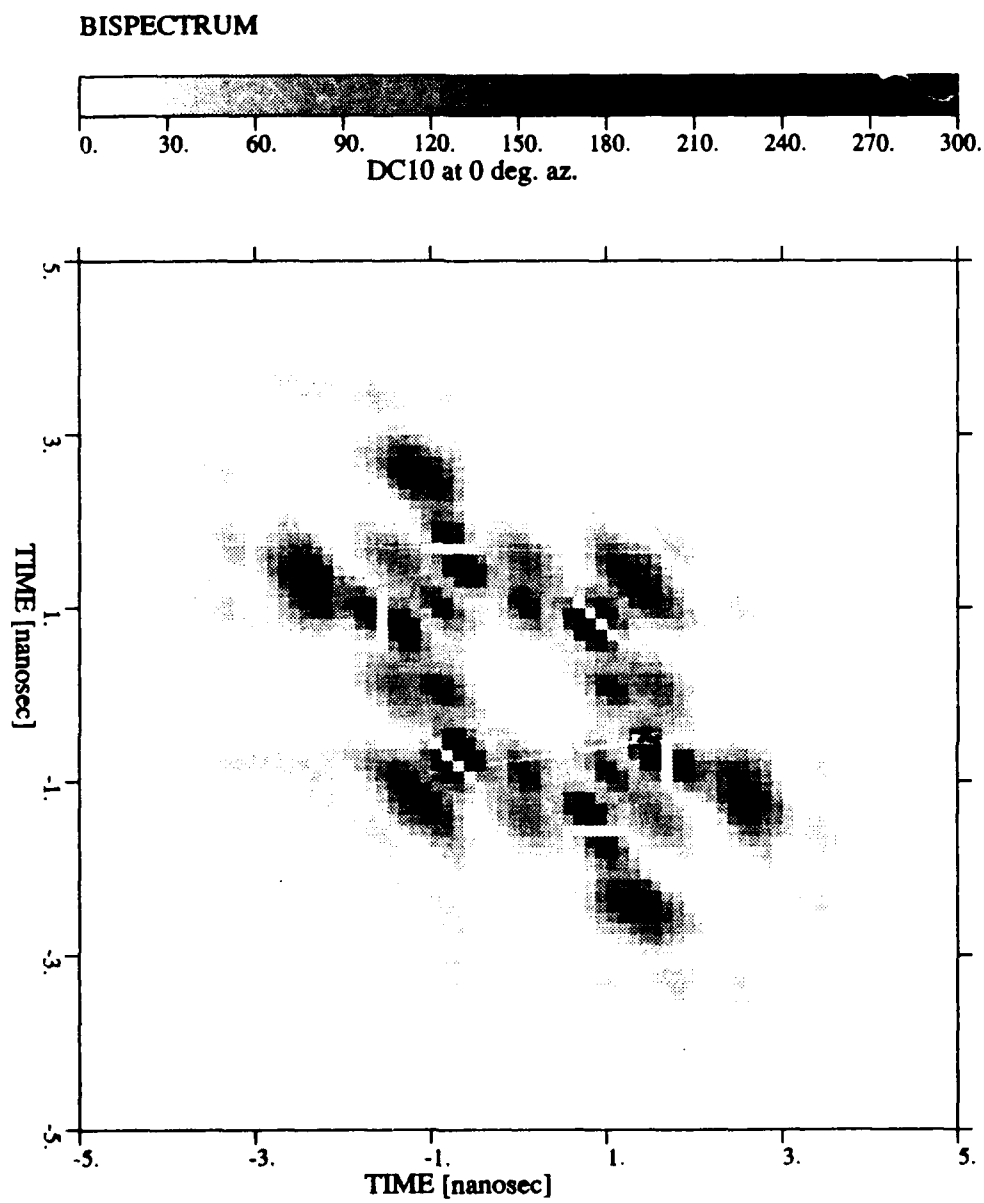


Figure 4.24: Bispectral response for DC10 at 0 degree azimuth, 0 degree elevation.

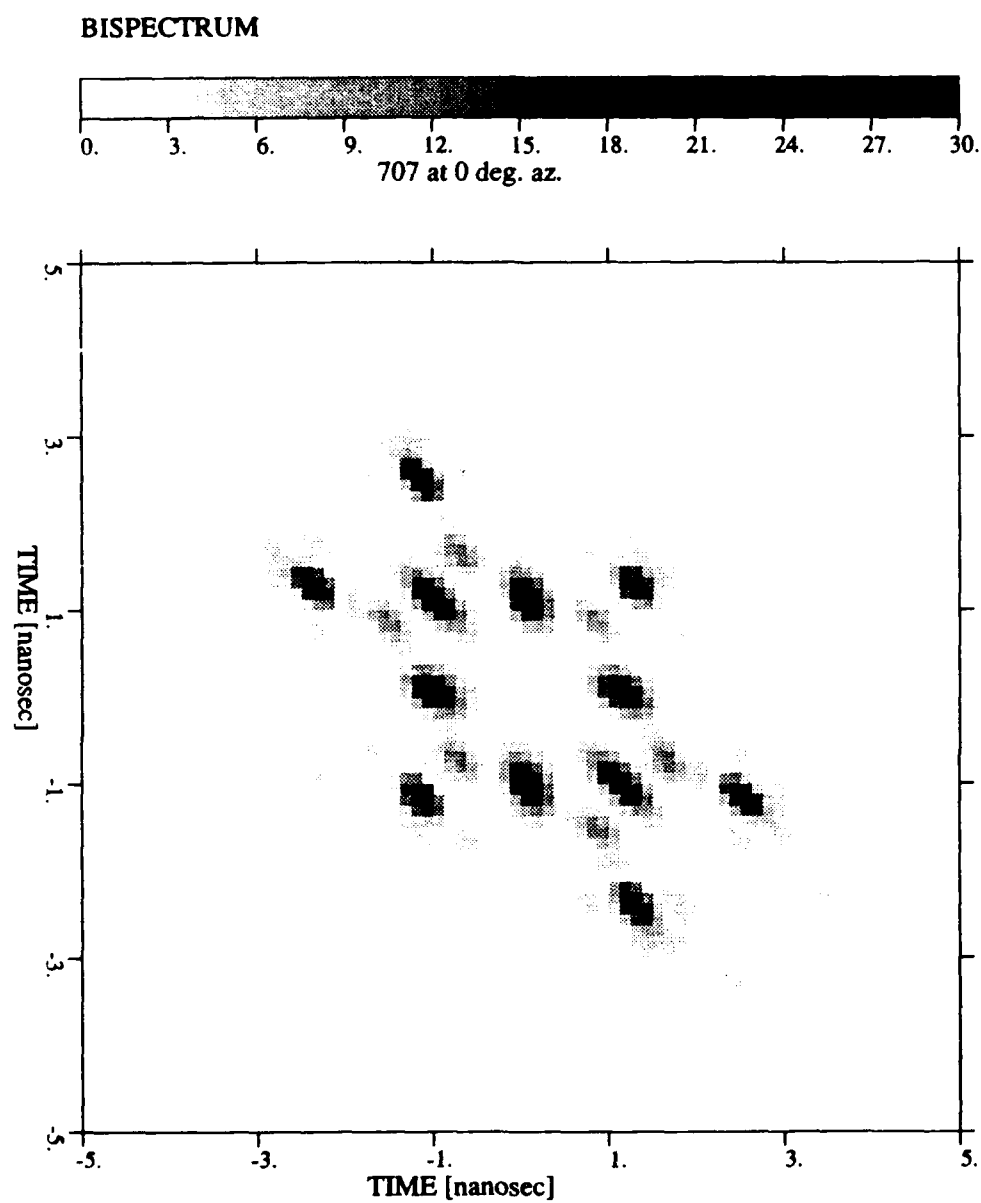


Figure 4.25: Bispectral response for 707 at 0 degrees azimuth, 0 degrees elevation.

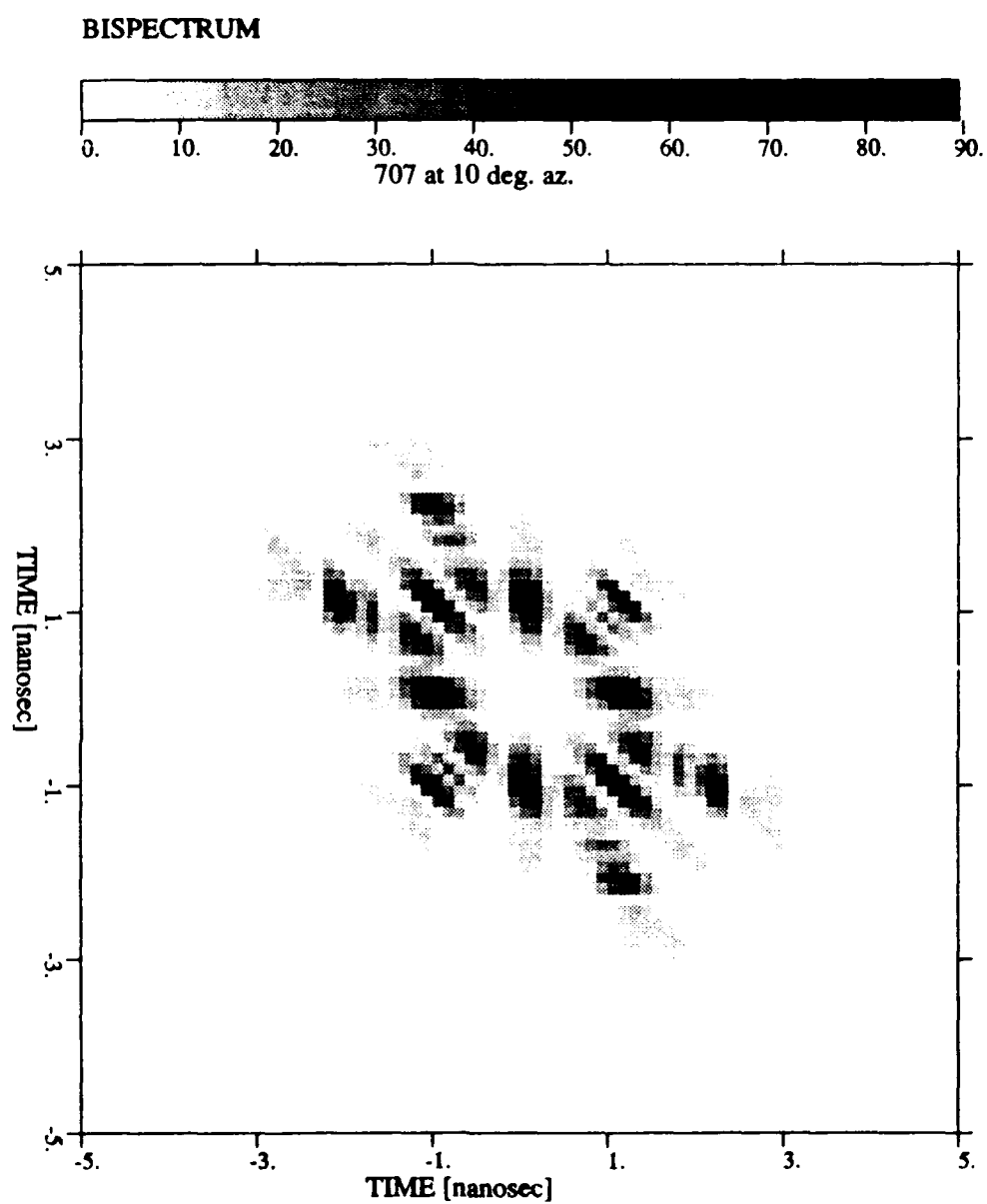


Figure 4.26: Bispectral response for 707 at 10 degrees azimuth, 0 degrees elevation.

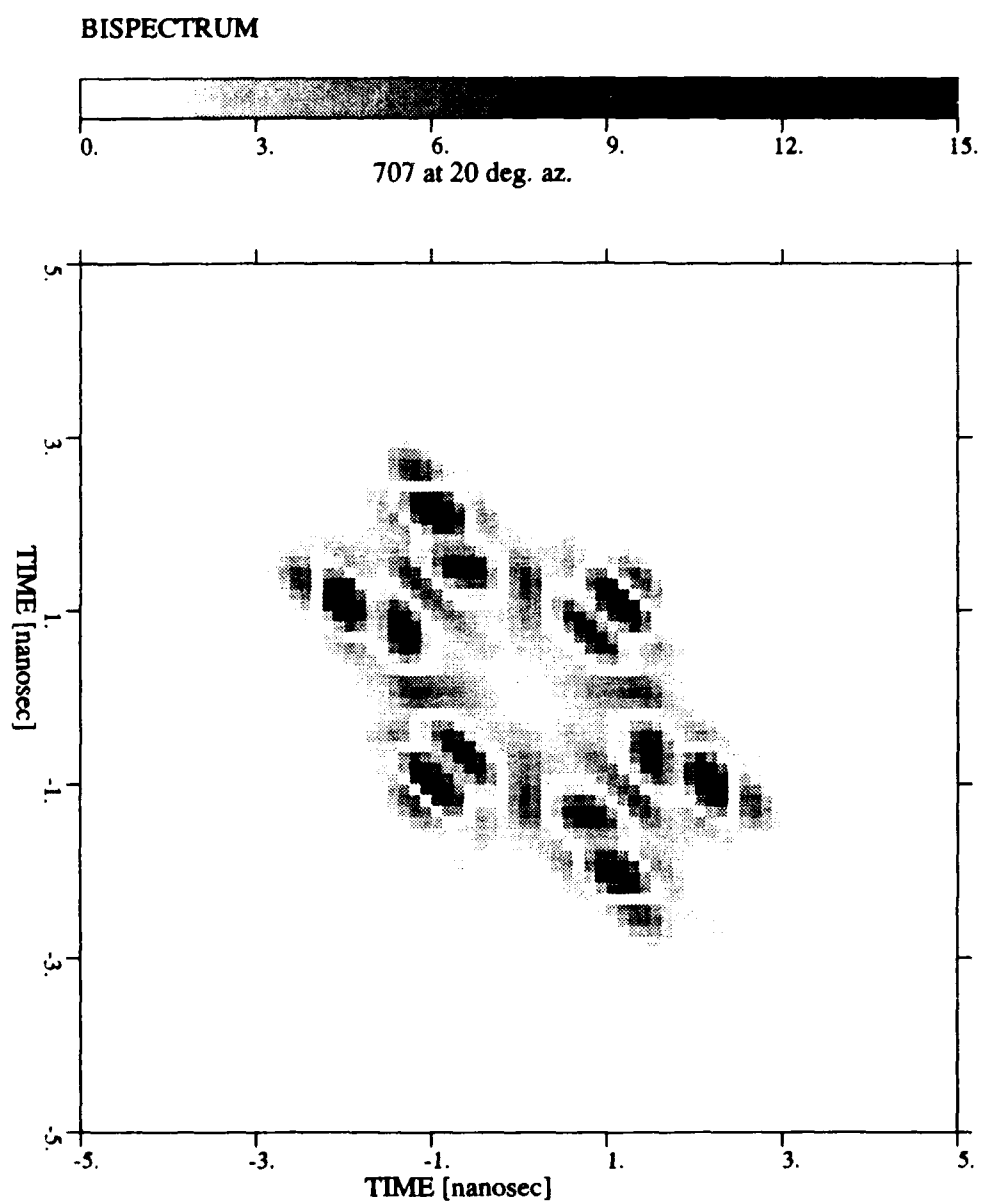


Figure 4.27: Bispectral response for 707 at 20 degree azimuth, 0 degree elevation.

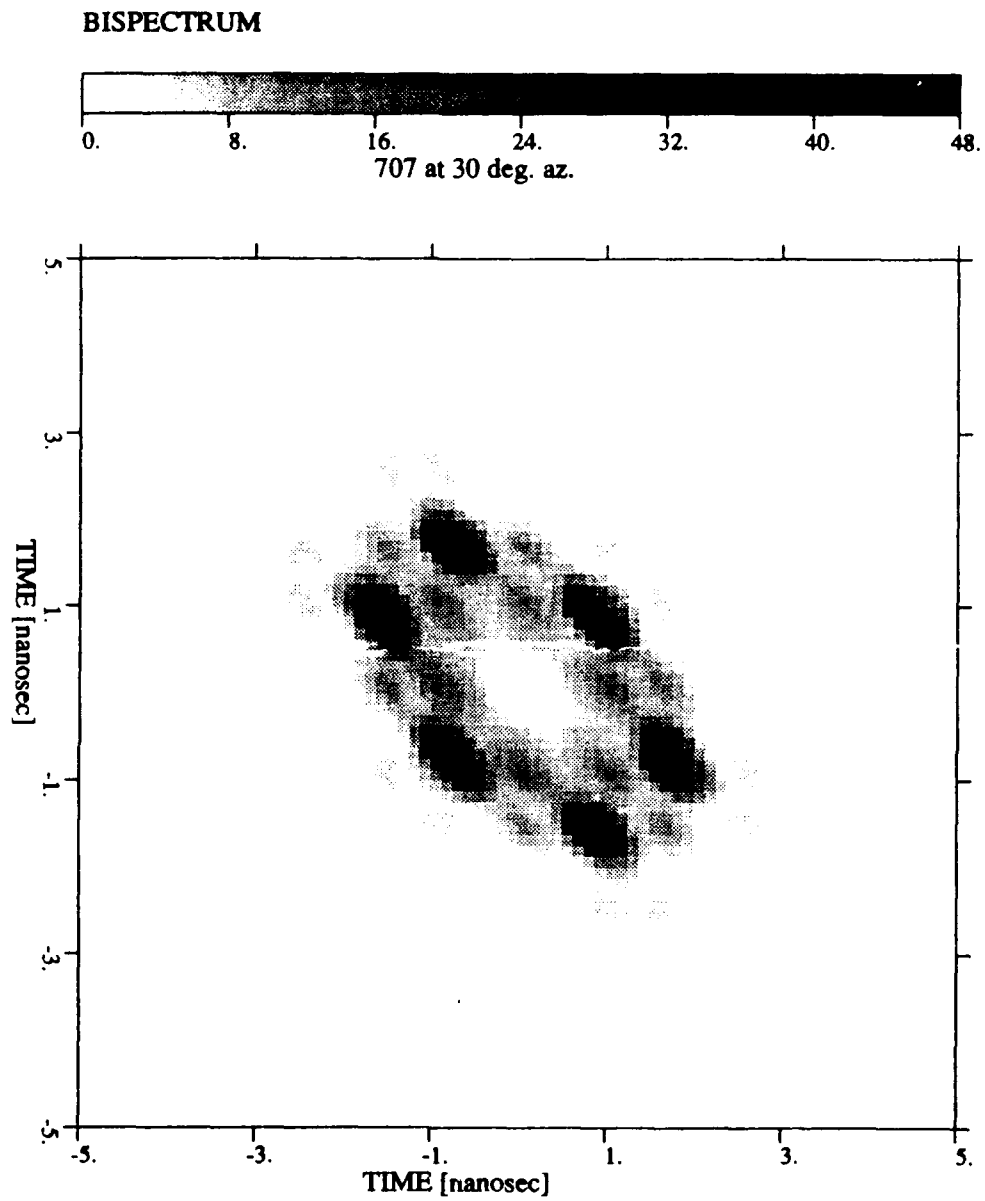


Figure 4.28: Bispectral response for 707 at 30 degree azimuth, 0 degree elevation.

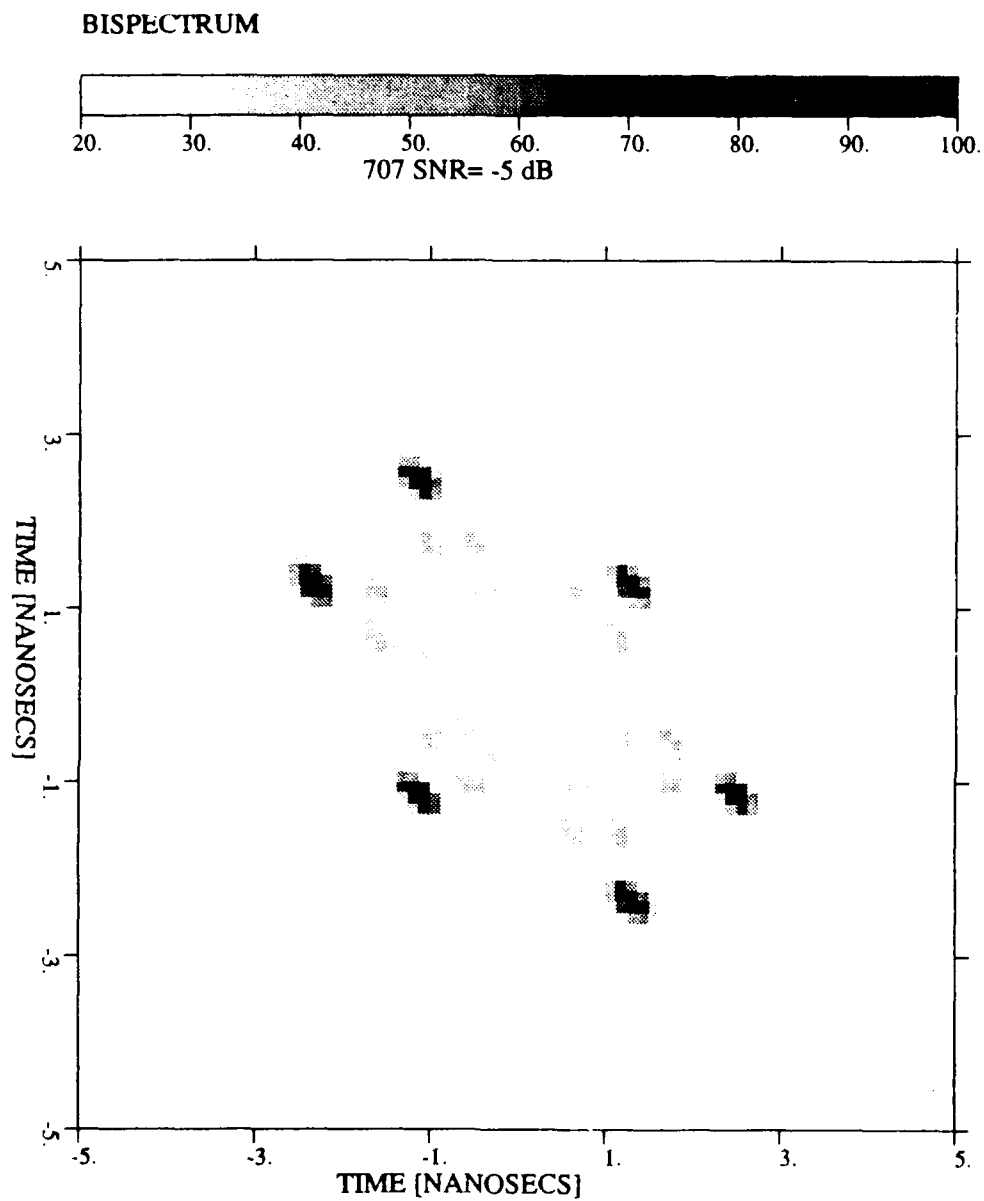


Figure 4.29: Bispectral response for 707 at 0 degrees azimuth, 0 degrees elevation and $SNR = -5dB$.

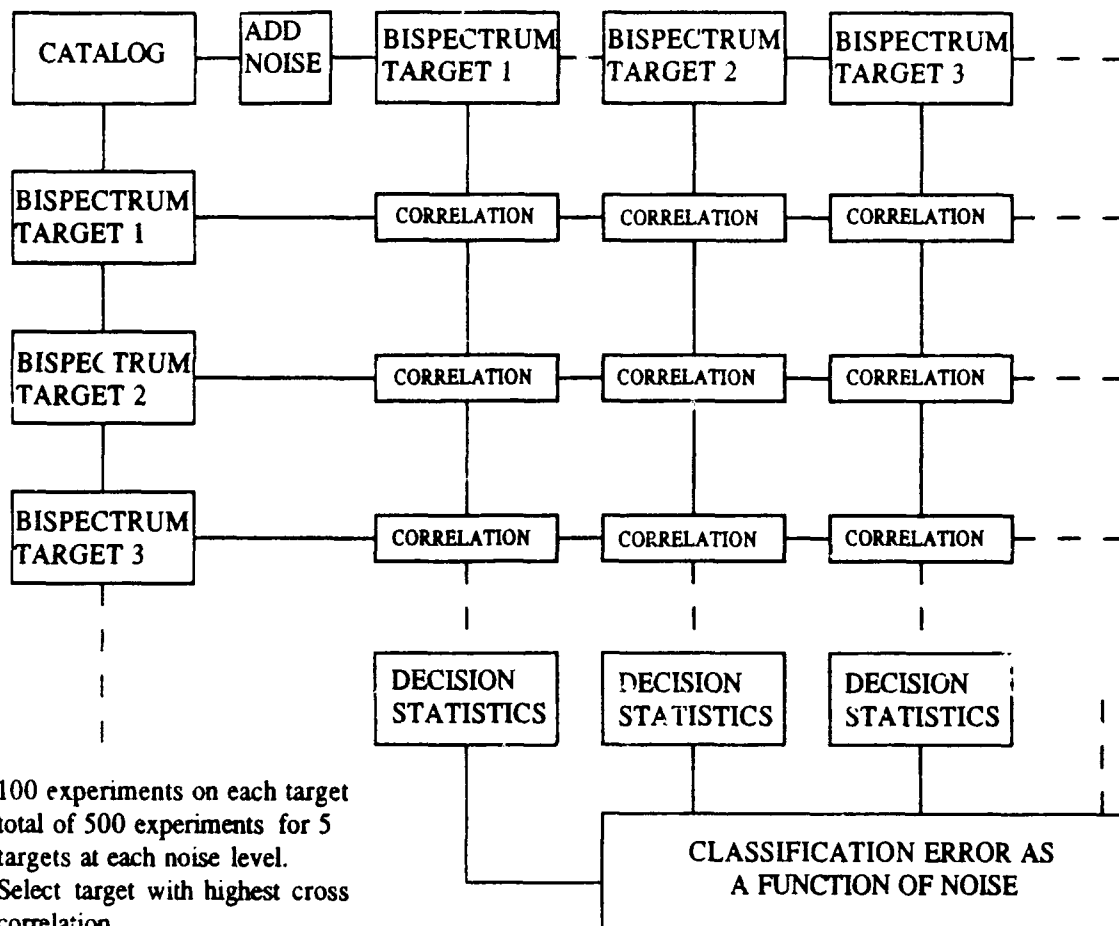


Figure 4.30: Conceptual diagram for bispectral radar target classification algorithm.

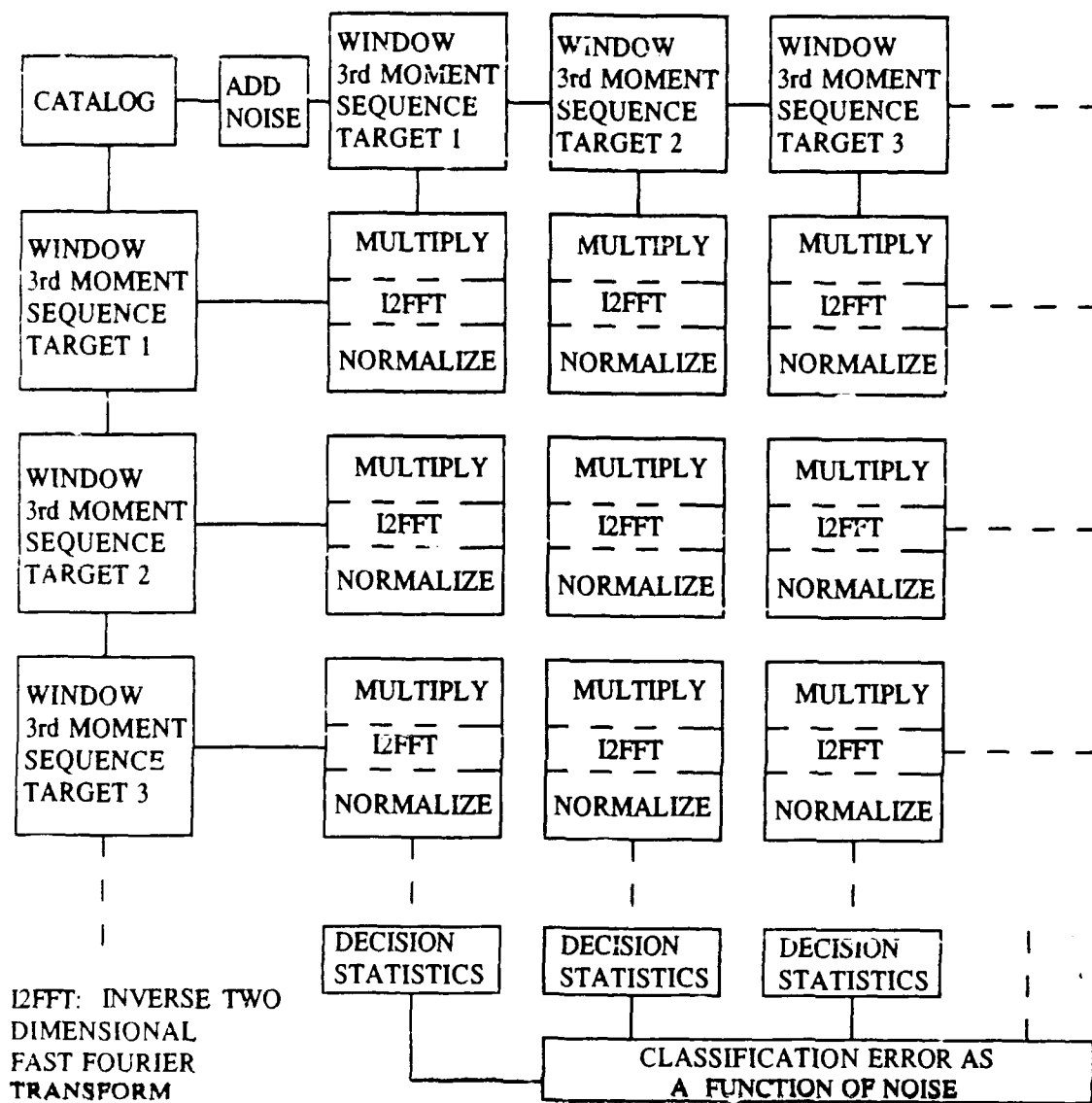


Figure 4.31: Diagram of bispectral radar target classification algorithm as implemented.

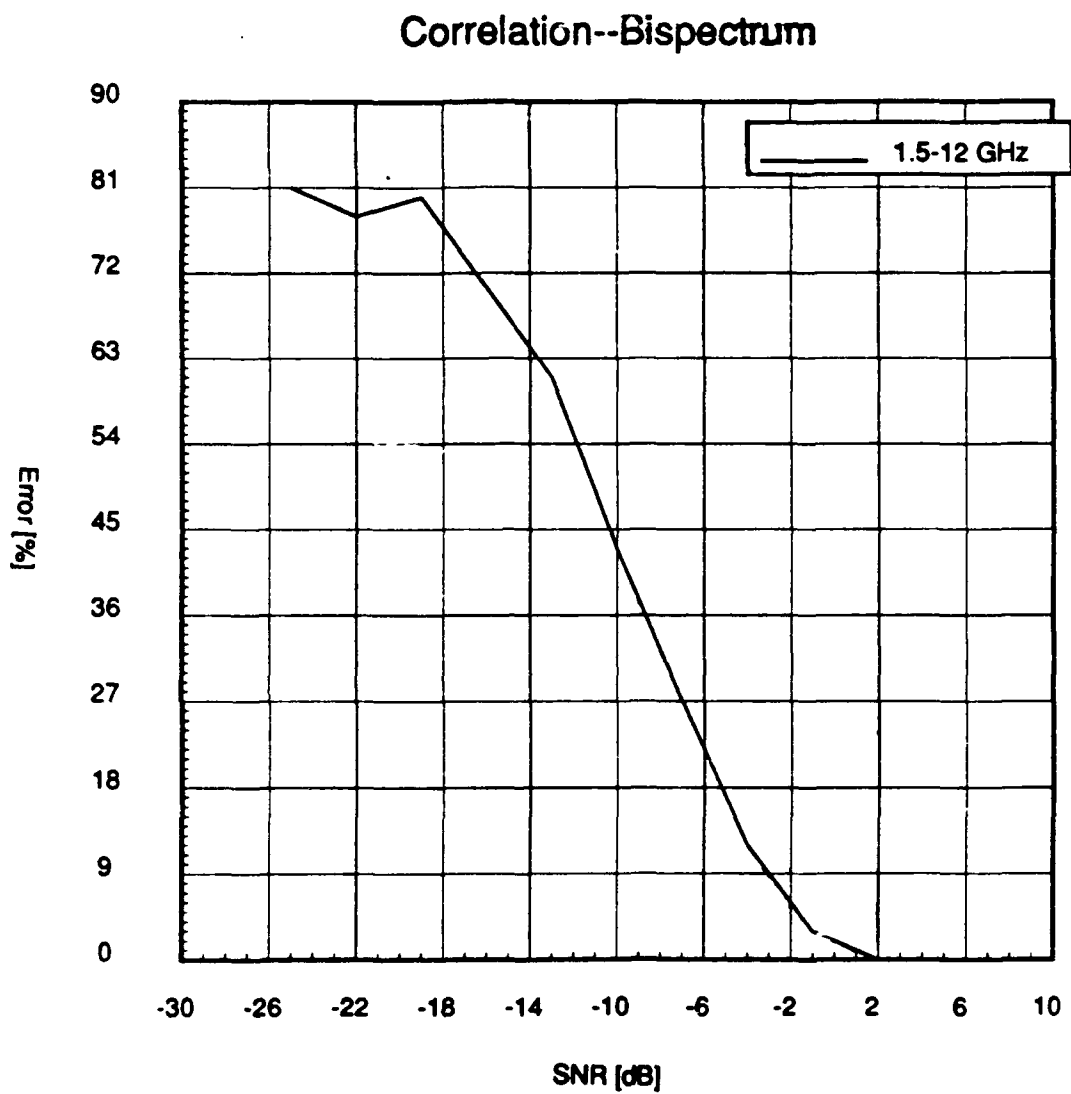


Figure 4.32: Classification performance assuming complete azimuth information.

5. Investigations of Structural Pattern Recognition Methods for Radar Target Identification

5.1 Introduction

One of the more troublesome aspects of the level-crossing based preprocessing methods of [17] is the determination of conditional string probabilities by the histogram method. Convergence of the histograms as well as the issue of unclassifiable strings unnecessarily complicates the investigation of inference of more sophisticated language theoretic classifiers and the computation of the resulting classifiers performance. To circumvent these difficulties, analytical methods for determination of unsqueezed octant crossing and single level crossing have been developed.

Currently, the algorithms are being used to determine misclassification probabilities by Monte-Carlo simulation. This method potentially allows for shorter execution time than the histogram methods of likelihood function estimation used previously, since conditional string probabilities need only be calculated for those strings which occur during the Monte-Carlo test. Furthermore, the problem of un-classifiable strings, as well as the problems related to the matched-noise phenomenon are alleviated. The algorithms which are employed, their current and possible future uses are described in the following section.

While extremely compact, the non-deterministic form of the a syntactic classifier derived in [17] is not particularly revealing in terms of analyzing decision rules induced by such a classifier. In order to gain insight into the resulting decision rules, programs have been developed which convert these classifiers to a deterministic form. The deterministic form resembles a tree classifier. As such, it reveals the relative discriminating power of particular symbol strings. This notion has yet to be formalized.

The deterministic form of the classifier may be used as an analysis tool to help understand how the grammatical inference methods are able to extend decision rules generated by likelihood function estimation. Recall that when likelihood functions estimated by the histogram method are used for decision rule generation (i.e. decisions do not exist for every possible symbolic representation) the grammati-

cal inference method allows the decision regions to *expand* into areas of unknown classification to reduce computational complexity (see [17]). Inspection of the deterministic form of the classifier reveals the extent to which overlapping of the decision regions induced by the grammatical inference method takes place. When coupled with the analytical method of likelihood function estimation, this form of the classifier will be able to quantify the gains realized by the expanded classifier.

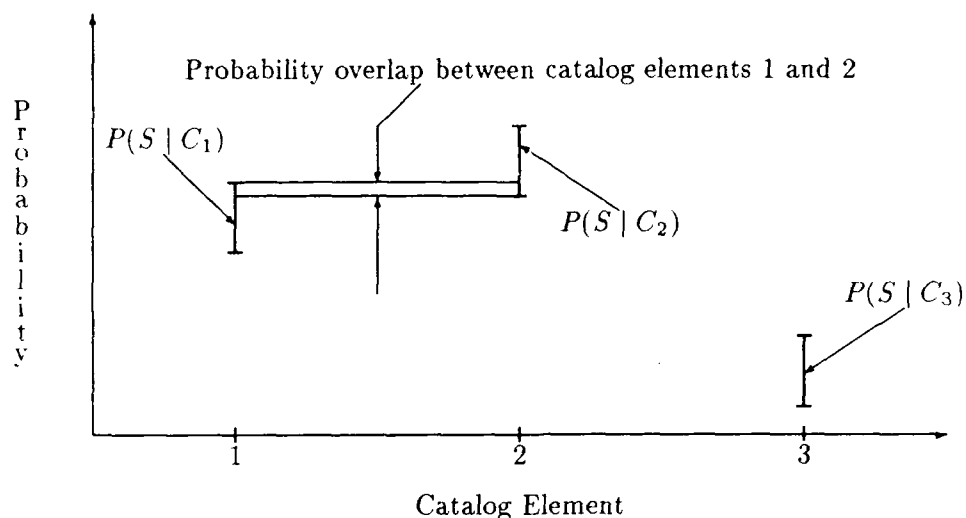


Figure 5.1: Conditional Probability Overlaps

5.2 Analytical Methods for Likelihood Function Determination

The basic algorithm is designed to calculate the conditional string probability for each element of a catalog to within a given tolerance. The string probability calculation procedures use this specified tolerance to determine allowable error for each calculation in the process. These individual errors are set so that the total string probability estimate is within the specified tolerance. The underlying purpose for calculation of the conditional string probabilities is to make a decision as to which catalog element the string was generated under. The maximum likelihood estimate of the generating catalog element is determined by choosing the maximum of the conditional probabilities. A decision can only be made if the band about the maximum conditional probability (the width determined by the given conditional probability tolerance) does not overlap any other bands (see Figure 5.1). Since little is known about a given conditional string probability before estimation, the total string probability tolerance is first set to some nominal value and the conditional string probabilities are determined. If the situation exists, where the maximum conditional probability overlaps some other conditional range of probabilities then

the conditional probabilities are re-calculated with an appropriately decreased tolerance. In this way, the conditional string probability estimation algorithms may be used to make a Bayesian decision about catalog elements.

Clearly, the string probability calculation algorithms may be used for Monte-Carlo test since it allows for a hard decision of any given string. However, these algorithms will allow for grammatical inference with supervision, since the string probability routines may act as a teacher. Furthermore, since the conditional probabilities are available on demand, investigation of information content of the symbolic representation is allowed for as well as investigation of the precise influence of noise on the likelihood functions.

5.2.1 Conditional String Probability Estimation

Each of the probability calculation algorithms involve further layers of error-control iteration beyond the decision process described in the section 5.2. This sub-section describes the first two of these layers. They are common to both the octant crossing and single level crossing schemes and, with modification, would apply to any symbol assignment scheme with adaptive thresholds.

The first layer of error control iteration, accounts for variations in the magnitude threshold by approximating it with a normal random variable. The thresholds of the double level crossing are dependent upon the maximum and the minimum of observed measurements and, as such, involve order statistics of independent Rician random variables.

The second layer of error control iteration involves the relation between individual symbol error and total string error. The technique developed in this section is valid for any symbol assignment scheme in which each symbol corresponds to an independent event. The individual symbol probability estimation procedures are described in the following section.

Magnitude Threshold as a Random Variable

By the definition of the single level crossing and octant crossing schemes, the magnitude threshold used in these schemes is the sum of the individual magnitudes

Equation (5.1). Since the threshold used for string generation is a function of the observation, it too is a random variable. Thus conditional string probabilities are calculated under the assumption of a fixed threshold and integrated with respect to the threshold density to determine the probability of a given string conditioned only on catalog element.

$$T = \frac{1}{N} \sum_{i=1}^N |(a_i)| \quad (5.1)$$

In equation (5.1), T is the magnitude threshold N represents the number of measurements taken and a_i is the i th noisy measurement.

$$P(S | C_i) = \int_{-\infty}^{\infty} P(S | T = t, C_i) P(T = t | C_i) dt \quad (5.2)$$

The individual magnitudes of the observation vector are Rician distributed random variables, by assumption of independent Gaussian noise. Equation (5.1) indicates that the magnitude threshold is a weighted sum of these Rician random variables. Thus, by the central limit theorem, it is reasonable to assume that the magnitude threshold for both schemes is, conditionally, a Gaussian distributed random variable. Furthermore, the central limit theorem indicates the statistics of the magnitude threshold.

$$P(T = t | C_j) = \frac{1}{\sqrt{2\pi\hat{\sigma}_t^2}} e^{-\left(\frac{t-\hat{\mu}_t}{\hat{\sigma}_t}\right)^2} \quad (5.3)$$

And so Equation (5.2) becomes:

$$P(S | C_i) = \frac{1}{\sqrt{2\pi\hat{\sigma}_t^2}} \int_{-\infty}^{\infty} P(S | T = t, C_i) e^{-\left(\frac{t-\hat{\mu}_t}{\hat{\sigma}_t}\right)^2} dt \quad (5.4)$$

In equations (5.3) and (5.4) $\hat{\mu}_t$ is the threshold mean and $\hat{\sigma}_t^2$ is the threshold variance. They are calculated from components of the measurement vector mean, $E[z_i^2]$, and second moment, $E[z_i]^2$.

$$\hat{\mu}_t = \frac{1}{N} \sum_{i=1}^N E[z_i] \quad (5.5)$$

$$\hat{\sigma}_t^2 = \frac{1}{N} \sum_{i=1}^N (E[z_i^2] - E[z_i]^2) \quad (5.6)$$

The components of the measurement vectors' mean and second moment are, in turn functions the magnitude of components of the noiseless measurement vectors, μ_{z_i} , and the per-channel noise variance, σ^2 (the quantity q_i is the ratio $\frac{\mu_{z_i}^2}{2\sigma^2}$).

$$E[z_i] = \sqrt{\frac{\pi}{2}} e^{\frac{-q_i}{2}} \sigma \left[(1 + q_i) I_0\left(\frac{q_i}{2}\right) + q_i I_1\left(\frac{q_i}{2}\right) \right] \quad (5.7)$$

$$E[z_i^2] = \mu_{z_i}^2 + 2\sigma^2 \quad (5.8)$$

The Gaussian Quadrature method is used to approximate the integral of Equation (5.2) with a sum (see Reference [18]).

$$P(S | C_i) \approx \sum_{k=1}^m H_k P(S | T = x_k, C_i) P(T = x_k | C_i) \quad (5.9)$$

This method chooses the abscissas (x_k) and the weights (H_k) in such a way as to minimize the error between the integral and the sum; exact answers are obtained for polynomials of degree $m - 1$ or less. Gaussian Quadrature with Hermite weighting is used to approximate integrals with weighting functions of the form $w(t) = e^{-t^2}$. Thus a change of variable is made to put Equation (5.4) into such a form.

$$x = h(t) = \frac{t - \hat{\mu}_t}{\hat{\sigma}_t} \quad (5.10)$$

$$t = h^{-1}(x) = \hat{\sigma}_t x + \hat{\mu}_t \quad (5.11)$$

And so Equation (5.4) becomes:

$$P(S | C_i) = \frac{1}{\sqrt{2\pi}} \int_{-\infty}^{\infty} P(S | T = h^{-1}(x), C_i) e^{-x^2} dx \quad (5.12)$$

Gaussian Quadrature with Hermite weighting may now be used to approximate the integral of Equation (5.12):

$$P(S | C_i) \approx \sum_{k=1}^m \tilde{H}_k P(S | T = h^{-1}(\tilde{x}_k), C_i) \quad (5.13)$$

The error associated with an estimate using Gauss-Hermite Quadrature is given in Reference [18] as:

$$E = \frac{\sqrt{\pi}m!}{2^m} f[t_1, t_1, t_2, t_2, \dots, t_m, t_m, \xi_1] \quad (5.14)$$

To obtain an estimate of this error, the divided difference ($f[t_1, t_1, t_2, t_2, \dots, t_m, t_m, \xi_1]$) of the string probability function is obtained by evaluating this function at $2m + 1$ points instead of m points as required by the Gauss-Hermite Quadrature rule. This procedure more than doubles the computation time required to calculate the probability of a given string, however, this is necessary to control the error and arrive at a valid decision. Once this error is obtained, it is compared with the designated error of the string probability function and the total error is taken to be the maximum of the two.

String Probability Error vs Symbol Probability Error

Both algorithms build up total string probabilities from individual symbol probabilities. Since the noise corruption is assumed independent between measurements, any given string probability is the product of the constituent symbol probabilities. Thus, in the absence of estimation errors the true total string probability, $P(S)$, is related to the true symbol probabilities, $P(a_i)$ by:

$$P(S) = \prod_{i=1}^N P(a_i) \quad (5.15)$$

However, exact values of the symbol probabilities are not available. Thus if we define the total string absolute error to be E and the i th symbol probability absolute error to be ϵ_i then equation (5.15) becomes:

$$P(S) + E = \prod_{i=1}^N (P(a_i) + \epsilon_i) \quad (5.16)$$

As stated above, total string probabilities are calculated to within a given tolerance. In order to guarantee that relative error on the total string probability is below some maximum (E_{relmax}), a maximum relative error for symbol probability estimation is supplied to symbol probability estimation routines. The defining property of the relative maximum symbol probability error is:

$$\left| \frac{\epsilon_i}{P(a_i)} \right| \leq \epsilon_{\text{relmax}}, \quad \forall 1 \leq i \leq N \quad (5.17)$$

This maximum relative error for the symbol probabilities is calculated from the designated string probability relative error by:

$$\epsilon_{\text{relmax}} = \sqrt[N]{E_{\text{relmax}} + 1} - 1 \quad (5.18)$$

This guarantees that the actual total string relative error will be less than the designated maximum since:

$$E = \prod_{i=1}^N P(a_i) + \prod_{i=1}^{N-1} P(a_i) \epsilon_N + \prod_{i=1}^{N-2} P(a_i) \epsilon_{N-1} P(a_i) + \dots \quad (5.19)$$

$$+ \prod_{i=1}^N \epsilon_i - P(S)$$

$$E = \left(\prod_{i=1}^N P(a_i) \right) \left[\sum_{i=1}^N \left(\frac{\epsilon_i}{P(a_i)} \right) + \sum_{i=1}^{N-1} \sum_{j=i+1}^N \left(\frac{\epsilon_i}{P(a_i)} \right) \left(\frac{\epsilon_j}{P(a_j)} \right) \right. \quad (5.20)$$

$$+ \sum_{i=1}^{N-2} \sum_{j=i+1}^{N-1} \sum_{k=j+1}^N \left(\frac{\epsilon_i}{P(a_i)} \right) \left(\frac{\epsilon_j}{P(a_j)} \right) \left(\frac{\epsilon_k}{P(a_k)} \right) + \dots$$

$$\left. + \prod_{i=1}^N \left(\frac{\epsilon_i}{P(a_i)} \right) \right]$$

$$\left| \frac{E}{P(S)} \right| = \left| \sum_{i=1}^N \left(\frac{\epsilon_i}{P(a_i)} \right) + \sum_{i=1}^{N-1} \sum_{j=i+1}^N \left(\frac{\epsilon_i}{P(a_i)} \right) \left(\frac{\epsilon_j}{P(a_j)} \right) \right. \quad (5.21)$$

$$+ \sum_{i=1}^{N-2} \sum_{j=i+1}^{N-1} \sum_{k=j+1}^N \left(\frac{\epsilon_i}{P(a_i)} \right) \left(\frac{\epsilon_j}{P(a_j)} \right) \left(\frac{\epsilon_k}{P(a_k)} \right) + \dots$$

$$\left. + \prod_{i=1}^N \left(\frac{\epsilon_i}{P(a_i)} \right) \right|$$

$$\left| \frac{E}{P(S)} \right| \leq \sum_{i=1}^N \left| \frac{\epsilon_i}{P(a_i)} \right| + \sum_{i=1}^{N-1} \sum_{j=i+1}^N \left| \frac{\epsilon_i}{P(a_i)} \right| \left| \frac{\epsilon_j}{P(a_j)} \right| \quad (5.22)$$

$$+ \sum_{i=1}^{N-2} \sum_{j=i+1}^{N-1} \sum_{k=j+1}^N \left| \frac{\epsilon_i}{P(a_i)} \right| \left| \frac{\epsilon_j}{P(a_j)} \right| \left| \frac{\epsilon_k}{P(a_k)} \right| + \dots$$

$$+ \prod_{i=1}^N \left| \frac{\epsilon_i}{P(a_i)} \right|$$

$$\left| \frac{E}{P(S)} \right| \leq \binom{N}{1} \epsilon_{\text{relmax}} + \binom{N}{2} \epsilon_{\text{relmax}}^2 + \binom{N}{3} \epsilon_{\text{relmax}}^3 + \dots \quad (5.23)$$

$$+ \binom{N}{N} \epsilon_{\text{relmax}}^N$$

$$\left| \frac{E}{P(S)} \right| \leq (1 + \epsilon_{\text{relmax}})^N - 1 \quad (5.24)$$

$$\left| \frac{E}{P(S)} \right| \leq E_{\text{relmax}} \quad (5.25)$$

5.2.2 Conditional Symbol Probability Calculations

Estimation of the conditional symbol probabilities makes use of standard routines for calculation of the error function or the Marcum Q function. Parls method [19] of recursively computing the Marcum Q function was used for single level crossing strings. The region of integration for the octant crossing symbol assignments is not the standard rectangular region usually associated with a bivariate normal random variable. As such, approximations to the region are made by sums of probabilities with rectangular regions of integration. This extension of the bivariate normal cumulative distribution function routine is considered the only source of error for the octant crossing symbol probability routine.

Octant Crossing

Octant crossing total string conditional probability estimates are made from corresponding symbol probability estimates. By assumption of independent Gaussian noise, an individual octant crossing symbol probability given a particular threshold, catalog element and location within the string, may be estimated by the formula:

$$P(a_i \mid T = t, C_j, i) = \frac{1}{2\pi\sigma^2} \int_{\Omega_{a_i}} e^{-\frac{1}{2}\left(\frac{u-x_i}{\sigma}\right)^2} e^{-\frac{1}{2}\left(\frac{v-y_i}{\sigma}\right)^2} dudv \quad (5.26)$$

In equation (5.26), Ω_{a_i} is the region of plane corresponding to symbol a_i . The symbols x_i and y_i are the real and imaginary component of the i th measurement.

The integral in equation (5.26) is calculated by transforming the coordinates so that the region Ω_{a_i} corresponds to the 7th or 3rd octant (see Figure 5.2). Since

octant	phase	magnitude
1	0-90	below
2	90-180	below
3	180-270	below
4	270-0	below
5	0-90	above
6	90-180	above
7	180-270	above
8	270-360	above

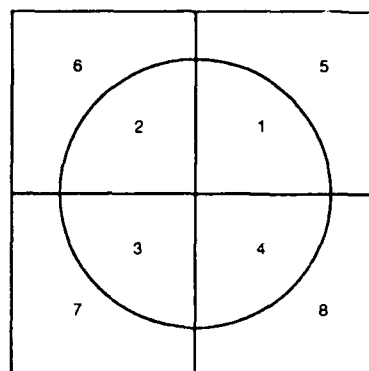


Figure 5.2: Octant crossing primitive assignments.

calculating the probability of a rectangular region, of a Gaussian bivariate random variable is relatively simple, the probability of the 7th octant is approximated with the sum of probabilities of such regions. This is accomplished by first determining a lower bound for the integral.

This lower bound is taken to be the integral over a *staircase* shaped region which approximately covers the 7th octant region and is inscribed by the 7th octant region (see Figure 5.3). The staircase region is determined such that the *points* of the stairs are equally spaced in angle. The probability of the staircase region is determined from a sum of the probabilities of rectangular regions. An upper bound for the integral is then calculated by summing the lower bound with a sum of probabilities of rectangular regions *between* the inscribed staircase region and a circumscribing staircase region. Thus, the resulting region integration of for the upper bound probability value completely covers the 7th octant region (see Figure 5.4).

If the difference between the upper and lower bounds is sufficiently small then the total 7th octant probability is taken to be the average of the two values. Otherwise the angular spacing is halved and the binding probability measures are re-calculated. The probability of the 3rd octant is calculated in a similar manner.

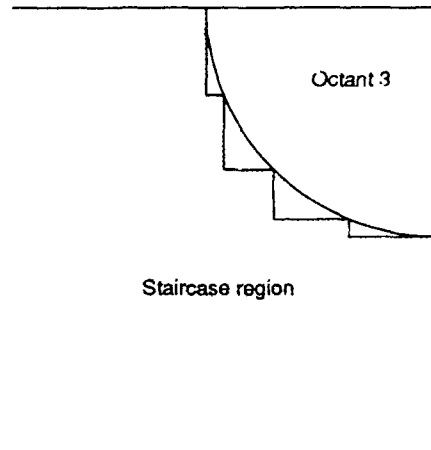


Figure 5.3: Inscribed staircase region, 5 points

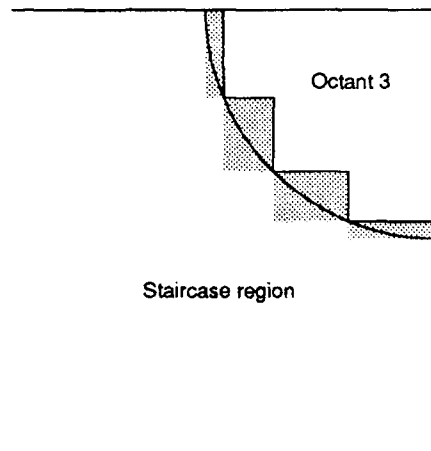


Figure 5.4: Circumscribed staircase region, 5 points

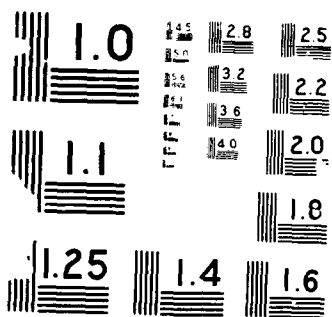
NO-A212-749 --PROGRESS IN THE IDENTIFICATION OF AIRBORNE KNOWN
TARGETS(U) OHIO STATE UNIV COLUMBUS ELECTROSCIENCE LAB
R CARRIER ET AL JUN 89 ESL-718048-12 N00014-86-K-0202

F/G 17/11

NL

UNCLASSIFIED





Single Level Crossing Conditional Symbol Probability Calculation

For a fixed threshold, the definition of the single level crossing scheme indicates that the probability of an entire single level crossing string may also be calculated as the product of probabilities of a series of Rician random variables being above or below the given threshold. For simplification of the program, single level crossing strings are transformed into a strings of binary symbols in which each symbol indicates "above" (1) or "below" (-1). These symbols are thus considered the constituent symbols of the strings and total string probability (given the catalog element and the threshold) in equation (5.2), etc. is estimated by the product of the probabilities of a series of Rician random variables, all exceeding or falling below the given threshold. Thus, the probability of a transformed single level crossing symbol is "above" the threshold, given a particular threshold, catalog element and location within the string may be estimated by the formulas:

$$P(a_i | T = t, C_j, i) = \int_t^\infty \frac{z}{\sigma^2} e^{-\frac{1}{2} \left(\frac{z^2 + \mu_{z_i}^2}{\sigma^2} \right)} I_0 \left(\frac{z \mu_{z_i}}{\sigma^2} \right) dz \quad (5.27)$$

$$= Q_1 \left(\frac{\mu_{z_i}}{\sigma}, \frac{t}{\sigma} \right) \quad (5.28)$$

In equation (5.28) μ_{z_i} and σ^2 are as defined above and Q_1 is the Marcum Q function.

The "below" case is calculated using different integration limits or the complementary Marcum Q function. Total string probability is calculated from products of these symbol probabilities.

5.2.3 Conclusions and Results

Comparison of likelihood functions generated with the analytical methods and those generated by the histogram method are similar for the noise levels which have been run. Misclassification results are given in Figures 5.5 and 5.6. These figures represent results obtained under the assumption of completely known noise variance. It is expected that the same matched noise phenomenon exhibited by the single level crossing scheme under the histogram method will appear if mismatched noise levels are used.

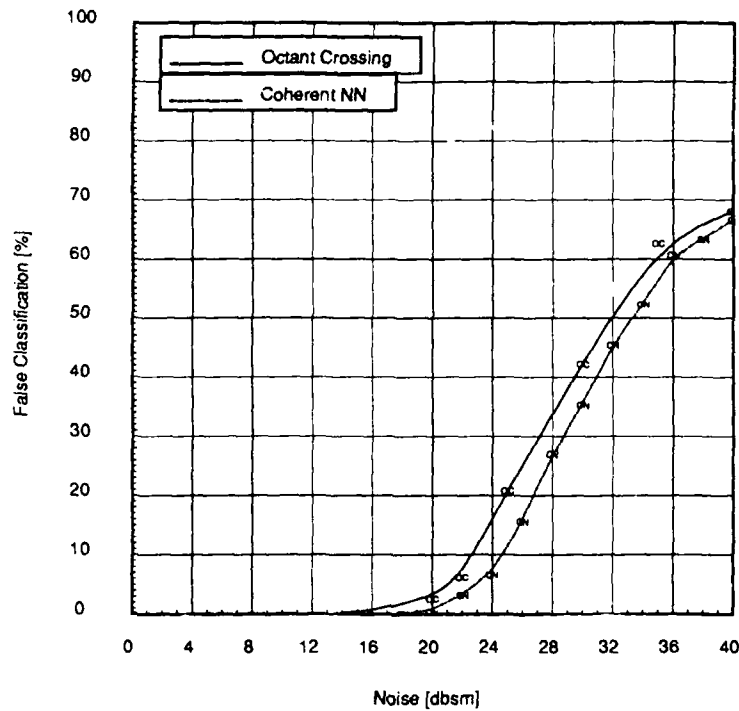


Figure 5.5: Octant crossing vs. coherent nearest neighbor

For comparison purposes, results from competing algorithms which employ the entire measurement vector. While the performance of the nearest-neighbor classifiers is usually better than that of the level-crossing classifiers, the level-crossing based pattern representations can be specified with only $\frac{1}{42}$ to $\frac{1}{35}$ the number of bits required by the nearest-neighbor specification. Thus, while the level-crossing observations cannot be considered "sufficient statistics" they are highly information preserving.

The consequences of this new algorithm are far reaching. Inference of more complex generating grammars requires the use of an *informant* [20]. The *informant* in these algorithms is expected to answer queries about the applicability of any given string. With the histogram method of likelihood function estimation, knowledge of the category of a given string is dependent upon the conditional probability of occurrence of that string. If, for all catalog elements, a string occurs with very small probability then it may take a very long time for knowledge of the category

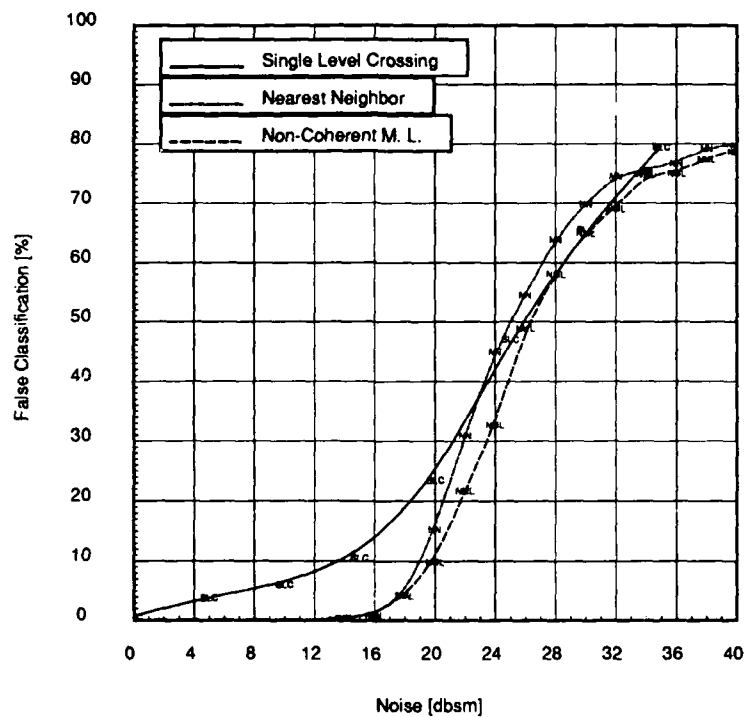


Figure 5.6: Single level crossing vs. nearest neighbor

to become available. The fact that any arbitrary string may be classified, no matter how small the conditional probability of occurrence, means that automatic inference of more complex generating grammars is possible with this technique.

The ability to classify a given symbolic representation quickly and easily also provides more flexibility in terms of classification algorithm design. The major hindrance in the determination of the symbolic representations conditional probability is the dependence on the adaptive magnitude threshold. It is proposed that the investigation of non-parametric syntactic pattern recognition techniques include the investigation of symbolic representations which do not include adaptive thresholds which are calculated over the entire range of measurements. Such symbolic assignment algorithms could represent quantities such as differential phase or magnitude. Furthermore, inference of the generating grammar for such symbolic assignments could be made directly from noiseless measurements.

It is conceded here that there exists no reason to believe that the generation of

such ad-hoc symbolic representations can be accurately modeled, in general, with a given generating grammar. However, by restricting the range of measurements and using automatic methods of inference, a simple classifier which uses an extremely distilled statistic of the full observation has been demonstrated to give good performance, even when compared to a classifier using the original vector observation. Continued exploration in this area may provide insight into the "structure" of such measurements.

As a further note, computation time for these strings can be exceedingly long. This becomes true when string probabilities are close for two or more catalog elements. Much effort has been expended on increasing computational efficiency. Some improvements have come about from novel storage and retrieval schemes of string and individual symbol probabilities.

5.3 Conversion of Syntactic Classifiers to Deterministic Forms

The syntactic classifiers derived in [17] are non-deterministic in nature. This means that there may be more than one production rule which is applicable to a particular nonterminal in a sentential form. In terms of automata, the transition function may have more than one value for a given state and symbol (the automata may have more than one place to "go" on a given symbol). Deterministic forms of automata or grammars do not.

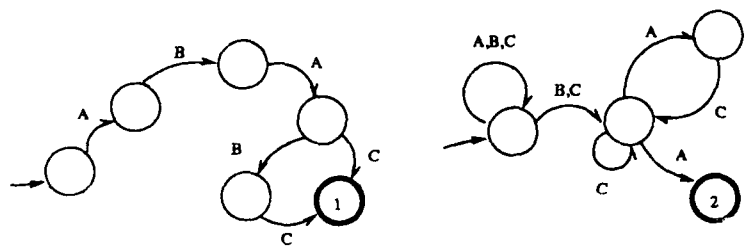
Derivation of a deterministic form for the syntactic classifier from the non-deterministic form can be summarized as:

1. *Label* the stop state each catalog elements automata with the corresponding catalog element name.
2. *Merge* the non-deterministic automata with labeled stop states together by adding a new start state with ϵ (null string) transitions to the start states of each of the automata.
3. *Convert* the resulting non-deterministic, merged automata to a deterministic form.

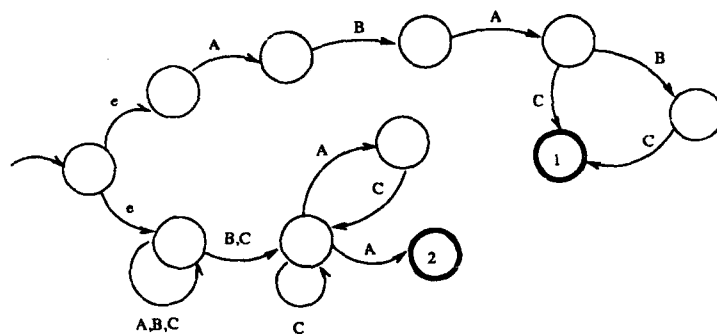
The conversion to a deterministic form is a well known process. It is fully describe in [21]. One of the more noteworthy aspects of the process is that each state of the deterministic form of the automaton is equivalent to a set of states of the non-deterministic form of the automaton. This leads to the fact that there are potentially 2^n states in the deterministic form of the automaton, where n is the number of states in the equivalent non-deterministic automaton.

Furthermore, the stop states in the deterministic form are determined from the stop states of the non-deterministic form. Specifically a state in the deterministic form or the automaton is a stop state for catalog element i if the stop state for catalog element i is contained in this state. Since states of the deterministic form of the automaton correspond to sets of states from the non-deterministic form it is easy to see that stop states can potentially correspond to acceptance of a string by more than one catalog element. This is the result which allows for analysis of the grammatical inference procedure.

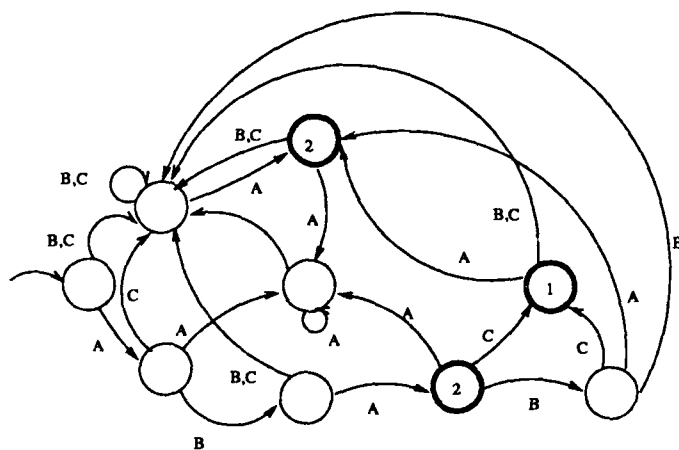
Even though application of the algorithm for derivation of the deterministic automata has potential to increase the number of states exponentially, it has, as a rule, decreased the number of states. Application of the algorithm to derived automata has revealed a number of multiply accepting states are present in the classifier. These states may be "traced back" to determine exactly which strings are being accepted in a multiple sense.



(a)



(b)



(c)

Figure 5.7: Conversion to deterministic form, (a) non-deterministic automata set with labeled final states. (b) merged non-deterministic automata. (c) resulting deterministic automata

6. References

- [1] W. Leeper, "Identification of scattering mechanisms from measured impulse response signatures of several conducting objects," M.S. Thesis, The Ohio State University, 1984.
- [2] R. L. Moses and R. Carrière, "Parametric modeling of radar targets using canonical scattering centers," Technical Report 719267-13, The Ohio State University, Department of Electrical Engineering, ElectroScience Laboratory, December 1988.
- [3] R. L. Moses and R. Carrière, "Autoregressive moving average modeling of radar target signatures," Technical Report 717220-6, The Ohio State University, Department of Electrical Engineering, ElectroScience Laboratory, January 1988.
- [4] R. Carrière and R. L. Moses, "High resolution radar target modeling using ARMA models," Technical Report, The Ohio State University, Department of Electrical Engineering, ElectroScience Laboratory, May 1989.
- [5] R. A. Roberts and C. T. Mullis, *Digital Signal Processing*. Reading, Mass.: Addison-Wesley, 1987.
- [6] R. Kumaresan and D. W. Tufts, "Estimating the parameters of exponentially damped sinusoids and pole-zero modeling in noise," *IEEE Transactions on Acoustics, Speech, and Signal Processing*, vol. ASSP-30, no. 6, pp. 833-840, December 1982.
- [7] S. M. Kay, *Modern Spectral Estimation, Theory and Application*. Englewood Cliffs, NJ: Prentice-Hall, 1988.
- [8] L. Marple, *Digital Spectral Analysis with Applications*. Englewood Cliffs: Prentice-Hall, 1987.
- [9] E. M. Kennaugh and R. L. Cosgriff, "The use of impulse response in electromagnetic scattering problems," in *IRE National Conv. Rec. pt.1*, pp. 72-77, 1968.
- [10] C. L. Nikias and M. R. Raghuveer, "Bispectrum estimation: A signal processing framework," *IEEE Transactions on Acoustics, Speech, and Signal Processing*, vol. 35, no. 7, pp. 869-891, July 1987.
- [11] M. R. Raghuveer and C. L. Nikias, "Bispectrum Estimation: A parametric approach," *IEEE Transactions on Acoustics, Speech, and Signal Processing*, vol. ASSP-30, no. 5, pp. 1213-1230, October 1985.

- [12] D. R. Brillinger and M. Rosenblatt, "Asymptotic theory of estimates of k -th order spectra," in *Spectral Analysis of Time Series*, B. harris, Ed., New York: Wiley, 1967.
- [13] E. K. Walton and J. D. Young, "The Ohio State University compact radar cross-section measurement range," *IEEE Transactions on Antennas and Propagation*, vol. AP-32, no. 11, pp. 1218-1223, November 1984.
- [14] F. D. Garber, N. F. Chamberlain, and O. Snorrason, "Time-domain and frequency-domain feature selection for reliable radar target identification," in *Proceedings of the IEEE 1988 National Radar Conference*, pp. 79-84, Ann Arbor, MI, April 20-21, 1988.
- [15] A. Kamis, E. K. Walton, and F. D. Garber, "Radar target identification techniques applied to a polarization diverse aircraft data base," Technical Report 717220-2, The Ohio State University, Department of Electrical Engineering, ElectroScience Laboratory, March 1987.
- [16] J. S. Chen and E. K. Walton, "Comparison of two target classification techniques," *IEEE Transactions on Aerospace and Electronic Systems*, vol. AES-22, no. 1, pp. 15-22, 1986.
- [17] O. S. Sands, "Syntactic pattern recognition for radar target identification," M.S. Thesis, The Ohio State University, September 1986. also: ElectroScience Laboratory Report 718048-2.
- [18] F. B. Hildebrand, *Introduction to Numerical Analysis*. New York: McGraw-Hill, 1974.
- [19] S. Parl, "A new method of calculating the generalized q function," *IEEE Transactions on Information Theory*, vol. IT-26, no. 1, pp. 121-124, January 1980.
- [20] K. S. Fu, *Syntactic Pattern Recognition and Applications*. Englewood Cliffs, NJ: Prentice-Hall, 1982.
- [21] A. V. Aho and J. D. Ullman, *The Theory of Parsing, Translation and Compiling*. Volume 1, Englewood Cliffs: Prentice-Hall, 1972.